ISSN 1451 - 9372 (Print)
ISSN 2217 - 7434 (Online)
APRIL-JUNE 2024
Vol.30, Number 2, 89-177

Chemical Industry & Chemical Engineering Quarterly

The AChE Journal for Chemical Engineering,
Biochemical Engineering, Chemical Technology,
New Materials, Renewable Energy and Chemistry
www.ache.org.rs/ciceq

Journal of the
Association of Chemical Engineers of
Serbia, Belgrade, Serbia

Chemical Industry & Chemical Engineering
CI&CEQuarterly

Journal of the
Association of Chemical Engineers of
Serbia, Belgrade, Serbia

Chemical Industry & Chemical Engineering Quarterly

Vol. 30 Belgrade, April-June 2024 No. 2

Chemical Industry & Chemical Engineering Quarterly (ISSN 1451-9372) is published quarterly by the Association of Chemical Engineers of Serbia, Kneza Miloša 9/I, 11000 Belgrade, Serbia

Editor:
Vlada B. Veljković
veljkovic@yahoo.com

Editorial Office:
Kneza Miloša 9/I, 11000 Belgrade, Serbia
Phone/Fax: +381 (0)11 3240 018
E-mail: shi@ache.org.rs
www.ache.org.rs

For publisher:
Ivana T. Drvenica

Secretary of the Editorial Office:
Slavica Desnica

Marketing and advertising:
AChE Marketing Office
Kneza Miloša 9/I, 11000 Belgrade, Serbia
Phone/Fax: +381 (0)11 3240 018

Publication of this Journal is supported by the Ministry of Education, Science and Technological Development of the Republic of Serbia

Subscription and advertisements make payable to the account of the Association of Chemical Engineers of Serbia, Belgrade, No. 205-2172-71, Komercijalna banka a.d., Beograd

Computer typeface and paging:
Marija B. Tasić

Journal manager:
Aleksandar B. Dekanski

Printed by:
Faculty of Technology and Metallurgy, Research and Development Centre of Printing Technology, Karnegijeva 4, P.O. Box 3503, 11120 Belgrade, Serbia

Abstracting/Indexing:
Articles published in this Journal are indexed in *Thompson Reuters* products: *Science Citation Index - Expanded*™ - access *via Web of Science*®, part of *ISI Web of Knowledge*℠

CONTENTS

The activities of the Association of Chemical Engineers of Serbia are supported by:

MINISTRY OF SCIENCE, TECHNOLOGICAL DEVELOPMENT AND INNOVATION OF REPUBLIC OF SERBIA

Faculty of Technology and Metallurgy, University of Belgrade

Faculty of Science, University of Novi Sad

Institute for Technology of Nuclear and Other Mineral Raw Materials, Bekgrade

Faculty of Technology, University of Novi Sad

Institute of Chemistry, Technology and Metallurgy, University of Belgrade

Faculty of Technical Sciences University of Novi Sad

Faculty of Technology, University of Niš, Leskovac

Faculty of Technical Sciences, University of Priština, Kosovska Mitrovica

IMS Institute, Belgrade

DCP HEMIGAL
Leskovac

Elixir Prahovo

CI&CEQ
Chemical Industry & Chemical Engineering Quarterly

Available online at
Association of the Chemical Engineers of Serbia *AChE*
www.ache.org.rs/CICEQ

Chem. Ind. Chem. Eng. Q. 30 (2) 89–98 (2024) CI&CEQ

VINILA MUNDAKKAL LAKSHMANAN[1,2]
APARNA KALLINGAL[1]
SREEPRIYA SREEKUMAR[1,2]

INTERNAL MODEL CONTROL OF CUMENE PROCESS USING ANALYTICAL RULES AND EVOLUTIONARY COMPUTATION

Article Highlights

- Classical controllers have been implemented for the cumene process with much uncertainty
- IMC controller is designed for cumene production and is compared with the ZN tuning controller
- It is identified that the PI controller is apt for this specific cumene production process
- PSO-PI controller is designed to analyze performance with evolutionary computation techniques

[1]Department of Chemical Engineering, National Institute of Technology Calicut, Kozhikode, Kerala, India

[2]Department of Robotics and Automation, Adi Shankara Institute of Engineering and Technology, Kalady, India

SCIENTIFIC PAPER

UDC 547:544:519.6

Abstract

Cumene is a precursor for producing many organic chemicals and is thinner in paints and lacquers. Its production process involves one of the large-scale manufacturing processes with complex kinetics. Different classical control strategies have been implemented and compared in this process for the cumene reactor. As a system with large degrees of freedom, a novel approach for extracting the state space model from the COMSOL Multiphysics implementation of the system is adopted here. Internal Modern Control (IMC) based PI and PID controllers are derived for the system. The system is reduced to the FOPDT and SOPDT model structure to derive the controller setting using Skogestad half rules. The integral time is modified for excellent set point tracking and faster disturbance rejection. From the analysis, it can be stated that the PI controller suits more for this specific process. The particle swarm optimization (PSO) algorithm, an evolutionary computation technique, is also used to tune the PI settings. The PI controllers with IMC, Zeigler Nichols, and PSO tuning are compared, and it can be concluded that the PSO PI controller settles at 45 s without any oscillations and settles down faster for the disturbance of magnitude 0.5 applied at t = 800 s. However, it is computationally intensive compared to other controller strategies.

Keywords: IMC PI, IMC PID, Skogestad half rule, Zeigler Nichols, PSO PI.

PID (Proportional-Integral-Derivative) controller is the widely adopted control strategy in the industry due to its simplicity in design and robustness. Besides, it can be employed in many processes with wide operating conditions. Even though the PID controller owns only three design parameters, finding suitable values (settings) for them without a systematic method is difficult. A visit to a process industry will reveal a high count of poorly tuned PID controllers. The scope of the systematic approach for developing classical controllers with different tuning mechanisms to the cumene reactor in the cumene plant in HOCL, Kochi, is analyzed in this study.

Sigurd Skogestad has introduced analytic rules for reducing the model and tuning the PID controller [1]. Previous work in this area includes Ziegler and

Correspondence: A. Kallingal, Department of Chemical Engineering, National Institute of Technology Calicut, Kozhikode, Kerala, 673601, India.
E-mail: aparnak@nitc.ac.in
Paper received: 11 July, 2022
Paper revised: 23 March, 2023
Paper accepted: 22 June, 2023

https://doi.org/10.2298/CICEQ220711014M

Nichol's [2]. classic study and discussion on IMC PID-tuning mechanism by Rivera *et al.* [3]. For integrating processes, the Ziegler-Nichols settings produce good disturbance rejection, but in the case of processes with dominant delay, they produce quite poor performance and aggressive settings [4–6]. On the other hand, the analytically derived IMC settings by Rivera *et al.* [3] have a weak disturbance rejection for integrating processes [6–7]. Still, they are robust and have excellent setpoint change responses. In a multidimensional space, a great number of particles move around in the PID controller with a basic PSO technique introduced by Kennedy and Eberhart [7], with each particle memorizing its vector of position and velocity, as well as the time at which it reached its peak degree of fitness [8]. PSO starts with a random population and updates it to find optimal solutions. PSO has the advantage of requiring no evolution operators, such as mutation and crossover operators, and it does not necessitate the adjustment of many free parameters [9,10]. Farimah *et al.* [11] have discussed the optimization of the cumene process with statistical and genetic algorithm-based methods. Some researchers discuss artificial intelligence and machine learning approaches in chemical processes, especially the cumene production process [12–14].

In this work, authors have derived PID controllers [15] for studying the disturbance rejection and setpoint tracking of the cumene reactor, which is designed as a four-layer fixed bed catalytic reactor [16,17]. The major difficulty in the analysis is the availability of a system model for the process with high degrees of freedom [18,19]. The state space model of the system for the analysis is obtained from the COMSOL design of the system by MATLAB Livelink [20–22]. The classical PI and PID controllers based on Internal Model Control (IMC) are derived based on analytical rules [23,24]. P, PI, and PID controllers based on Zeigler Nichols tuning are developed as the system's basic controller for comparison [25]. PID controller based on Particle Swarm Optimisation is derived from studying the advantage of the evolutionary algorithm approach [26].

The major works included in the paper are: Derivation of system model for the plant (cumene rector in HOCL, Kochi) from the state matrices obtained from COMSOL design [14]. Design of PI and PID controllers for the system using analytical rules and comparison. Design of IMC P, PI, and PID controller based on Zeigler Nichols tuning. PI controller design with particle swarm optimization and comparison with other controllers.

The paper is structured as follows. The first section details the cumene production process and state space model of the reactor. The second section derives the PI and PID controllers design using analytical rules. P, PI, and PID controllers with Zeigler Nichols tuning are discussed in the following section. The following section explains the PI controller based on an evolutionary algorithm. The simulation results and comparative studies are also presented. The concluding comments are marked in the last section.

STATE MODEL OF THE CUMENE PROCESS

Cumene Production Process Description

The fundamental reaction in the cumene production process in the cumene plant is an alkylation process in which benzene and propylene react to form cumene in the presence of an acidic catalyst [20,27]. HOCL set up a cumene plant employing SPA catalyst in 1983 at Kochi. The used packed bed reactor has four layers of solid phosphoric acid beds [20,28].

The principal reaction is expressed as:

$$C_3H_6 + C_6H_6 \rightarrow CH(CH_3)_2 \tag{1}$$

The simplified model of the reactor is given by Eqs. 2–4.

The mass balance equations are:

$$\begin{aligned}
&\epsilon_b\,\rho_g \frac{dw_B}{dt} = \left(-\frac{M}{A_{\text{int}}}\frac{\partial w_B}{\partial z} + Mw_B(-r_B)\right).....(a)\\
&\epsilon_b\,\rho_g \frac{dw_P}{dt} = \left(-\frac{M}{A_{\text{int}}}\frac{\partial w_P}{\partial z} + Mw(-r_P)\right).....(b)\\
&\epsilon_b\,\rho_g \frac{dw_C}{dt} = \left(-\frac{M}{A_{\text{int}}}\frac{\partial w_C}{\partial z} + Mw_C r_C\right).....(c)
\end{aligned} \tag{2}$$

where A_{int} is the inner cross-sectional area of the reactor, M is the mass flow rate, Mw_i is the molar weight of the ith component, r_i is reaction rate of ith species, ϵ_b is catalytic bed void fraction, ρ_g is gas phase density and w_B , w_P and w_C are the mass fractions of benzene, propylene, and cumene, respectively.

The reactor energy balance equation is:

$$\begin{aligned}
&\left(\epsilon_b\,\rho_g C_{Pmix} + (1-\epsilon_b)\rho_c C_{Pcat}\right)\frac{dT}{dt} = -\frac{M}{A_{\text{int}}}C_{Pmix}\frac{\partial T}{\partial z}\\
&+\pi\frac{U}{A_{\text{int}}}(T_{Shell}-T) + r_c(-\Delta H_r)
\end{aligned} \tag{3}$$

where ϵ_b is the catalytic bed void fraction, ρ_g is the gas phase density, C_{Pmix} is the specific heat of the mixture, ρ_c is the catalytic pellet density, C_{Pcat} is the specific heat of the catalyst, ρ_c is catalytic pellet density, A_{int} is the inner cross-sectional area of the reactor, M is the mass flow rate, U is the heat transfer coefficient, T_{Shell} is the reactor shell side temperature and ΔH_r is the enthalpy of the reaction.

The rate of reaction is:

$$r_C = \rho_c (1 - \epsilon_b) \eta_1 r_1 \quad (4)$$

where

$$r_1 = k w_B w_C \text{ and } k = 3500 e^{-\frac{13.28}{RT}} \quad (5)$$

ρ_c is catalytic pellet density, ϵ_b is catalytic bed void fraction, η_1 is reaction efficiency w_B *and* w_C are mass fractions of benzene and cumene, R is the universal gas constant, and T is the absolute temperature.

As a system with a large amount of uncertainty, it is very difficult to extract the state space model of the system. Besides, the system is represented by nonlinear partial differential equations, making the solution derivation more tedious. Incorporating the parameters from the studied plant, the system has been implemented in COMSOL Multiphysics to extract state transition matrices of the system [14].

Extraction of Model from COMSOL Multiphysics using Matlab Livelink

For many chemical processes, the state space modeling of the system is not available because of the high degrees of freedom. The COMSOL Multiphysics modeling of the reactor will help with the performance analysis and optimization of specific parameters [20]. A novel approach for extracting the state space matrices from COMSOL is utilized here. The state space matrices of the cumene production process have been obtained from the COMSOL design using MATLAB Livelink. The Continuous-time state-space model obtained has 11493 DOF. The system has been reduced to a 4th order system using model order reduction. The parameters used to simulate the model are listed in Table 1.

Table 1. Parameters used for simulation.

Parameters	Unit for simulation
Height of the reactor	15.3 m
Diameter of the reactor	1.5 m
Diameter of the catalyst particle	1 mm
Density of catalyst particle	58000 kg/m^3
Porosity of catalyst particle	0.75
Initial solid height	150 mm
Bed porosity	0.5
Inlet feed velocity	0.8 m/s
Inlet feed composition (C_6H_6, C_3H_8, C_3H_6)	8:2:1
Inlet feed temperature	316 K
Inlet pressure	32.9 atm

The state space matrices obtained for the cumene production process after model order reduction are given in Eq. 6:

$$A = \begin{bmatrix} -0.5409 & 5.304x10^{-7} & 1.52x10^{-10} & 1.027x10^{-6} \\ -1.939x10^{-5} & -0.5077 & 1.96x10^{-6} & -3.858x10^{-10} \\ -0.00373 & -1.527x10^{-5} & -0.4719 & 1.5x10^{-5} \\ 1.021x10^{-5} & 0.002405 & 1.947x10^{-6} & -0.4492 \end{bmatrix} \quad (6)$$

$$B = \begin{bmatrix} 1.66x10^{-17} \\ 1.286x10^{-17} \\ 7.461x10^{-17} \\ 1.31x10^{-16} \end{bmatrix}$$

$$C = \begin{bmatrix} 1.878x10^{-17} & 2.291x10^{-17} & 9.192x10^{-18} & 5.657x10^{-18} \end{bmatrix}$$

$$D = [0]$$

INTERNAL MODEL CONTROL-BASED PI AND PID CONTROLLERS

The simple two-step procedure proposed by Sigurd Skogestad [1] has been adopted to design a controller for the cumene production process. The tuning rules should be well-motivated for a good controller, with a preference for model-based and analytically determined tuning rules. They should be simple to remember. They should be able to handle a wide range of tasks. The Internal Model Control PID, which satisfies the objectives of a good PID controller, provides the rules for system model reduction and design of the PID controller. Figure 1 shows the packed bed reactor structure and the system with feedback control. Here u is the manipulated input, d is the disturbance, y is the controlled output and y_s is the setpoint for controlled output. The process transfer function is represented by $(s) = \frac{\Delta y}{\Delta u}$, controller feedback is represented as $c(s)$. Δ, the deviation of the variables and s, the laplace variables are neglected to simplify the notation.

Using the proposed Skogestad half rule, the system's first and second-order plus delay model is derived. The controller settings can be derived based on the model. If we consider the first-order model plus delay model, it will result in PI controller settings, and if we start from the second-order plus delay model, PID controller settings can be obtained.

The PID settings are derived for the series form of PID controller as follows:

$$c(s) = K_c \left(\frac{\tau_1 + 1}{\tau_1 s} \right) (\tau_D s + 1) \quad (7)$$

$$c(s) = \frac{K_c}{\tau_1 s} \left(\tau_1 \tau_D s^2 + (\tau_1 + \tau_D) s + 1 \right) \quad (8)$$

Step 1: Process model approximation

The model approximation includes the approxi-

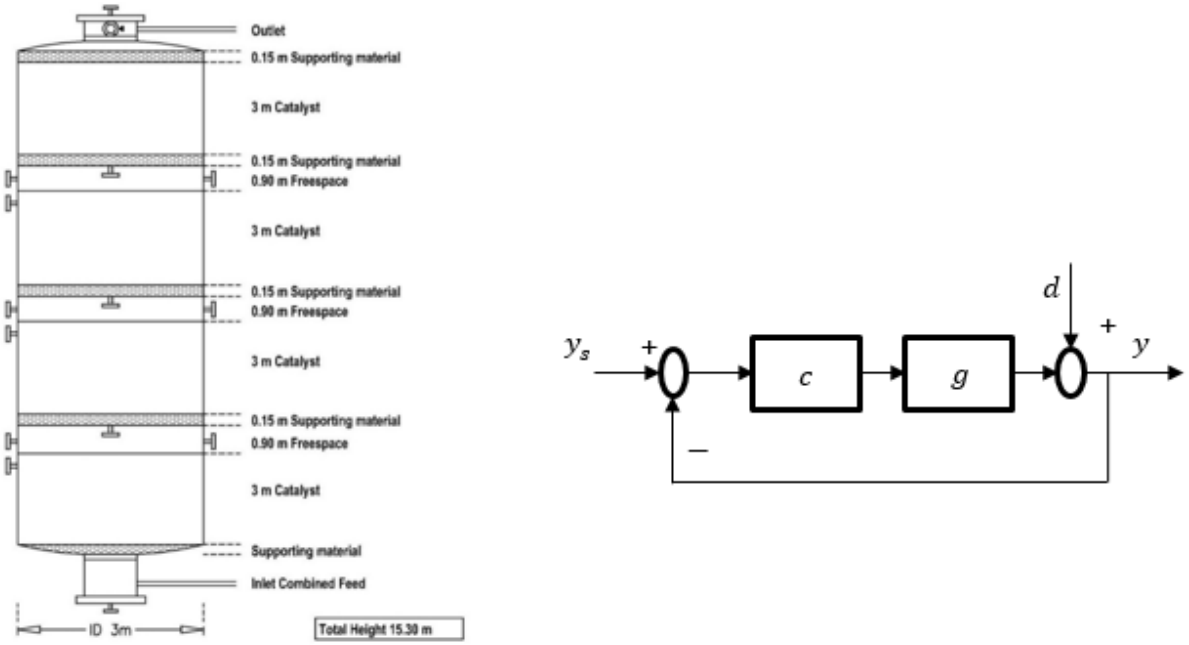

Figure 1. System with feedback control.

mation of the original model to a first- or second-order plus time delay model, $g(s)$. Skogestad half rules approximate first order plus dead time (FOPDT) and second order plus dead time (SOPDT) systems. For a system to apply Skogestad half rules, the denominator should be in terms of τs, and a dominant time constant should exist ($\boldsymbol{\tau}_{largest} \geq 1.5\boldsymbol{\tau}_{next\ largest}$) and the system should be stable. The parameters that need to be estimated for the model approximation are planted gain K, dominant lag time constant (τ in case FOPDT and τ_1 in case of SOPDT), time delay (dead time) θ, second-order lag time constant τ_2,

The approximate first order plus deadtime (FOPDT) model can be represented as

$$\frac{Ke^{-\theta s}}{\tau s+1} \tag{9}$$

The parameters are obtained as follows:

$$K = K_{higher\ order}$$

$$\tau = \tau_{\text{largest}} + 0.5\tau_{next\ \text{largest}}$$

$$\theta = 0.5\tau_{next\ \text{largest}} + \sum\tau + \theta_{higher\ order}$$

Approximated model after substituting the parameters is:

$$\frac{4.26x10^{-33}e^{-10.942s}}{2.29s+1} \tag{10}$$

Similarly, the approximate second-order plus deadtime model can be represented as:

$$\frac{Ke^{-\theta s}}{(\tau_1 s+1)(\tau_2 s+1)} \tag{11}$$

The parameters are obtained as:

$$K = K_{higher\ order}$$

$$\tau_1 = \tau_{\text{largest}}$$

$$\tau_2 = \tau_{next\ \text{largest}} + 0.5\tau_{\text{second }next\ \text{largest}}$$

$$\theta = 0.5\tau_{\text{second }next\ \text{largest}} + \sum\tau + \theta_{higher\ order}$$

Approximated model after substituting the parameters is:

$$\frac{4.26x10^{-33}e^{-8.897s}}{(2.23s+1)(3.105s+1)} \tag{12}$$

Step 2: Internal model control based PID tuning

In this session, PI and PID controllers are derived for the FOPDT and SOPDT system using the direct synthesis method or the internal model control approach[1,3].

From the comparison of Eq. A9 and A10 (Supplementary materials), the parameters can be obtained as:

$$\tau_D = \tau_2;\ \tau_1 = \tau_1;\ K_c = \frac{1}{K}\frac{\tau_1}{(\tau_c+\theta)} \tag{13}$$

The parameter values are obtained from the model, and the response is obtained for various tuning

values. The best tuning value is identified, and the integral terms are varied to obtain the best setpoint tracking and disturbance rejection.

P, PI, AND PID CONTROLLERS USING ZEIGLER NICHOLS TUNING

Ziegler-Nichols tuning is applied to the FOPDT model of the process to obtain the system's step response. The reaction curve process identification procedure is used to identify the parameters for P, PI, and PID settings. The inflection point is identified, and the tangent is plotted in the reaction curve. The values obtained are effective delay, D_e, process reaction rate, R_p and unit reaction rate, R_u; these values are used for parameter setting. Parameter settings from the process reaction curve for P, PI, and PID controllers are given in Table 2.

Table 2. PID setting from process reaction curve.

Type	K_c	T_i	T_d
P	$1/R_u D_e$	-	-
PI	$0.9 R_u D_e$	$3.33 D_e$	-
PID	$1.2/R_u D_e$	$2D_e$	$0.5 D_e$

PSO PID CONTROLLER FOR THE SYSTEM

An evolutionary algorithm for PI tuning is introduced to compare the performance in settling time and rejection of disturbance with that of analytical rules. Particle swarm optimization algorithm, also known as bird swarm foraging algorithm, is used here for tuning the PI parameters, in which the idea originated from the study of the predation behavior of birds or fish. The particle swarm algorithm simulates so that the birds in the flock are considered massless particles. The attributes of each particle include position and velocity. Each particle searches for the optimal solution separately in the search space, determines the fitness value through the fitness function to evaluate the quality of the current position, and records the optimal solution. Particles are evolved by competition and corporation among themselves through generations. The particles adjust their speed and position according to the local and global optimal solutions. The analysis depicts the importance of computational techniques in controller design. The PSO algorithm to tune the PI parameter based on the best position and velocity is given in Figure 2.

PSO algorithm

The velocity of the particle:

$$\vartheta_{id}^{k} = w\,\vartheta_{id}^{k-1} + c_1 r_1\left(pbest_{id} - x_{id}^{k-1}\right) + c_2 r_2\left(gbest_{id} - x_{id}^{k-1}\right) \quad (14)$$

Position of the particle:

$$x_{id}^{k} = x_{id}^{k-1} + \vartheta_{id}^{k-1} \quad (15)$$

where,

v_{id} =velocity of the i[th] particle

x_{id} =position of the i[th] particle

k = discrete time constant

id= particle index

$pbest_{id}$=best position found by the i[th] particle

$gbest_{id}$ = best position found by the swarm

w= inertia factor

c_1, c_2 = acceleration constant

r_1, r_2= random numbers [0,1]

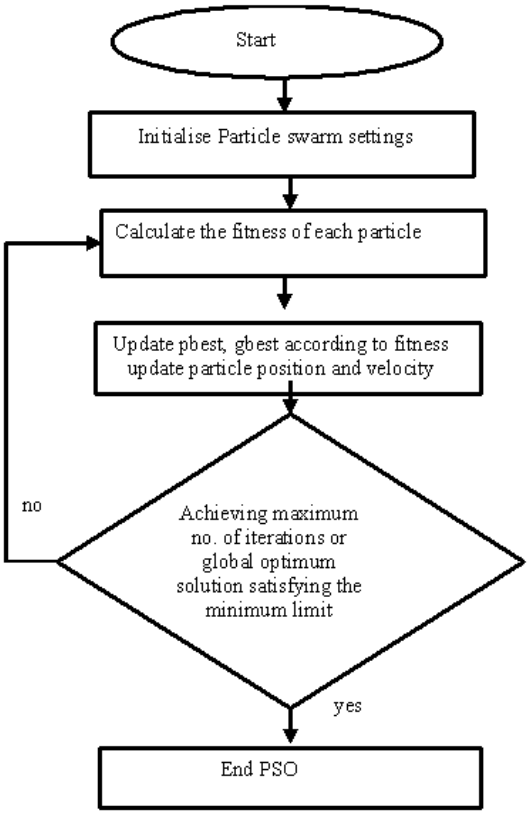

Figure 2. PSO algorithm.

SIMULATION RESULTS

IMC-based PI and PID controllers

The PI and PID controllers for the system with different tuning parameter values are designed. Figure 3 shows the PI controller with three different tuning parameters.τ_c=0, τ_c=1, and τ_c=1.5. From the analysis, it can be identified that the PI and PID controllers with τ_c=1.5 shows better disturbance rejection and setpoint tracking.

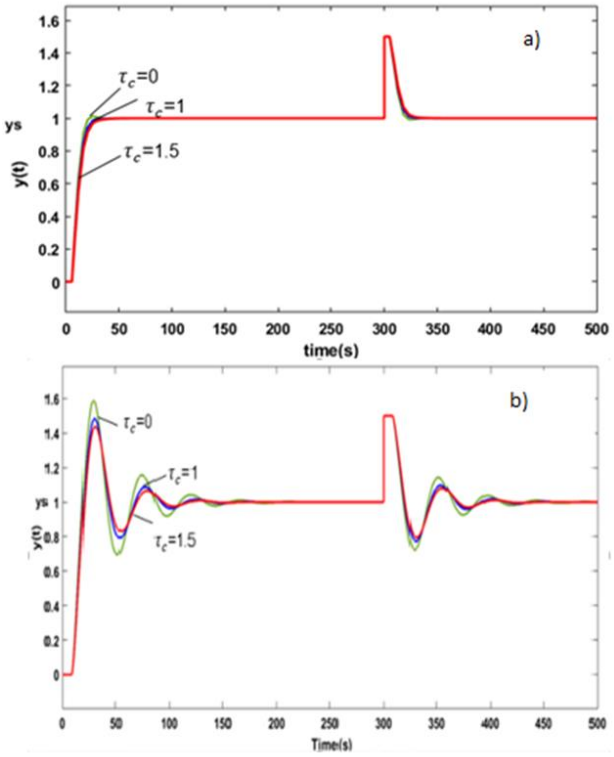

Figure 3. (a) PI and (b) PID controller with different tuning parameters.

To improve the disturbance rejection, the rule for an integral term is modified in the proposed IMC PI tuning. Figure 4 shows the effect of changing the integral time for PI-control of the system with *K*c =9.63x10^{33}. The setpoint change is given at t=0 s, and a load disturbance of 0.5 magnitude is applied at t = 800 s. The integral time has given the values as τ_1, θ, 2θ, 4 s,3 s, and 2 s.

Interpretation of PI controller output

$\boldsymbol{\tau_I}$ =$\boldsymbol{\tau_1}$=3.29 s: excellent setpoint tracking and fast settling for a load disturbance.

$\boldsymbol{\tau_I}$ =2$\boldsymbol{\theta}$: setpoint response is poor and slow settling time for load disturbance.

$\boldsymbol{\tau_I}$ = $\boldsymbol{\theta}$: even quicker settling and reaction to setpoints (and robustness).

$\boldsymbol{\tau_I}$ = $\boldsymbol{4s}$: excellent setpoint tracking and faster settling time.

$\boldsymbol{\tau_I}$ = 3 s: good setpoint tracking and faster settling time.

$\boldsymbol{\tau_I}$= $\boldsymbol{2\ s}$: response is poor with slow settling time.

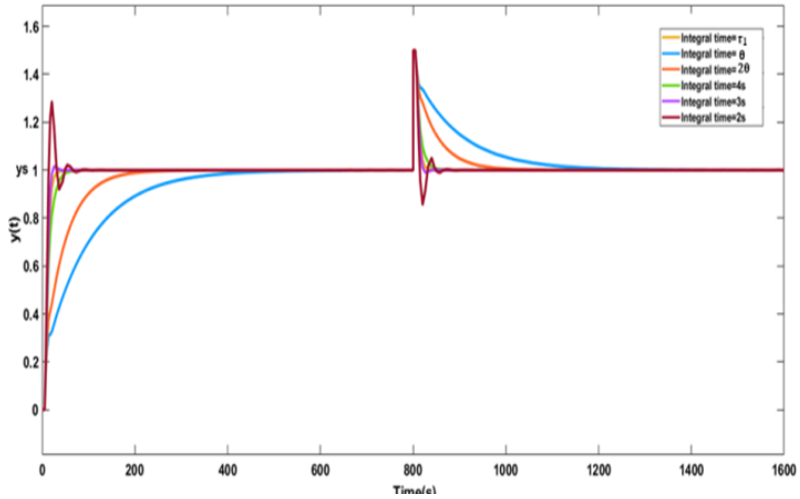

Figure 4. PI-control of the system with different integral times. K_c =9.63x10^{33}, change in setpoint is at t = 0 s and load disturbance is at t = 800 s.

Table 3. Disturbance rejection and setpoint tracking for various values of integral timeτ_I for PI controller.

Type	Integral time	Unit setpoint change at t=0s				Load Perturbation of magnitude 10 at t=800s			
		t_p (s)	t_s (s)	M_p (%)	ϵ_{ss}	t_p (s)	t_s (s)	M_p (%)	ϵ_{ss}
Proposed PI	τ_I=τ_1	0	45	0	0	0	38	0	0
	τ_I=2θ	0	600	0	0	0	520	0	0
	τ_I=θ	0	350	0	0	0	60	0	0
	τ_I=4s	0	75	0	0	0	60	0	0
	τ_I=3s	25	45	1.5%	0	30	40	2%	0
	τ_I=2s	21	110	28%	0	20	100	14%	0

A good trade-off between disturbance response and robustness is obtained by selecting the integral time. $\boldsymbol{\tau_I = \tau_1}$, for the above system.

In the proposed IMC PID tuning, the rule for the integral term is modified to improve the disturbance rejection. Figure 5 shows the effect of changing the integral time for PID-control of the system with Kc =5.03x10^{32}. The setpoint change is given at t=0s, and a load disturbance of 0.5 magnitude is applied at t = 800 s. The integral time has given the values as τ_1, θ, 2θ, 4 s,3 s, and 2 s.

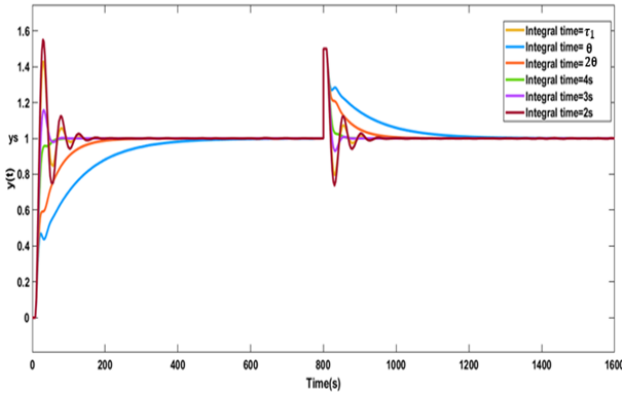

Figure 5. PID control of the system with different integral times. K_c = 9.63x10^{33}, change in setpoint is at t = 0 s, and load disturbance is at t = 800 s.

Peak time t_p, settling time t_s, peak oversoot M_p, and steady-state error ϵ_{ss} corresponding to the disturbance rejection and setpoint tracking for the PID controller are shown in Table 4.

Interpretation of PID controller output

$\tau_I = \tau_1 = 2.203$ s: poor response with slow oscillations.

$\tau_I = 2\theta$: slow setpoint response and slow settling.

$\tau_I = \theta$: even faster settling and setpoint response (and robustness).

$\tau_I = 4s$: excellent setpoint tracking and faster settling time.

τ_I = 3 s: slow oscillations in setpoint tracking and faster settling time.

$\tau_I = 2s$: poor response with oscillations.

A good trade-off between disturbance response and robustness is obtained by selecting the integral time. $\tau_I = 4\ s$, which corresponds to the above system.

Table 4. Disturbance rejection and setpoint tracking for various values of integral time, τ_I for PID controller.

Integral Types time		Unit setpoint change at t=0s				Load Perturbation of magnitude 10 at t=800s			
		t_p (s)	t_s (s)	M_p (%)	ϵ_{ss}	t_p (s)	t_s (s)	M_p (%)	ϵ_{ss}
Proposed PID	τ_I=τ_1	29	160	43%	0	30	150	20%	0
	τ_I=2θ	0	570	0	0	0	600	0	0
	τ_I=θ	0	300	0	0	0	350	0	0
	τ_I=4s	0	103	0	0	0	95	0	0
	τ_I=3s	32	100	16%	0	30	70	7%	0
	τ_I=2s	29	500	57%	0	30	200	26%	0

Comparison of IMC-based PI and PID controllers

The comparison of PI and PID controllers has been done for various values of integral time. Figure 6 shows that the PI controller has a better-set point tracking disturbance rejection than the PID controller. Table 5 gives the comparison of PI and PID controllers for τ_I=τ_1 and τ_I=4 s. The controllers corresponding to these values have better setpoint tracking and disturbance rejection than other integral values. In the PI controller, τ_I=τ_1 gives a better response, where τ_I= 4 s gives a better setpoint tracking disturbance rejection, as in the case of the PID controller.

P, PI, and PID controllers with Zeigler Nichols Tuning

This analysis uses the parameter obtained from the process reaction curve for parameter setting. For the controller setting, the unit reaction rate, R_u and effective delay,D_e obtained from the reaction curve are used for calculating K_c, T_i, and T_d . The parameter values obtained for P, PI, and PID controllers are given in Table 6.

A comparative study of P, PI, and PID controllers derived from Zeigler Nichols's PID setting is done in this section. The response of P, PI, and PID controllers for a setpoint change given at $t = 0\ s$, and a load disturbance of magnitude 0.5 applied at $t = 800\ s$ is given in Figure 7. It can be identified that the PI controller gives better setpoint tracking compared to the sluggish nature of the PID controller. The analysis of both IMC and Zeigler Nichols controllers depicts that the PI controllers best suit the cumene production process with improved robustness and stability.

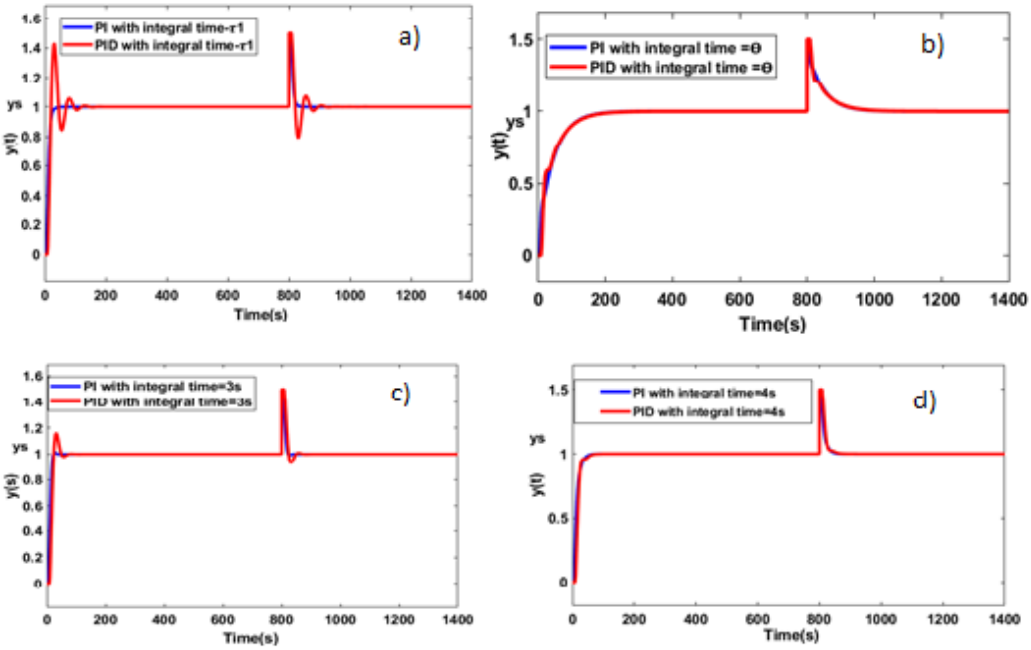

Figure 6. Comparison of PI and PID controllers done for various values of integral times, τ_I (a) τ_I =τ_1, (b) τ_I =θ, (c) τ_I = 3 s, and (d) τ_I = 4s.

Table 5. Disturbance rejection and setpoint tracking for PI and PID controllers.

Integral Types time		Unit Setpoint change at t=0 s				Load Perturbation of magnitude 10 at t=800 s			
		t_p (s)	t_s (s)	M_p (%)	ϵ_{ss}	t_p (s)	t_s (s)	M_p (%)	ϵ_{ss}
Proposed PI	τ_I=τ_1	35	45	0	0	0	38	0	0
	τ_I=4s	0	75	0	0	0	60	0	0
Proposed PID	τ_I=τ_1	29	160	43%	0	30	150	20%	0
	τ_I=4s	0	103	0	0	0	95	0	0

Table 6. Zeigler Nichols PID setting.

Type	K_c	$T_i(s)$	$T_d(s)$
P	$7.538*10^{31}$	-	-
PI	$6.784*10^{31}$	36.437	-
PID	$9.0456*10^{31}$	21.884	5.4710

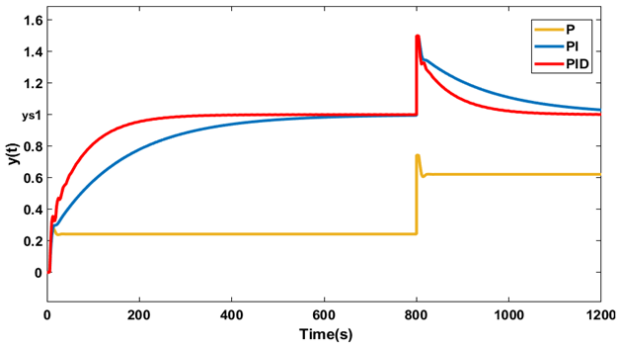

Figure 7. P, PI, and PID controller response with Zeigler Nichols tuning.

PI controller with PSO

The IMC and ZN-based controller simulation results emphasize that the PI controller is the apt controller for this production process. In this part, the PI controller tuning is obtained with particle swarm optimization algorithm.50 iterations are considered for a population size of 50. The Inertia weight is taken as 0.9. Other parameters used for optimization are given in Table 7.

Table 7. Variables in PSO.

Variables	Values
Dimension	2
Population	50
Iterations	50
Cognitive coefficient, c1	0.12
Social coefficient, c2	1.2
Inertia weight	0.9

Comparative study of PSO PI controller with and Zeigler Nichols tuning PI controller

PSO PI controller based on evolutionary algorithm gives excellent response for setpoints without any oscillations, and settling time is very small for a load disturbance compared to Zeigler Nichols and IMC PI controllers. A comparison of IMC-PI, PSO, and ZN PI controllers for setpoint tracking and disturbance

rejection comparison is shown in Figure 8. The analysis in Table 8 tells that the PSO PI controller settles at 45 s without any oscillations and settles down faster for the disturbance of magnitude 0.5 applied at t = 800 s.

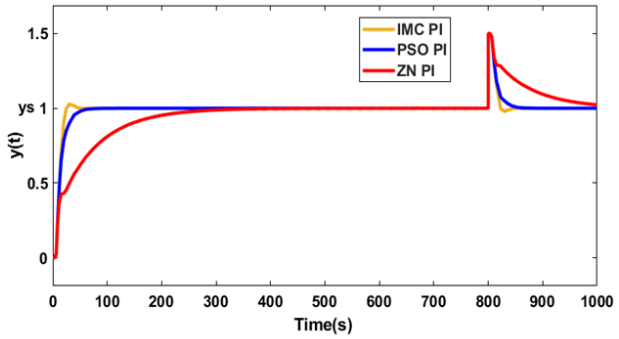

Figure 8. Setpoint tracking and disturbance rejection comparison of the PSO PI controller and comparison with the IMC and ZN PI controllers.

Table 8. Setpoint tracking and disturbance rejection comparison.

Controller Types	Unit setpoint change at $t = 0\ s$				Load perturbation of magnitude 10 at $t = 800\ s$			
	t_p (s)	t_s (s)	M_p (%)	ϵ_{ss}	t_p (s)	t_s (s)	M_p (%)	ϵ_{ss}
IMC PI	30	45	0	0	0	38	0	0
ZN PI	0	300	0	0	0	200	0	0
PSO PI	0	45	0	0	0	38	0	0

The comparative study of different classical control strategies shows that the PSO PI controller exhibits excellent setpoint tracking and disturbance rejection compared to other modeling strategies. Besides that, compared to the PID controller, the PI controller suites better for this particular process.

CONCLUSION

A comparative study of different classical control strategies was done for the cumene production process as a part of modeling and control of the process. As a system with a large amount of uncertainty, the state space matrices of the cumene production process were obtained from the COMSOL design using MATLAB Livelink. The IMC/based PI and PID controllers are derived for the performance analysis, and the controller with analytical rules is compared with that of Zeigler Nichols tuning and Particle swarm optimization. The single-tuning parameter τ_c is adjusted in the PI and PID controller with the analytical rules for the optimum response. The integral terms can be further adjusted for improved disturbance rejection and setpoint tracking. The P, PI, and PID controllers of Zeigler Nichols tuning are designed with process curve approximations and it is found that the PI controller has the best approximation. The evolutionary computation technique is used for the PID controller setting to check the improvement in response. Particle swarm optimization is used for the PID tuning, and it is observed that the PI controller with PSO shows better disturbance rejection and setpoint tracking with a minimum settling time.

ACKNOWLEDGMENT

The authors thank the team HOCL, Kochi, Kerala, for their timely support in completing the work. They would like to thank all the anonymous referees for their suggestions for improving this paper.

ABBREVIATIONS

FOPDT	First Order Plus Dead Time
SOPDT	Second Order Plus Dead Time
IMC	Internal Model Control
PSO	Particle Swarm Optimization

REFERENCES

[1] S. Skogestad, J. Process Control. 13 (2003) 291–309. https://doi.org/10.1016/S0959-1524(02)00062-8.

[2] J.G. Ziegler, N.B. Nichols, Trans. ASME. 64 (1942) 759–765. https://doi.org/10.1115/1.4019264.

[3] D.E. Rivera, M. Morari, S. Skogestad, Ind. Eng. Chem. Process Des. Dev. 25 (1986) 252–265. https://doi.org/10.1021/i200032a041.

[4] B.D. Tyreus, W.L. Luyben, Ind. Eng. Chem. Res. 31 (1992) 2625–2628. https://doi.org/10.1021/ie00011a029.

[5] K.J. Astrom, P.I.D. Controllers, Theory, Design, and Tuning, Instrument Society of America, Research Triangle Park, North Carolina (1995).

[6] K.J. Astrom, T. Hägglund, J. Process Control. 14 (2004) 635–650. https://doi.org/10.1016/j.jprocont.2004.01.002.

[7] R. Eberhart, J. Kennedy, Particle Swarm Optimization, in Proceedings of the IEEE International Conference on Neural Networks, Citeseer, (1995) 1942–1948.

[8] W. Zeng, W. Zhu, T. Hui, L. Chen, J. Xie, T. Yu, Nucl. Eng. Des. 360 (2020) 110513. https://doi.org/10.1016/j.nucengdes.2020.110513.

[9] F. Marini, B. Walczak, Chemom. Intell. Lab. Syst. 149 (2015) 153–165. https://doi.org/10.1016/j.chemolab.2015.08.020.

[10] D. Wang, D. Tan, L. Liu, Soft Comput. 22 (2018) 387–408. https://doi.org/10.1007/s00500-016-2474-6.

[11] F. Mahmoudian, A.H. Moghaddam, S.M. Davachi, Can. J. Chem. Eng. 100 (2022). 90–102.

https://doi.org/10.1002/cjce.24072.

[12] A.H. Moghaddam, J. Shayegan, J. Sargolzaei, J. Taiwan Inst. Chem. Eng. 62 (2016) 150–157. https://doi.org/10.1016/j.jtice.2016.01.024.

[13] A. HedayatiMoghaddam, H. Hazrati, J. Sargolzaei, J. Shayegan, A, Appl. Water Sci. 7 (2017) 2753–2765. doi:10.1007/s13201- 016-0503-3.

[14] H. Vaziri, A. HedayatiMoghaddam, S.A. Mirmohammadi,Chem. Pap. 74 (2020) 3311–3324. doi:10.1007/s11696-020-01162-w.

[15] S. Bennett, Annu. Rev. Control 25 (2001) 43–53. https://doi.org/10.1016/S1367-5788(01)00005-0.

[16] V.M. Lakshmanan, A. Kallingal, S. Sreekumar,, J. Indian Chem. Soc. 99 (2022) 100730. https://doi.org/10.1016/j.jics.2022.100730.

[17] V.M. Lakshmanan, A. Kallingal, S. Sreekumar,, J. Control Decis. (2022) 1–11. https://doi.org/10.1080/23307706.2022.2146009

[18] V. Gera, M. Panahi, S. Skogestad, N. Kaistha, Ind. Eng. Chem. Res. 52 (2013) 830–846. https://doi.org/10.1021/ie301386h.

[19] A. Chudinova, A. Salischeva, E. Ivashkina, O. Moizes, A. Gavrikov, Procedia Chem. 15 (2015) 326–334. https://doi.org/10.1016/j.proche.2015.10.052.

[20] V.M. Lakshmanan, A. Kallingal, S. Sreekumar, Int. J. Chem. React. Eng. (2021) 1–17. https://doi.org/10.1080/23307706.2022.2146009.

[21] X. Yang, S. Wang, B. Li, Y. He, H. Liu, Fuel 274 (2020) 117829. https://doi.org/10.1016/j.fuel.2020.117829.

[22] H.M. Park, Int. J. Heat Mass Transfer 116 (2018) 520–531. https://doi.org/10.1016/j.ijheatmasstransfer.2017.09.035.

[23] U.M. Nath, C. Dey, R.K. Mudi, IETE J. Res. (2021) 1–21. https://doi.org/10.1080/03772063.2021.1874839.

[24] S.K. Pradhan, D. Acharya, D.K. Das, Ann. Nucl. Energy 165 (2022) 108675. https://doi.org/10.1016/j.anucene.2021.108675.

[25] Z. Nie, Z. Li, Q. Wang, Z. Gao, J. Luo,Int. J. Robust Nonlinear Control. (2021). https://doi.org/10.1002/rnc.5848.

[26] S. Sreekumar, A. Kallingal, L.V. Mundakkal, Chem. Ind. Chem. Eng. Q. 28(2) (2022) 127–134. https://doi.org/10.2298/CICEQ200911031S.

[27] P.G. Junqueira, P.V Mangili, R.O. Santos, L.S. Santos, D.M. Prata, Chem. Eng. Process. 130 (2018) 309–325. https://doi.org/10.1016/j.cep.2018.06.010.

[28] M.L. Vinila, K. Aparna, S. Sreepriya, in Int. Conf.Intell.Comput.Inf.Control Syst., Springer, 2019: pp. 201–208. https://doi.org/10.1007/978-3-030-30465-2_23.

VINILA MUNDAKKAL LAKSHMANAN[1,2]

APARNA KALLINGAL[1]

SREEPRIYA SREEKUMAR[1,2]

[1]Department of Chemical Engineering, National Institute of Technology Calicut, Kozhikode, Kerala, India

[2]Department of Robotics and Automation, Adi Shankara Institute of Engineering and Technology, Kalady, India

NAUČNI RAD

UNUTRAŠNJI MODEL KONTROLE KUMENSKOG PROCESA KORIŠĆENJEM ANALITIČKIH PRAVILA I EVOLUCIONOG RAČUNARSTVA

Kumen (izopropilbenzen) je prekursor za proizvodnju mnogih organskih hemikalija i razređivača za boje i lakove. Njegov proizvodni proces uključuje složenu kinetiku. Različite klasične strategije upravljanja za kumenski reactor su implementirane i upoređene u ovom procesu. Za ovakav sistem sa velikim stepenom slobode, usvojen je novi pristup za izdvajanje modela u prostora stanja iz programskog paketa COMSOL Multiphisics. Za sistem su izvedeni PI i PID kontroleri zasnovani na internoj modernoj kontroli (IMC). Da bi se izvelo podešavanje kontrolera korišćenjem Skogestad polupravila, sistem je sveden na strukturu modela FOPDT i SOPDT. Integralno vreme je modifikovano za praćenje zadate tačke i brže odbacivanje smetnji. Iz analize se može konstatovati da PI kontroler više odgovara ovom specifičnom procesu. Algoritam za optimizaciju roja čestica (PSO), evoluciona tehnika izračunavanja, takođe se koristi za podešavanje PI podešavanja. Upoređeni su PI kontroleri sa podešavanjem IMC, Zeigler Nichols i PSO i može se zaključiti da se PSO PI kontroler smiruje za 45 s bez ikakvih oscilacija i brže se slaže za poremećaj veličine 0,5 primenjen na t = 800 s. Međutim, on je računarski intenzivan u poređenju sa drugim strategijama kontrolera.

Ključne reči: IMC PI, IMC PID, Skogestad polupravilo, Zeigler Nichols, PSO PI.

CI&CEQ
Chemical Industry & Chemical Engineering Quarterly

Available online at
Association of the Chemical Engineers of Serbia *AChE*
www.ache.org.rs/CICEQ

Chem. Ind. Chem. Eng. Q. 30 (2) 99–110 (2024) CI&CEQ

BEATRIZ MENOSSI RIBEIRO[1]
LEANDRO DA RIN DE SANDRE JUNIOR[1]
GIANCARLO DE SOUZA DIAS[1]
MICHELLE DA CUNHA ABREU XAVIER[2]
ALEX FERNANDO DE ALMEIDA[3]
ELDA SABINO DA SILVA[4]
ALFREDO EDUARDO MAIORANO[4]
RAFAEL FIRMANI PERNA[1]
SERGIO ANDRES VILLALBA MORALES[2]

[1]Institute of Science and Technology, Federal University of Alfenas, Poços de Caldas-MG, Brazil

[2]Bioprocess Engineering and Biotechnology Department, Federal University of Tocantins Gurupi-TO, Brazil

[3]Food Engineering Department, Federal University of Tocantins, Palmas-TO, Brazil

[4]Industrial Biotechnology Laboratory, Institute for Technological Research University City, São Paulo-SP, Brazil

SCIENTIFIC PAPER

UDC 544.47:547:66.02:577.15

CROSS-LINKED WHOLE CELLS FOR THE SUCROSE TRANSFRUCTOSYLATION REACTION IN A CONTINUOUS REACTOR

Article Highlights

- Glutaraldehyde-crosslinked fungi cells were used as biocatalysts in a packed bed reactor (PBR)
- The highest activity was presented by biocatalysts prepared by cross-linking at 200 rpm and 45 min
- The behavior of the cells' activity at several operational parameters of the PBR was obtained
- The biocatalyst achieved high operational stability for 12 h of reaction in the PBR
- The biocatalyst showed a high potential for the production of fructooligosaccharides in PBR

Abstract

Fructooligosaccharides (FOS) are fructose oligomers beneficial to human health and nutrition for prebiotic sugars. Their production occurs by a transfructosylation reaction in sucrose molecules catalyzed by fructosyltransferase enzymes (FTase, E.C.2.4.1.9) adhered to microbial cells. The purpose of this work was to study the preparation, enzymatic activity, and stability of glutaraldehyde-crosslinked Aspergillus oryzae IPT-301 cells used as a biocatalyst for the transfructosylation reaction of sucrose in a packed bed reactor (PBR), aiming at FOS production. The highest transfructosylation activity (A_T) was presented by the biocatalyst prepared by cross-linking at 200 rpm and 45 min. The highest A_T in the PBR was obtained at 50 °C, with flow rates from 3 mL min^{-1} to 5 mL min^{-1} and sucrose concentrations of 473 g L^{-1} and 500 g L^{-1}. The enzymatic kinetics was described using the Michaelis-Menten model. Finally, the biocatalyst showed constant A_T of approximately 75 U g^{-1} and 300 U g^{-1} for 12 h of reaction in the PBR operating in continuous and discontinuous flow, respectively. These results demonstrate a high potential of glutaraldehyde-crosslinked A. oryzae IPT-301 cells as heterogeneous biocatalysts for the continuous production of FOS in PBR reactors.

Keywords: fructosyltransferase, whole cells, heterogeneous biocatalysts, packed bed reactors, fructooligosaccharides.

Fructooligosaccharides (FOS) are fructose oligomers produced by the transfructosylation reaction of sucrose catalyzed by fructosyltransferase (FTase, E.C.2.4.1.9), in which fructose molecules are transferred to the β-(2→1) position of the sucrose molecule, producing FOS and glucose [1,2].

These sugars are widely used in food fabrication as supplements and substitutes for sucrose because of their high sweetening power and numerous health benefits since they are low-calorie and non-cariogenic, improve intestinal function, and help reduce total serum cholesterol [1,3,4]. Nevertheless, despite the high worldwide demand for FOS, its large-scale production

Correspondence: R.F. Perna, Institute of Science and Technology, Federal University of Alfenas, José Aurélio Vilela Road 11999, km 533, Poços de Caldas-MG, Zip Code 37715-400, Brazil.
E-mail: rafael.perna@unifal-mg.edu.br
Paper received: 20 December, 2022
Paper revised: 16 April, 2023
Paper accepted: 22 June, 2023

https://doi.org/10.2298/CICEQ221220015M

is limited by the use of soluble enzymes as biocatalysts since they have low stability and cannot be reused or applied in packed bed reactors (PBR), which can decrease the production costs of these sugars [2,5–8].

Currently, the main strategy to prepare more stable biocatalysts for the transfructosylation reaction of sucrose has been the immobilization of extracellular microbial FTases on solid matrices [9,10]. However, extracellular enzymes deactivate rapidly during immobilization, and the solid matrices can limit enzymatic activity by causing transport limitations to the molecules of reactants and products or by modifying the microenvironment of the enzyme [2,9–11]. In this sense, whole cells with transfructosylation activity can be more advantageous biocatalysts since they have mycelial enzymes naturally immobilized on their producer microorganisms, decreasing enzyme losses and operational costs associated with manipulating extracellular enzymes and matrices [3,12].

Cells from fungi like *Xanthophyllomyces* sp. and *Aspergillus* sp., and mainly from the strain *Aspergillus oryzae* IPT-301, have shown great enzymatic activity during the transfructosylation reaction of sucrose in batch reactors [1,3,4,13–16]. However, these cells' thermal and operational stability must be improved, aiming its use in PBR reactors.

The immobilization of cells by entrapment or absorption can improve their stability during FOS production in batch reactors [7,13,17]. However, these immobilization techniques can reduce the enzymatic activity of the cell because of mass transport limitations [3,6,15,18]. In this sense, immobilization of cells by cross-linking is an important alternative since it does not use external materials as support, and the cross-linked cells showed great catalytic activity and stability in reaction batches [3]. The optimal pH and glutaraldehyde concentration to maximize the transfructosylation activity of glutaraldehyde-crosslinked *A. oryzae* IPT-301 cells were reported by Garcia *et al.* [3]. However, the enzymatic activity of these cells could still be improved by studying the effect of important cross-linking variables such as cross-linking time and agitation speed aiming its use in PBR reactors.

Currently, the use of free and immobilized cells in PBR reactors for FOS production has been explored shortly [5–7]. Furthermore, the use of cross-linked cells in this process has not been reported yet. This work aimed to prepare a stable heterogeneous biocatalyst with high activity for the transfructosylation reaction of sucrose in a PBR aiming for FOS production. For this, it evaluated the effect of agitation speed and time of cross-linking on the enzymatic activity of glutaraldehyde-crosslinked cells of *Aspergillus oryzae* IPT-301, as well as the enzymatic activity and stability of these cells as a function of reaction conditions in the PBR, such as flow rate, substrate concentration, and temperature.

MATERIALS AND METHODS

Materials

All chemical products used were of analytical grade. Yeast extract, sucrose, monopotassium phosphate (KH_2PO_4), manganese (II) chloride tetrahydrate ($MnCl_2.4H_2O$), and iron (II) sulfate heptahydrate ($FeSO_4.7H_2O$) were purchased from Labsynth® (Diadema, Brazil). Glutaraldehyde solution Grade I (25% in water), sodium borohydride ($NaBH_4$), sodium nitrate ($NaNO_3$), magnesium sulfate heptahydrate ($MgSO_4.7H_2O$), 3,5-dinitrosalicylic acid ($C_7H_4N_2O_7$), potassium sodium tartrate ($KNaC_4H_4O_6.4H_2O$), and tris(hydroxymethyl)aminomethane ($NH_2C(CH_2OH)_3$) were purchased from Dinamica® (Diadema, Brazil). The enzyme kit GOD-PAP for glucose determination was obtained from Laborlab® (Guarulhos, Brazil).

Biocatalyst production

Microorganism and production of the whole cells

Whole cells of *A. oryzae* IPT-301 were provided by the Institute for Technological Research (IPT-SP). Microbial growth was conducted by submerged culture in unbaffled Erlenmeyer flasks containing 50 mL of a sterilized culture medium with the following composition (in %, w v^{-1}): sucrose 15.0, yeast extract 0.5, $NaNO_3$ 0.5, KH_2PO_4 0.2, $MgSO_4.7H_2O$ 0.05, $MnCl_2.4H_2O$ 0.03, and $FeSO_4.7H_2O$ 0.001.[1] The pH of the medium was adjusted to 5.5 before sterilization. The flasks were inoculated with 0.5 mL of a spore suspension of 1 x 10^7 spores mL^{-1} and incubated in a rotary shaker (Tecnal® Brazil, model TE-4200) at 30 °C and 200 rpm for 64 h [1,3,5,15]. After cultivation, the culture broth was vacuum-filtered using a Whatman N° 1 filter paper to retain the whole cells with transfructosylation activity. The collected filter cake, containing the mycelial FTase, was used to prepare the biocatalyst into spherical particles with 2.58 ± 0.30 mm of diameter. The prepared biocatalyst was taken to cross-linking assays.

Cross-linking assays of the whole cells

The cross-linking assays for the biocatalyst preparation were conducted according to an adaptation of the methods reported by Gonçalves *et al.* [15] and Garcia *et al.* [3]. Initially, about 1.5 g of whole cells were added to a 250 mL Erlenmeyer flask, followed by 12.6 mL of a glutaraldehyde solution (25 wt % in water) previously dissolved in 137.4 mL of 0.2 mol L^{-1} tris-

acetate buffer (2.1% v v^{-1} of glutaraldehyde and pH 7.9). The flask was placed on an orbital shaker (Tecnal® Brazil, model TE-4200), wherein the cells were cross-linked at 25 °C and agitation speeds from 150 rpm to 250 rpm, with agitation times from 30 min to 90 min. These values were chosen according to optimal pH and glutaraldehyde concentrations reported in previous work [3] and after preliminary cross-linking assays. Afterward, 1.5 mL of sodium borohydride previously dissolved in a 1 x 10^{-3} mol L^{-1} sodium hydroxide p.a solution (100 g L^{-1}) was added, and the medium was maintained under reaction for an additional 30 min. The cross-linking cells were vacuum-filtered (Whatman n° 1 filter paper), washed with distilled water, and preserved under refrigeration at 4 °C in 0.2 mol L^{-1} tris-acetate buffer (pH 5.5) for further determination of the enzymatic activity. Subsequently, the glutaraldehyde-crosslinked cells which showed the highest activity were used in the PBR assays.

Characterization of the biocatalyst

The morphology of the cross-linked cells was determined by scanning electron microscopy (Zeiss EVO MA-10, Germany) operating with an acceleration voltage of 20 kV, a working distance of 10.1 mm, and a spot size of 390. The samples were firstly dried for 2 h at 60 °C in a Micromeritics Vap Prep 61, Sample Degas System. The BET surface area was determined by nitrogen physisorption on a Micromeritics Gemini VII Surface Area and Porosity analyzer.

Evaluation of the enzymatic activity of the biocatalyst in a packed bed reactor

Implementation of the packed bed reactor setting

The catalytic behavior of the biocatalyst was determined in a borosilicate-packed bed reactor (PBR) of 12 mm of internal diameter. The PBR was filled with biocatalyst beads (glutaraldehyde-crosslinked cells) of 2.6 ± 0.3 mm in mean diameter up to a height of 15 cm. The temperature of the PBR was controlled using a thermostatic bath with water recirculation (Tecnal® Brazil, model TE-2005), which pumped water through a borosilicate jacket coupled to the PBR. The sucrose solution was pumped through the bioreactor upwardly using a peristaltic pump (MS Tecnopon® Brazil, model LAP-101-3). The biocatalyst beads were introduced into the PBR (by the top) using a spatula, and their mass was kept constant for all experimental runs, aiming to keep enzyme loading constant. The PBR was operated in continuous and discontinuous flow (i.e., total recirculation of the exit effluent). A schematic representation of the PBR setting was shown in previous work [5].

Effect of operational parameters on the enzymatic activity of the biocatalyst

The effect of the volumetric flow rate on the transfructosylation activity of the biocatalyst was evaluated for a range from 1.0 mL min^{-1} to 5.0 mL min^{-1} at 50 °C. The effect of temperature on the transfructosylation activity was evaluated for a range from 30 °C to 60 °C at 1.0 mL min^{-1}. These tests were performed for 150 min at pH 5.5 and a sucrose concentration of 473 g L^{-1}.

The effect of substrate concentration on the transfructosylation activity of the biocatalyst was evaluated for a range from 200 g L^{-1} to 600 g L^{-1} at 50 °C, pH 5.5, and 1 mL min^{-1} for 150 min. The Michaelis-Menten model (Eq. (1)) was used to estimate the kinetic parameters by non-linear regression.

$$v = \frac{v_{max}[S]}{K_m + [S]} \quad (1)$$

where v is reaction speed (U g^{-1}), V_{max} is the maximum reaction speed reached under the condition of substrate saturation (U g^{-1}), $[S]$ is sucrose concentration (g L^{-1}), and K_m is the Michaelis-Menten constant (g L^{-1}).

Operational stability assays

The operational stability of the biocatalyst was determined for 720 min at 50 °C, pH 5.5, sucrose concentration of 473 g L^{-1}, and flow rate of 1.0 mL min^{-1}. The experiments were carried out in the PBR operating in ascendant flow in continuous and discontinuous configuration.

Determination of external mass transfer parameters

The external mass transfer coefficient (k_c) and the Sherwood (Sh), Schmidt (Sc), and particle Reynolds (Re_p) numbers were calculated using Eqs. (2), (3), (4), and (5), respectively [19,20].

$$k_c = \frac{Sh \cdot D_{AB}}{d_p} \quad (2)$$

$$Sh = 2 + 0.6 Re_p^{1/2} Sc^{1/3} \quad (3)$$

$$S_c = \frac{v}{D_{AB}} \quad (4)$$

$$Re_p = \frac{U \cdot d_p}{v} \quad (5)$$

where d_p is the biocatalyst particle diameter (m), v is the kinematic viscosity (m^2 s^{-1}), U is reactant fluid flow velocity (m s^{-1}), and D_{AB} is the substrate diffusion coefficient (A) in the fluid (B), expressed in m^2 s^{-1}.

The mass diffusion coefficient (D_{AB}) was estimated using Eqs. (6–8), where T is the temperature of the solution (K), μ is the dynamic viscosity of the solution (cP), MM is the molar mass (g mol^{-1}), X_A is the molar fraction of the substrate, X_B is the molar fraction of the solvent, and D_{0BA} and D_{0AB}(m s^{-1}) are the diffusion coefficients under the condition of infinite dilution of the solvent in the solute (substrate) and of the solute in the solvent, respectively [5,21].

$$D_{AB} = X_A D_{0BA} + X_B D_{0AB} \quad (6)$$

$$D_{0BA} = \frac{9.40x10^{-11}T}{MM_B^{1/3}\mu_A} \quad (7)$$

$$D_{0AB} = \frac{9.40x10^{-11}T}{MM_A^{1/3}\mu_B} \quad (8)$$

The Re_p was determined using a fluid flow velocity of 2.1 x 10^{-3} m s^{-1}. The sucrose solution was considered a diluted solution since the concentration used (473.0 g L^{-1}) corresponds to a sucrose dry substance content of 32.7% (w w^{-1}), which is inside the interval defined for an ideal solution [22]. The physical properties of liquid water and a solution of sucrose at 473 g L^{-1} and 50 °C were used to calculate the external mass transfer coefficients [21,23]. The dynamic viscosity of the sucrose solution was obtained using a Brookfield viscometer, model DV-I Prime with spindle 61 and agitation of 100 rpm.

Quantification of the enzymatic activity

The enzymatic activity was determined according to the method reported by Dias *et al.* [5]. The effluent sample was collected from the bioreactor and immediately incubated in boiling water for 10 min and ice bath for 5 min. The unit of transfructosylation activity was defined as the amount of enzyme that transfers one micromole of fructose per minute per gram of dry biocatalyst under the chosen experimental condition [3,5,15]. The concentration (μmol L^{-1}) of transfructosylated fructose (F_T) present in the reaction medium was calculated by Eq. (9) from the concentrations of glucose (G) and reducing sugars (RS), which were estimated using the enzymatic Glucose kit (GOD-PAP) and 3,5-dinitrosalicylic acid (DNS) method, respectively [1,10,11].

$$F_T = 2[G] - [RS] \quad (9)$$

To obtain the dry biocatalyst, the cross-linked whole cells were abundantly washed with distilled water after each assay, then vacuum-filtered in a Whatman n°1 filter and maintained in a drying oven (ProLab®, Brazil) at 60 °C until a constant mass was obtained.

Statistical analysis

All experiments were performed in triplicate. The analysis of the means for the cross-linking assays was performed by Tukey's honest significant difference (HSD) test, with a confidence interval of 95%.

RESULTS AND DISCUSSION

Physical properties of the biocatalyst

The surface area of the biocatalyst was 2.12 ± 0.01 m^2 g^{-1}. Dias *et al.* [5] reported that free cells of *A. oryzae* IPT-301 show a surface area of approximately 2.79 m^2 g^{-1}. It suggests that the cross-linking process of the cells with glutaraldehyde did not modify their texture significantly. It is worth mentioning that although the surface area of the cross-linked cells is considerably lower than that of solid matrices, such as silica gel (approx. 320 m^2 g^{-1}) used for immobilization of extracellular FTase, the activity of mycelial enzymes present in the cells has shown to be considerably higher than the activity of extracellular FTase immobilized by adsorption or covalent bonding on solid matrices [1,3,9,10,15,24]. Additionally, the use of cross-linked cells as biocatalysts avoids the addition of external solid matrices to the reaction media.

Figure 1 shows that the biocatalyst morphology mainly consists of a network of non-septate hyphae without the presence of fruiting bodies, spores, and a homogeneous mycelium, which is characteristic of the mycelial growth of a filamentous fungus of the genus *Aspergillus*. In general, hyphae are present in filamentous fungi due to stages of spore germination, hyphal growth, branching, and fungal differentiation [25]. However, the surface of the cross-linked cells showed a more homogeneous distribution of filaments than that shown by the free cells reported by Dias *et al.* [5]. It could be attributed to the cluster formed by the hyphae network during the cross-linking process, which reduces hyphae spacing in the cells. Hyphae spacing and distribution depend on cell growth and immobilization conditions [26,27]. The formation of cross-linked multimolecular complexes of enzyme and mycelial material, promoted by glutaraldehyde, occurs through formation of Schiff bases bonds (imine groups) between glutaraldehyde aldehyde groups and amino groups of the microbial cells, which reduces the spacing between the fungus hyphae and strengthens the interaction between enzyme and mycelium, causing conformational and morphology changes at protein and cross-linked cells [28–30]. In turn, these changes may increase the exposure of biocatalyst active sites and reduce substrate molecules' transport limitations, increasing the catalytic efficiency of the mycelial enzyme [3,31].

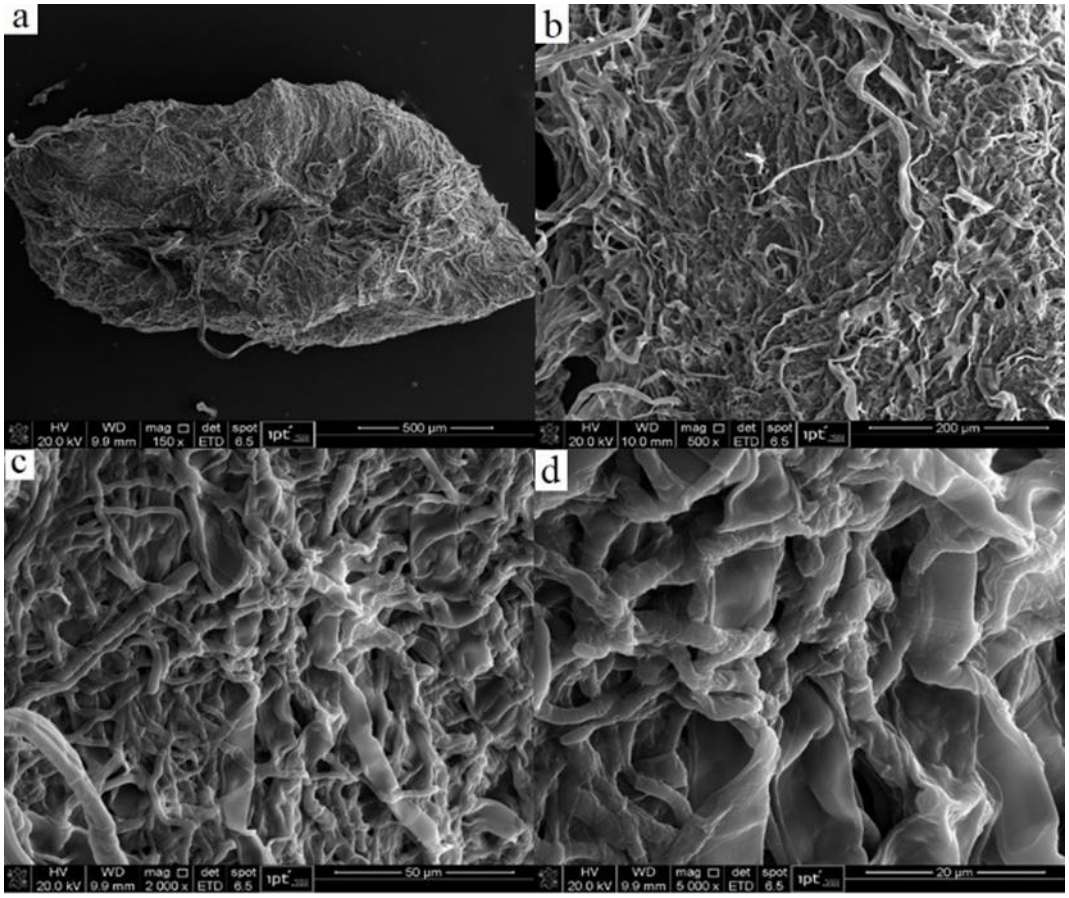

Figure 1. Micrographs of the cross-linked cells of A. oryzae IPT-301 with a magnification of (a) 150x, (b) 500x, (c) 2000x, and (d) 5000x.

Effect of cross-linking variables on biocatalyst activity

The effects of agitation speed and time during cell cross-linking on the biocatalyst activity were studied individually since preliminary statistical tests showed that both variables are independent. In the agitation speed assays, the highest transfructosylation activity (A_T) was achieved by the cells cross-linked at an agitation speed of 200 rpm, further confirmed by Tukey's HSD test (Figure 2a). Previously, Garcia *et al.* [3] had reported high A_T of *A. oryzae* IPT-301 cells cross-linked with glutaraldehyde at 200 rpm. However, the influence of agitation speed was not studied in their work. The cells cross-linked at agitation speeds of 150 rpm and 250 rpm showed the lowest A_T (below 500 U g^{-1}). The low A_T at 150 rpm could be attributed to the low mass transfer rate of the species, which reduces the effective contact between glutaraldehyde and the microbial cells, affecting the cross-linking efficiency [32,33]. On the other hand, the low A_T at 250 rpm could be attributed to an elevated shear rate on the cells caused by the high agitation speed, which can prevent cell cross-linking and the formation of bonds between enzymes and cells [34,35]. Furthermore, high agitation speeds can also produce a vortex in the vessel, which reduces the effective mixture volume and affects cell cross-linking [36].

In the agitation time assays, the highest A_T (approximately 979 U g^{-1}) was presented by the cells cross-linked for 45 min, also verified by Tukey's HSD test (Figure 2b). Similarly, Garcia et al. [3] reported that cells of *A. oryzae* IPT-301 cross-linked with glutaraldehyde for 60 min showed transfructosylation activities of approximately 986 U g^{-1}. Also, Gonçalves et al. [15] reported that cells cross-linked for 60 min and then entrapped in calcium alginate showed activity of approximately 817 U g^{-1}. Therefore, the results obtained in this work indicate an important time reduction in the cell immobilization process, which is favorable for enzymatic activity since long cross-linking times can cause enzyme denaturation because of the high glutaraldehyde reactivity [37].

Until the development of this work, only two works were found in literature about the cross-linking of whole cells with transfructosylation activity, and none of these explored the influence of agitation speed and cross-linking time on cell activity [11,15]. Gonçalves et al. [15] evaluated the stability of *A. oryzae* IPT-301 cells immobilized by cross-linking followed by entrapment in alginate. Garcia et al. [11] determined the optimal pH and glutaraldehyde concentration to maximize the activity of cross-linked *A. oryzae* IPT-301 cells. Therefore, the influence of agitation speed and cross-

linking time on the activity of cross-linked *A. oryzae* IPT-301 cells reported in this work is important original information for synthesizing novel heterogeneous biocatalysts with high enzymatic activity aiming at FOS production.

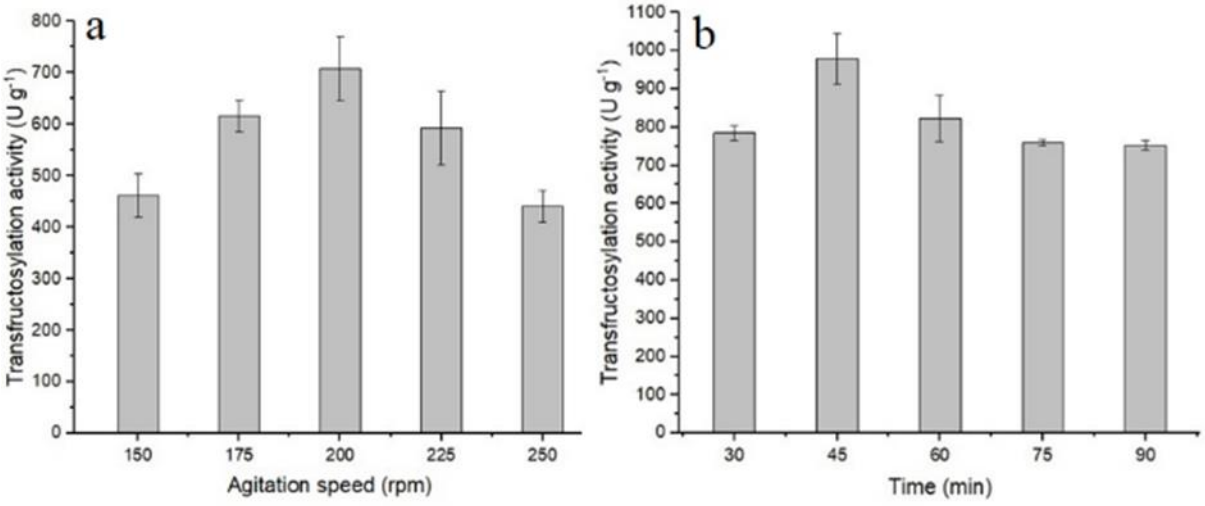

Figure 2. Effect of agitation speed (a) and effect of agitation time (b) during cell cross-linking on the transfructosylation activity of the biocatalyst.

Effect of the flow rate and temperature on the enzymatic activity of the biocatalyst

For all flow rates, the highest enzymatic activities of the biocatalyst in the PBR were obtained at the reaction time interval from 50 min to 100 min (Figure 3a). The highest A_T was obtained at the highest flow rate (5 mL min^{-1}), while the lowest A_T was obtained at the lowest flow rate (1 mL min^{-1}). Although higher flow rates provide a lower residence time in the PBR, they also allow a reduction in the transport limitations of the species on the external biocatalyst surface since higher flow velocities reduce the boundary layer in the catalyst beads, allowing faster contact between the substrate molecules and the active sites of the biocatalyst [5,20]. Conversely, the biocatalyst tested at 1 mL min^{-1} showed the lowest activity decrease, and the A_T decreased faster as the flow rate increased. This behavior could be attributed to enzyme drag at higher flow rates, as also reported by Dias *et al.* [5] for the sucrose transfructosylation reaction in a PBR catalyzed by free *A. oryzae* IPT-301 cells.

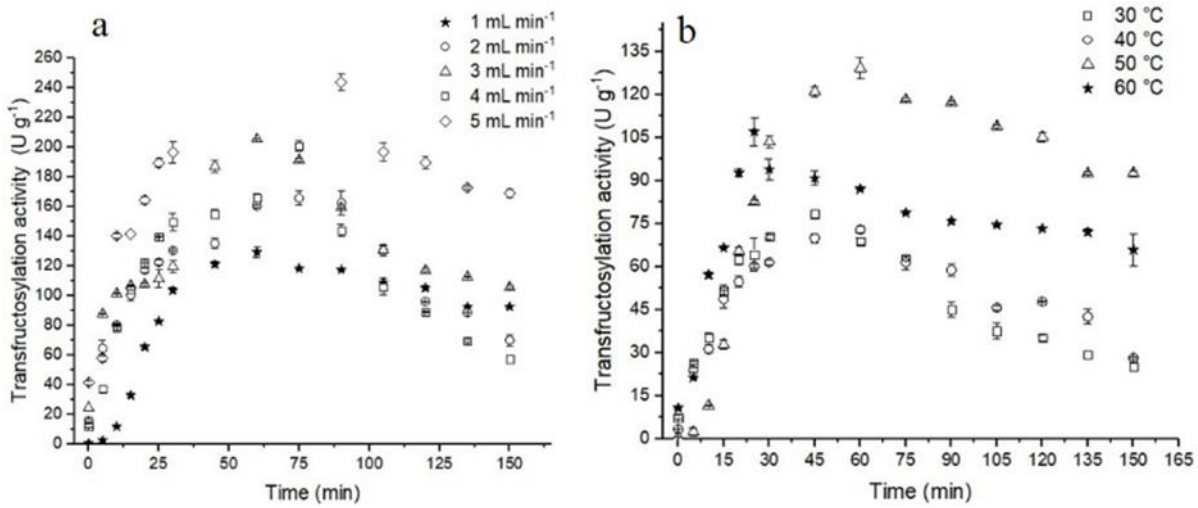

Figure 3. Effect of flow rate (a) and effect of reaction temperature (b) on the transfructosylation activity of the biocatalyst.

The highest A_T of the biocatalyst in the PBR was obtained at 50 °C, and the lowest A_T was obtained at 30 °C (Figure 3b). It can be explained by the higher frequency of collisions between substrate molecules and active sites at higher temperatures. The temperature increase enables sucrose molecules to reach the activation energy, consequently increasing the enzymatic reaction rate [3,38,39]. However, the

biocatalyst showed lower A_T for the reactor operated at 60 °C, which could be attributed to a faster thermal denaturation of enzymes at higher temperatures [24,40,41]. In thermal denaturation, the molecular interactions that maintain the force balance (hydrogen bonds, hydrophobic interactions, and van der Waals forces) of the native protein are disrupted, which affects the tertiary structure of the enzyme, causing an activity decay [24,40,41].

Additionally, for the reaction at 50 °C, proximity to the steady state was observed at about 135 min (Figure 3b). Similarly, Dias *et al.* [5] reported that free *A. oryzae* IPT-301 cells showed the highest enzymatic activity at 50 °C and steady-state at 25 min of reaction in a PBR. These results suggest that the cross-linking process did not alter the effect of temperature on the cells' activity.

Effect of sucrose concentration on the enzymatic activity of the biocatalyst and kinetics parameters

The highest A_T was presented by the reaction operated at initial sucrose concentrations of 473 g L^{-1} and 500 g L^{-1}. Similarly, Garcia *et al.* [3] reported that cross-linked cells of *A. oryzae* IPT-301 showed the highest A_T at 473 g L^{-1} in a batch reactor. It suggests that the substrate concentration effect on the A_T of the cross-linked cells was not affected by their applicability in the PBR. The lowest activities were observed for sucrose concentrations of 500 g L^{-1} and 600 g L^{-1}. Similarly, Dias *et al.* [5] reported a decrease in enzymatic activity at sucrose concentrations above 573 g L^{-1}, which can be attributed to inhibition by the substrate [42]. It suggests that A_T reduction at high substrate concentrations in the PBR was similar for both the free and cross-linked cells. Figure 4a also shows that a transition from transient to steady-state occurred at about 120 min of reaction for all tested sucrose concentrations.

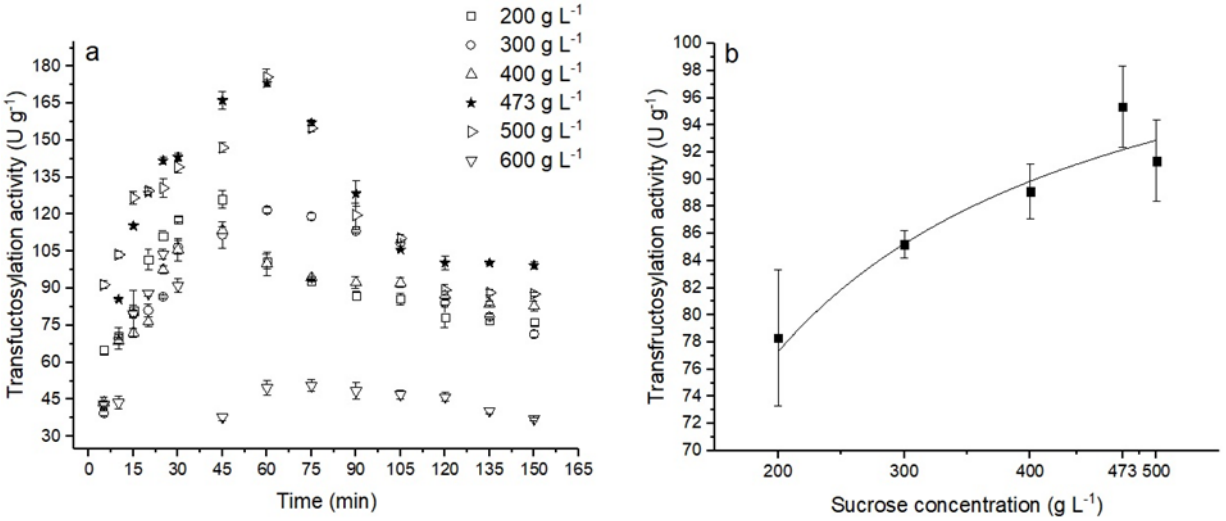

Figure 4. (a) Effect of sucrose concentration on the transfructosylation activity of the biocatalyst (b) and Michaelis-Menten model adjustment.

The A_T obtained in the assays of the substrate concentration effect was successfully adjusted to the Michaelis-Menten model (Figure 4b). This model was used because of its simplicity and wide applicability, and aimed to compare the kinetics parameters of the transfructosylation reaction on the cross-linked cells in the PBR with data reported for the same reaction on free cells in batch and PBR reactors and with the reaction catalyzed on cross-linked cells in batch reactors [3,5]. The kinetic parameters for the A_T shown by the biocatalyst are listed in Table 1. The V_{max} obtained in the PBR was lower than that reported by Garcia *et al.* [3] for a similar biocatalyst tested in a batch reactor (Table 1). This behavior was also reported for free *A. oryzae* IPT-301 cells tested in batch and PBR reactors and can be attributed to mass transport limitations in the PBR at low flow rates [3,5]. The K_m obtained for the cross-linked cells in the PBR was also lower than that obtained in a batch reactor [3]. However, it showed the opposite behavior for the free *A. oryzae* IPT- 301 cells tested in batch and PBR reactors [3,5]. It suggests that cross-linking of the cells is advantageous for application in PBR reactors. Additionally, previous work demonstrated that cross-linking of the *A. oryzae* IPT-301 cells with glutaraldehyde also increases substrate-enzyme affinity during the transfructosylation reaction in batch reactors [3]. Therefore, the kinetics parameters obtained with the Michaelis-Menten model can be significantly useful for further modeling of the transfructosylation reaction of sucrose in a PBR, catalyzed on cross-linked cells of *A. oryzae*-IPT-301, aiming FOS production.

Table 1. Kinetic parameters of the Michaelis-Menten model obtained for the transfructosylation activity of A. oryzae IPT-301 cells.

Kinect parameters	Biocatalyst/reactor			
	Cross-linked cells in a PBR	Cross-linked cells in a batch reactor	Free cells in a PBR	Free cells in a batch reactor
V_{max} (U g^{-1})	106.90 ± 4.15	956.06	634 ± 85	817.50
K_m (g L^{-1})	74.21 ± 16.14	98.50	157 ± 68	121.50
R^2	0.92	0.95	0.97	0.91
Reference	This work	[3]	[5]	[3]

Operational stability

Initially, for the PBR operating in a continuous flow, the biocatalyst showed a fast increase in A_T up to approximately 190 U g^{-1} (Figure 5). Nonetheless, after 60 min of reaction, the A_T decreased rapidly and stabilized at approximately 75 U g^{-1} after 180 min. The A_T decrease could be attributed to enzymes' drag on the cell surface. After that, the A_T stayed practically constant for up to 12 h of reaction, suggesting great operational stability of the biocatalyst. Similarly, Dias *et al.* [5] reported that free *A. oryzae* IPT-301 cells showed constant enzymatic activity for 12 h of reaction in a PBR at 50 °C and flow rate of 5 mL min^{-1}, but they presented rapid deactivation at flow rates above 11 mL min^{-1}. On the other hand, in this work, in the PBR operating with discontinuous flow, the A_T increased along the reaction time and stabilized at approximately 300 U g^{-1} after 9 h of reaction. It could be attributed to the constant recycling of dragged enzymes back to the PBR in the discontinuous flow configuration. This behavior was also reported for free *A. oryzae* IPT-301 cells used in a PBR with continuous and discontinuous descendent flow at 11.5 mL min^{-1} [5]. These results suggest that the biocatalyst prepared in this work is stable for the transfructosylation reaction of sucrose, and it has a high potential to catalyze the large-scale production of FOS in a PBR.

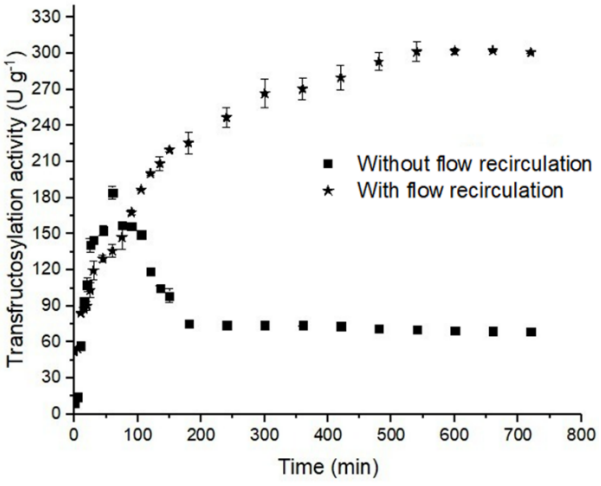

Figure 5. Operational stability of the biocatalyst in the PBR operated in continuous and discontinuous flow.

Recently, Garcia *et al.* [3] reported that cross-linked *A. oryzae* IPT-301 cells are considerably more stable than free cells in batch reactors. In that study, the cross-linked cells showed 88.9% of their initial transfructosylation activity after 12 sequential reaction batches of 1 h, while free cells only retained 50.3% of their initial activity [3]. Aldehyde groups of glutaraldehyde can act as an intramolecular crosslinker by reacting with two vicinal primary amine groups within a protein, or it can promote intermolecular cross-linking between two primary amine groups of two neighboring biomolecules by the formation of Schiff bases (imine groups) [31,43,44]. Therefore, the increase in enzymatic activity and stability after treatment with glutaraldehyde in whole cells of *A. oryzae* IPT-301 may be due to the formation of inter- or intramolecular cross-links that can cause conformational changes in the mycelial enzyme and, consequently, allow greater contact between the active sites of the protein and substrate molecules [3].

Furthermore, the higher stability of cross-linked cells can be more advantageous for FOS production when PBR reactors are used since the continuous flow offer a higher effective contact between reactants and biocatalyst [5,7]. Zambelli *et al.* [7] immobilized bacterial whole cells by entrapment in alginate and tested it in batch and PBR reactors for FOS production. The authors reported that the FOS yield was 1.7 times higher in a PBR than in a batch reactor. Similarly, Dias *et al.* [5] reported that free cells of *A. oryzae* IPT-301 showed enzymatic productivity of approximately 40 times the productivity of batch reactors. The results showed in this work are the first concerning the use of cross-linked cells as stable biocatalysts for the transfructosylation reaction of sucrose in a PBR, which is a key strategy to enable the large-scale production of FOS.

Mass transfer and kinetics regimes

Figure 6 shows that for flow rates from 1 mL min^{-1} to 4 mL min^{-1}, the transfructosylation activity of the biocatalyst in the PBR was limited by substrate diffusion [5,20]. It indicates that the sucrose molecules were transported slowly through the boundary layer at the biocatalyst surface up to the active sites, which decreases A_T. These results explain the low V_{max} obtained in the PBR (Table 1). Also, as the kinetic parameters shown in Table 1 were determined at 1 mL min^{-1}, these are apparent kinetic parameters. On

the other hand, it can be seen that the A_T stayed practically constant at flow rates of 4 mL min^{-1} and 5 ml min^{-1}, suggesting that the change in flow velocity did not alter enzymatic activity. It indicates that the reaction could be kinetics-limited or limited by internal diffusion at this flow interval. However, because of the low surface area of the biocatalyst, which is related to the absence of porosity, the reaction could be considered kinetics-limited. It is worth mentioning that although high flow rates could be used in the kinetics studies to avoid external mass transfer limitations in the PBR, the lowest flow rate was used in those assays because the A_T showed higher instability as the flow rate increased (Figure 3a).

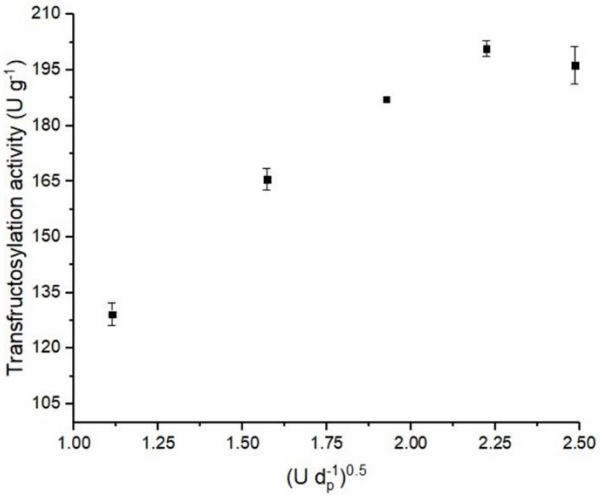

Figure 6. Regions of limitation by external mass transfer and by reaction kinetics.

The use of PBR reactors for FOS production has been explored shortly [5–7]. Therefore, there is a lack of mass transfer data in this process in the literature. However, it is known that the flow regime greatly influences the biocatalyst performance. According to the Reynolds number obtained, the PBR operated in laminar flow, suggesting a high influence of viscous forces on substrate flow (Table 2). The laminar flow is unfavorable for a proper mass transfer in the reactor. However, it is inevitable since the enzymatic reaction requires long residence times to reach high substrate conversion, and hence low flow rates must be used. Also, as shown in Figure 3a, low flow rates allow higher stability. The laminar regime was also used in the work of Dias *et al.* [5] for a PBR packed with free cells. Dias *et al.* [5] also reported lower enzyme stability at higher flow rates in their work. Furthermore, similar studies in a PBR for FOS production used flow rates below 1 mL min^{-1} [6,7]. The high Schmidt number obtained showed the great effect of viscosity on the laminar flow. Moreover, the Sherwood number indicates that the mass transfer in the PBR was predominantly convective, per the results shown in Figure 6. Finally, it was obtained a low coefficient of external mass transfer (k_c), which can be attributed to the high sucrose concentration (which results in a high fluid viscosity) and the low flow used for the transfructosylation reaction of sucrose on the cross-linked cells in the PBR. This behavior has also been reported for other enzymatic reactions tested in a PBR since enzymatic processes generally need high residence times because of their slow reaction kinetics [45,46]. These results demonstrate the importance of improving immobilization techniques, such as cross-linking of whole cells, for developing highly active and stable biocatalysts for the continuous enzymatic production of FOS at higher flow rates.

Table 2. Parameters of mass transfer and dimensionless numbers.

Parameters and dimensionless numbers	Value
Reynolds of particle – Re_p	1.058
Schmidt – Sc	6.64 x 10^6
Sherwood – Sh	118.027
Sucrose diffusion coefficient (A) in water (B) (D_{AB})	7.66 x 10^{-13} m^2 s^{-1}
Coefficient of external mass transfer (k_c)	3.51 x 10^{-8} m s^{-1}

CONCLUSION

Glutaraldehyde-crosslinked *A. oryzae* IPT-301 cells were successfully prepared and tested as biocatalysts for the transfructosylation reaction of sucrose in a PBR. The effects of the agitation speed and time of cross-linking on the biocatalyst activity were evaluated. The highest A_T was presented by cells cross-linked at 200 rpm for 45 min, which allowed the improvement of the biocatalyst preparation methodology. In the PBR operated with continuous flow, the highest A_T of the biocatalyst was obtained at 5 mL min^{-1}, 50 °C, and sucrose concentrations of 473 g mL^{-1} and 500 g mL^{-1}. Nevertheless, high flow rates should be avoided to reduce A_T loss along the time on stream. The A_T of the biocatalyst showed reaction kinetics and responses to variations in temperature and sucrose concentrations that were similar to the cross-linked cells used in the batch reactors, suggesting that it can be used in PBR systems without affecting their performance. Finally, the biocatalyst showed high operational stability for 12 hours of reaction. These results suggest a high

potential for applying the cross-linked *A. oryzae* IPT-301 cells as a biocatalyst for FOS production in PBR reactors.

ACKNOWLEDGMENT

The authors gratefully acknowledge the financial support from the National Council for Scientific and Technological Development - CNPq/ Brazil (Proc. 421540/2018-4 and Proc. 404912/2021-4), the Foundation for Research of the State of Minas Gerais (FAPEMIG/ Brazil, Proc. APQ-00085-21), and the Coordination for the Improvement of Higher Education Personnel (CAPES/ Brazil).

REFERENCES

[1] J.S. Cunha, C.A. Ottoni, S.A.V. Morales, E.S. Silva, A.E. Maiorano, R.F. Perna, Brazilian J. Chem. Eng. 36 (2019) 657–668. https://doi.org/10.1590/0104-6632.20190362s20180572.

[2] M.B.P.O. Silva, D. Abdal, J.P.Z. Prado, G.S. Dias, S.A.V. Morales, M.C.A. Xavier, A.F. de Almeida, E.S. da Silva, A.E. Maiorano, R.F. Perna, Brazilian J. Food Technol. 24 (2021) 1–11. https://doi.org/10.1590/1981-6723.28320.

[3] R.L. Garcia, G.S. Dias, S.A.V. Morales, M.C.A. Xavier, E.S. Silva, A.E. Maiorano, P.W. Tardioli, R.F. Perna, Brazilian J. Chem. Eng. 38 (2021) 273–285. https://doi.org/10.1007/s43153-021-00110-9.

[4] C. Nobre, E.G.A. Filho, F.A.N. Fernandes, E.S. Brito, S. Rodrigues, J.A. Teixeira, L.R. Rodrigues, Lwt. 89 (2018) 58–64. https://doi.org/10.1016/j.lwt.2017.10.015.

[5] G.S. Dias, E.D. Santos, M.C.A. Xavier, A.F. Almeida, E.S. Silva, A.E. Maiorano, R.F. Perna, S.A.V. Morales, J. Chem. Technol. Biotechnol. (2022). https://doi.org/10.1002/jctb.7163.

[6] A.S.G. Lorenzoni, L.F. Aydos, M.P. Klein, M.A.Z. Ayub, R.C. Rodrigues, P.F. Hertz, J. Mol. Catal. B Enzym. 111 (2015) 51–55. https://doi.org/10.1016/j.molcatb.2014.11.002.

[7] P. Zambelli, L. Tamborini, S. Cazzamalli, A. Pinto, S. Arioli, S. Balzaretti, F.J. Plou, L. Fernandez-Arrojo, F. Molinari, P. Conti, D. Romano, Food Chem. 190 (2016) 607–613. https://doi.org/10.1016/j.foodchem.2015.06.002.

[8] K.H. Jung, S.H. Bang, T.K. Oh, H.J. Park, Biotechnol. Lett. 33 (2011) 1621–1624. https://doi.org/10.1007/s10529-011-0606-8.

[9] E. Aguiar-Oliveira, F. Maugeri, Brazilian J. Chem. Eng. 28 (2011) 363–372. https://doi.org/10.1590/S0104-66322011000300002.

[10] L.L. Faria, S.A.V. Morales, J.P.Z. Prado, G.S. Dias, A.F. de Almeida, M.C.A. Xavier, E.S. da Silva, A.E. Maiorano, R.F. Perna, Biotechnol. Lett. 43 (2021) 43–59. https://doi.org/10.1007/s10529-020-03016-7.

[11] L.A. Garcia, J.P.Z. Prado, S.A.V. Morales, M.C.A. Xavier, M.S. Lopes, E.S. da Silva, A.E. Maiorano, R.F.K. Gunnewiek, R.F. Perna, Mater. Today Commun. 31 (2022). https://doi.org/10.1016/j.mtcomm.2022.103588.

[12] L. Canilha, W. De Carvalho, Biotecnol. Ciência e Desenvolv. Ano IX. (2006) 48–57.

[13] C.C. Castro, C. Nobre, M.E. Duprez, G. De Weireld, A.L. Hantson, Biochem. Eng. J. 118 (2017) 82–90. https://doi.org/10.1016/j.bej.2016.11.011.

[14] R.C. Fernandez, C.A. Ottoni, E.S. Da Silva, R.M.S. Matsubara, J.M. Carter, L.R. Magossi, M.A.A. Wada, M.F. De Andrade Rodrigues, B.G. Maresma, A.E. Maiorano, Appl. Microbiol. Biotechnol. 75 (2007) 87–93. https://doi.org/10.1007/s00253-006-0803-x.

[15] M.C.P. Gonçalves, S.A.V. Morales, E.S. Silva, A.E. Maiorano, R.F. Perna, T.G. Kieckbusch, J. Chem. Technol. Biotechnol. 95 (2020) 2473–2482. https://doi.org/10.1002/jctb.6429.

[16] C.A. Ottoni, R. Cuervo-Fernández, R.M. Piccoli, R. Moreira, B. Guilarte-Maresma, E.S. Da Silva, M.F.A. Rodrigues, A.E. Maiorano, Brazilian J. Chem. Eng. 29 (2012) 49–59. https://doi.org/10.1590/S0104-66322012000100006.

[17] M.A. Ganaie, H.K. Rawat, O.A. Wani, U.S. Gupta, N. Kango, Process Biochem. 49 (2014) 840–844. https://doi.org/10.1016/j.procbio.2014.01.026.

[18] A.A. Homaei, R. Sahiri, F. Vianello, R. Stevanato, J. Chem. Biol. 6 (2013) 185–205. https://doi.org/10.1007/s12154-013-0102-9.

[19] E.L. Cussler, Diffusion mass transfer in fluid systems, Cambridge University Press, New York (2009), p. 655. ISBN: 9780521871211.

[20] H.S. Fogler, Elements of Chemical Reaction Engineering, Prentice Hall, (2019), p. 993. ISBN: 9780133887518.

[21] C.J. Geankopolis, Transport Process and Unit Operations, Prentice-Hall International, New Jersey (1993), p. 937. ISBN: 0-13-045253-X.

[22] M. Starzak, S.D. Peacock, Zuckerindustrie. 122 (1997) 380–387. ISSN 03448657. https://www.researchgate.net/publication/286862720.

[23] M. Mathlouthi, P. Reiser, Sucrose: Properties and Applications, Chapman & Hall, (1995), p. 307. ISBN: 9781461361503.

[24] I.M. Araújo, P.C. Becalette, E.S. da Silva, G.S. Dias, M.C.A. Xavier, A.F. de Almeida, A.E. Maiorano, S.A.V. Morales, R.F. Perna, J. Chem. Technol. Biotechnol. (2022). https://doi.org/10.1002/jctb.7255.

[25] J. Nielsen, Adv. Biochem. Eng. Biotechnol. 46 (1992) 187–223. https://doi.org/10.1007/bfb0000711.

[26] V.G. Elizei, S.M. Chalfoun, D.M. dos S. Botelho, P.P.R. Rebelles, Arq. Inst. Biol., Sao Paulo 81 (2014) 165–172. https://doi.org/10.1590/1808-1657001032012.

[27] I.A. Soares, A.C. Flores, L. Zanettin, H.K. Pin, M.M. Mendonça, R.P. Barcelos, L.R. Trevisol, R.D. Carvalho, D. Schauren, C.L. de M.S.C. da Rocha, S. Baroni, Cienc. e Tecnol. Aliment. 30 (2010) 700–705. https://doi.org/10.1590/S0101-20612010000300021.

[28] K. Long, H.M. Ghazali, A. Ariff, K. Ampon, C. Bucke, Biotechnol. Lett. 18 (1996) 1169–1174. https://doi.org/10.1007/bf01398317.

[29] T. Sun, W. Du, D. Liu, L. Dai, Process Biochem. 45 (2010) 1192–1195. https://doi.org/10.1016/j.procbio.2010.03.037.

[30] O. Barbosa, R. Torres, C. Ortiz, R. Fernandez-Lafuente, Process Biochem. 47 (2012) 1220–1227. https://doi.org/10.1016/j.procbio.2012.04.019.

[31] J.M. Guisan, Immobilization of Enzymes and Cells, Humana Press, New York (2013), p. 375. ISBN: 978-1-62703-550-7.

[32] A.E. Maiorano, E.S. da Silva, R.F. Perna, C.A. Ottoni, R.A.M. Piccoli, R.C. Fernandez, B.G. Maresma, M.F.A. Rodrigues, Biotechnol. Lett. 42 (2020) 2619–2629. https://doi.org/10.1007/s10529-020-03006-9.

[33] J.S. Lim, J.H. Lee, J.M. Kim, S.W. Park, S.W. Kim, Biotechnol. Bioprocess Eng. 11 (2006) 100–104. https://doi.org/10.1007/BF02931891.

[34] J. Su, S. Jia, X. Chen, H. Yu, J. Appl. Phycol. 20 (2008) 213–217. https://doi.org/10.1007/s10811-007-9221-4.

[35] I. Mahasiswa, E. Indonesia, U.G. Mada, World J. Chem. 4 (2009) 34–38.

[36] Y. Bakri, A. Mekaeel, A. Koreih, Brazilian Arch. Biol. Technol. 54 (2011) 659–664. https://doi.org/10.1590/s1516-89132011000400003.

[37] I.L. Furlani, B.S. Amaral, R. V. Oliveira, Q.B. Cassa, Quim. Nova. 43 (2020) 463–473. https://doi.org/10.21577/0100-4042.20170525.

[38] P.A. Fields, Comp. Biochem. Physiol. - A Mol. Integr. Physiol. 129 (2001) 417–431. https://doi.org/10.1016/S1095-6433(00)00359-7.

[39] V.M. Almeida, S.R. Marana, PLoS One. 14 (2019) 1–8. https://doi.org/10.1371/journal.pone.0212977.

[40] E. Gomes, M.A.U. Guez, N. Martin, R. da Silva, Quim. Nova. 30 (2007) 136–145. https://doi.org/10.1590/S0100-40422007000100025.

[41] D. de Andrades, N.G. Graebin, M.K. Kadowaki, M.A.Z. Ayub, R. Fernandez-Lafuente, R.C. Rodrigues, Int. J. Biol. Macromol. 129 (2019) 672–678.https://doi.org/10.1016/j.ijbiomac.2019.02.057.

[42] M. Antošová, M. Polakovič, Chem. Pap. 55 (2001) 350–358. https://www.chempap.org/file_access.php?file=556a350.pdf.

[43] P. Monsan, J. Mol. Catal. 3 (1978) 371–384. https://doi.org/10.1016/0304-5102(78)80026-1.

[44] R. Satar, M.A. Jafri, M. Rasool, S.A. Ansari, Brazilian Arch. Biol. Technol. 60 (2017) 1–12. https://doi.org/10.1590/1678-4324-2017160311.

[45] H. Veny, M.K. Aroua, N.M.N. Sulaiman, Chem. Eng. J. 237 (2014) 123–130. https://doi.org/10.1016/j.cej.2013.10.010.

[46] W. Sieng, A. Yuniarto, J. Environ. Chem. Eng. 7 (2019) 103185. https://doi.org/10.1016/j.jece.2019.103185.

BEATRIZ MENOSSI RIBEIRO[1]
LEANDRO DA RIN DE SANDRE JUNIOR[1]
GIANCARLO DE SOUZA DIAS[1]
MICHELLE DA CUNHA ABREU XAVIER[2]
ALEX FERNANDO DE ALMEIDA[3]
ELDA SABINO DA SILVA[4]
ALFREDO EDUARDO MAIORANO[4]
RAFAEL FIRMANI PERNA[1]
SERGIO ANDRES VILLALBA MORALES[2]

[1]Institute of Science and Technology, Federal University of Alfenas, Poços de Caldas-MG, Brazil

[2]Bioprocess Engineering and Biotechnology Department, Federal University of Tocantins Gurupi-TO, Brazil

[3]Food Engineering Department, Federal University of Tocantins, Palmas-TO, Brazil

[4]Industrial Biotechnology Laboratory, Institute for Technological Research University City, São Paulo-SP, Brazil

NAUČNI RAD

REAKCIJA TRANSFRUKTOZILIZACIJE U KONTINUALNOM REAKTORU

Fruktooligosaharidi su oligomeri fruktoze koji su korisni za ljudsko zdravlje i ishranu kao prebiotski šećeri. Oni se proizvode reakcijom transfruktozilacije u molekulima saharoze katalizovanom enzimima fruktoziltransferaze (FTase, E.C.2.4.1.9) prilepljenim na mikrobne ćelije. Cilj ovog rada je proučavanje pripreme, enzimske aktivnosti i stabilnosti glutaraldehidom umreženih ćelija Aspergillus orizae IPT-301 koje se koriste kao biokatalizator za reakciju ima biokatalizator pripremljen umrežavanjem na 200 o/min za 45 min. Najveća aktivnost transfruktozilacije u reaktoru sa pakovanim slojem dobijen je na 50 °C, sa protokom 3–5 ml/min i sa koncentracijama saharoze od 473–500 g/l. Enzimska kinetika je opisana Michaelis-Mentenovim modelom. Konačno, biokatalizator je pokazao konstantnu aktivnost transfruktozilacije približno 75–300 U/g tokom 12 h reakcije u reaktoru sa pakovanim slojem koji radi u kontinuiranom i diskontinuiranom režimu, redom. Ovi rezultati pokazuju visok potencijal glutaraldehidom umreženih ćelija A. orizae IPT-301 kao heterogenih biokatalizatora za kontinualnu proizvodnju fruktooligosaharida u reaktorima sa pakovanim slojem.

Ključne reči: fruktoziltransferaza, cele ćelije, heterogeni biokatalizatori, reaktori sa pakovanim slojem, fruktooligosaharidi.

Ključne reči: fruktoziltransferaze, umrežene ćelije, heterogeni biokatalizator, reaktorimi sa pakovanim slojem, fruktooligosaharidi.

CI&CEQ
Chemical Industry & Chemical Engineering Quarterly

Available online at
Association of the Chemical Engineers of Serbia *AChE*
www.ache.org.rs/CICEQ

Chem. Ind. Chem. Eng. Q. 30 (2) 111–122 (2024) CI&CEQ

VANESSA DAL-BÓ[1]
HEITOR OTACÍLIO NOGUEIRA ALTINO[1,2]
JOSÉ TEIXEIRA FREIRE[1]

SYSTEM DEVELOPMENT FOR MONITORING THE PRODUCTION PROCESS OF FREEZE-DRIED SAMPLES: A SIMPLE AND LOW-COST APPROACH

Article Highlights

- Accurate and precise data on the freeze-drying process were obtained using low-cost sensors
- The use of correction blank curves significantly reduced the sample's mass measurement errors
- It was identified that the PI controller is suitable for the production process of lyophilized samples
- The system developed could also be used to acquire data on the freezing process

[1]Federal University of São Carlos, Department of Chemical Engineering, Drying Center of Pastes, Suspensions and Seeds, São Carlos, São Paulo, Brazil

[2]Federal University of Uberlandia, Faculty of Chemical Engineering, Uberlândia, MG, Brazil

Abstract

The data acquisition from the freeze-drying process is important for obtaining freeze-dried samples with the desired final moisture content under various operating conditions. The current study extensively presents a simple and low-cost methodology for implementing a data acquisition system in a laboratory-scale freeze dryer. The results showed that higher drying temperatures (40 °C) increased the errors involved in measuring the mass of material; nevertheless, the application of correction blank curves statistically significantly reduced those errors. In general, the system developed provided precise and accurate measurements of the temporal changes in the sample mass and temperature, and chamber pressure variations, allowing monitoring of the production process of freeze-dried samples with low final moisture contents.

Keywords: lyophilization, drying, freezing, heating temperature, Arduino, avocado.

SCIENTIFIC PAPER

UDC 66.047:664.8.037:58

Freeze-drying is a dehydration process whereby the amount of water in a material is reduced by freezing the liquid fraction, followed by sublimation of the ice. Low temperatures reduce the possibility of food degradation, so lyophilized products have better nutritional quality and sensory characteristics [1,2].

Correspondence: H.O.N. Altino, Federal University of São Carlos, Department of Chemical Engineering, Drying Center of Pastes, Suspensions and Seeds, Rod. Washington Luiz, km 235, P.O. Box 676, 13565-905, São Carlos, São Paulo, Brazil.
E-mail: heitor.engquimica@gmail.com
Paper received: 21 August, 2022
Paper revised: 20 December, 2022
Paper accepted: 22 June, 2023

https://doi.org/10.2298/CICEQ220821016D

However, the wider application of the technique is limited by slow drying rates and high operating costs in terms of the energy required for freezing and vacuum. Consequently, freeze-drying is restricted to products with higher added value [3–5]. To reduce the drying time, heat can be supplied to the sample; nevertheless, the heat flux must not be excessive; otherwise, the material can be harmed [6–8].

To study the effect of operational conditions on the final product quality, samples of the material are freeze-dried under different conditions in small-size pilot plants or even lab-scale freeze-dryers [9–11]. The final moisture content of the freeze-dried material is an important parameter that affects product quality and energy consumption. Thus, it is important to monitor the

sublimation rate of the material during the freeze-drying process [10]. To measure this data, many technics have been utilized, such as discontinuous measurement of the sample moisture [12], determination of freeze-drying rate by artificial neural networks [13], thermal flux sensors [14], Tunable Diode Laser Absorption Spectroscopy (TDLAS) [15], Manometric Temperature Measurement (MTM) [16] and Pressure Rise Analysis (PRA) [17], and real-time measurement of sample weight throughout the drying process [10]. In general, most of the experimental data shown in the literature were measured by this first method, which is not advantageous, once the number of experimental points is limited, and the interruptions of the process may lead to long operational times [9,10,18–21]. On the other hand, this last method is reported by some authors as accurate and reliable [13,22]. In addition, it is possible to simultaneously determine the mass and temperature of the sample, which is useful for identifying the transition from the primary to the secondary drying stage [23].

However, commercial freeze dryers with integrated real-time data acquisition systems are rare and often expensive, which leads to the need to adapt conventional freeze dryers. In this context, a few studies in the literature show the adaptation process for research purposes, final moisture control, and sample production. Pikal, Shah, Senior, and Lang [24] described the direct experimental determination of the resistance of the lyophilized product using a suspended microbalance. The system was successfully applied to monitor the drying process of several aqueous solutions. Carullo and Vallan [9] and Vallan [23] describe a system for monitoring the mass and temperature of samples during the lyophilization process. In this system, heat was provided to the sample by conduction. To reduce the mass measurement errors induced by the heat supply, a mechanical lifting system had to be used to raise and release the vials when the mass measurement had to be carried out. Although this system showed good results, the lifting process may affect the lyophilization speed and increase the complexity and costs of the system. In the same way, Roth, Winter, and Lee [25] also used a mobile microbalance. However, in this method, the heat supply was interrupted during the mass measurements. Tribuzi and Laurindo [10] showed a freeze-dryer data acquisition system where a mechanical lifting apparatus was not required, and heat was also provided to the sample by conduction. The authors explored the stability of the mass measurements in blank experiments and the drying rate and temperature data of the freeze-drying process of banana slices. Nevertheless, for simplicity of the mass measurement system, the supply of heat by thermal radiation is preferable once scales with floating sample holders can be employed [23]. Kirmaci *et al.* [11] and Menlik *et al.* [13] showed only some details of the data acquisition systems utilized in the freeze-drying process of apples and strawberries, with heat supply by thermal radiation, but the methodology of adaptation of the freeze-dryers was not reported. Xiang *et al.* [26] constructed a custom microbalance to better control and measure sample temperature and chamber pressure. They observed that the microbalance was useful for studying the sublimation rate during lyophilization. Fissore *et al.* [27] and Pisano [21] provided reviews of the different approaches to using microbalances to study the lyophilization process. They concluded that the system could be useful, mainly to determine the mass transfer resistance of the sample.

In general, most of the systems cited use high-cost sensors, and several important details were not reported in the papers, such as the main physical structure adaptations necessary, electrical/electronic diagrams, and signal noise reduction procedures. It is highlighted by Fissore *et al.* [27] that depending on the operational conditions, process fluctuations, vibrations, gas flows, and temperature gradients can affect the measurement performance of different sensors. In addition, most of those papers did not analyze the main performance indicators of measurement systems, such as accuracy, precision, and stability. In this context, the need for detailed methodologies to correctly develop a system for monitoring the production process of freeze-drying samples is observed, mainly when the heat is supplied to the sample holder by thermal radiation. It is important to highlight that, from a practical point of view; the incorrect measurement of the drying kinetics data can lead to a misleading estimation of the drying time required for obtaining the desired final moisture content of the freeze-dried product. Thus, a detailed methodology for developing a system for accurate data acquisition of the chamber pressure and temperature and sample mass and temperature variation through the freeze-drying process stands out. In particular, the high accuracy of the sample's mass measurement is an important factor since, for some materials, the variation throughout the drying process is very small.

Thus, this work aimed to describe in detail the adaptation process of a laboratory-scale freeze dryer by introducing a data acquisition system for monitoring the material's mass and temperature, and chamber pressure, during the production process of freeze-dried samples. The acquired data were used to control the final moisture content of the produced sample. The system was built using low-cost sensors, actuators, and microprocessors, developing a more accessible and

reproducible methodology. The performance indicators of the mass measurements in blank experiments were determined for different operational conditions. As a test case, the system's performance was also evaluated in drying avocado (*Persea americana*) pulp, with tray heating temperature at 40 °C and without temperature control. The results were used to determine energy indexes and transition points during the drying process. The system's reliability was analyzed by comparing the mass of material determined by the data acquisition system, before and after the drying process, with the data provided by an external analytical scale.

MATERIALS AND METHODS

System development for freeze-drying data acquisition

The studies were performed using a laboratory-scale freeze dryer (Labconco®, FreeZone, console 6L), as shown in Figure 1. The basic components of the system were: data acquisition system (1), drying chamber (4), vapor condensation chamber (5), control panel (6), and freeze dryer internal components (7).

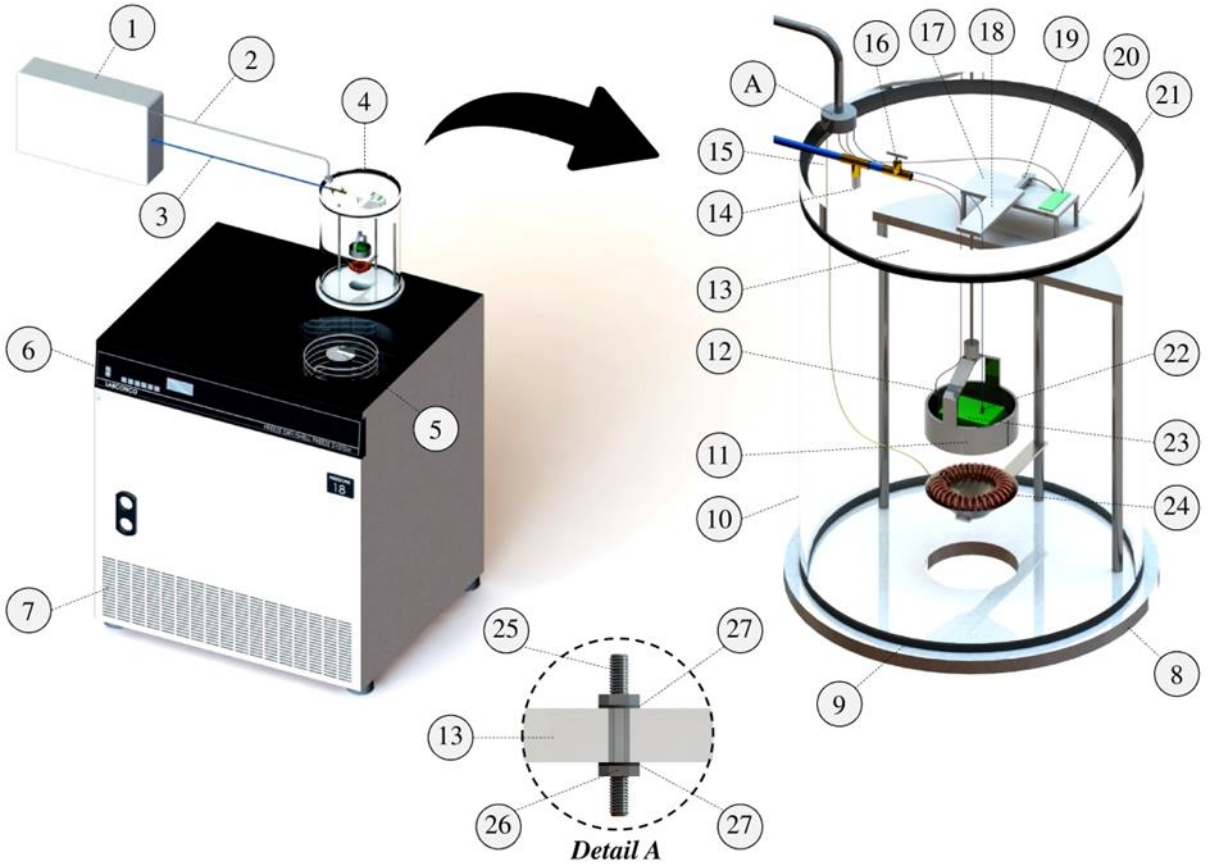

Captions

1 – Data acquisition system:
  a – Microprocessor (Arduino®, Mega, 2560R3)
  b – Pressure transducer (Freescale®, MPX5500DP)
  c – Pressure, temperature, and humidity sensor (Bosch®, BME280)
2 – Data transfer cable and electrical commands
3 – Flexible pneumatic hose
4 – Cylindrical acrylic chamber
5 – Vapor condensation chamber
  a – Temperature sensor (Maxim Integrated®, DS18B20)
6 – Freeze dryer control panel
7 – Freeze dryer internal components:
  a – Vacuum pump (JB Industries®, DV 142N 250)
  b – Radiator Heat Exchanger
8 – Steel support of the cylindrical chamber
9 – Rubber seal of the cylindrical acrylic chamber
10 – Acrylic wall of the cylindrical chamber
11 – Aluminum sample holder tray
12 – Temperature sensor (Maxim Integrated®, DS18B20)
13 – Acrylic chamber cover
14 – Pressure tap point
15 – Temperature sensor (Maxim Integrated®, DS18B20)
16 – Acrylic support of load cell
17 – Pressure relief valve
18 – Acrylic extension of load cell
19 – Load cell (Zhipu®)
20 – Voltage amplifier (HX711, 24 Bits)
21 – Helical springs
22 – Temperature sensor (Maxim Integrated®, DS18B20)
23 – Avocado sample
24 – Stainless steel resistor (25W)
25 – Steel screw
26 – Steel screw nut
27 – Rubber o-ring

Figure 1. Experimental system for data acquisition of the freeze-drying processes.

The vacuum pump (7a) specification was 5 CFM, two stages, a final vacuum of 3.2 kPa, and a flow rate of 8.52 m^3/h. The drying environment consisted of a cylindrical acrylic chamber (4). The junction between the cylinder and the cover was hermetically sealed with a rubber ring (9). To standardize the experiments and reduce random errors, such as ambient heat transfer by thermal radiation to the sample, all the assays were performed in a climatized environment (ambient temperature of approximately 22 °C), close to the sunlight, under an artificial light source (fluorescent lamp of 32 W). To obtain data on the freeze-drying process, the drying chamber (4) and drying chamber cover (13) were modified by the attachment of a mass measurement system (11, 17, 18, 19, 20, and 21), a heating system (24), and temperature (5a, 12, 15 and 22) and pressure (14) sensors.

The mass was measured using a load cell (19) with an operating temperature range from -20 to 60 °C, a maximum load of 200 g, and a precision of ±0.04 g. The load cell (18) was attached to the acrylic support (17) by two screws. This support was coupled to another one of larger proportions using four helical springs (21) to minimize the effect of vibrations on load cell measurements. The load cell had an extension (18), attached by two screws, that was positioned centrally in the drying chamber. An aluminum sample holder tray (11) was suspended from the load cell extension (18) by a steel cable. In this way, the load cell was sensitive to changes in the mass of the sample holder tray (11). The low-strength signals produced by the load cell were amplified by a voltage amplifier (20) and transmitted by cables (2) to a microprocessor (1a). The electrical diagram in Figure S1 (Supplementary Material) details the wire connections between these devices. The load cell was calibrated using different weights from 1 g to 200 g. A touch button (Figure S1) was added to the system to tare the balance before each freeze-drying procedure.

The tray was heated from underneath by irradiation from a 25 W resistor (24), powered by a 12 v power source, detailed in Figure S1. The temperature of the tray was measured using a sensor (12) with a range from -55 °C to 125 °C and a precision of ±0.5 °C. The temperature data of the tray was also transmitted through cables (2) to the microprocessor (1a). These data were used by the microprocessor to act on a solid-state relay (Figure S1) connected to the heating resistor (23) and feedback-control the temperature of the tray using an on-off control. The routine for data reading, control, and writing was developed using Arduino® IDE 1.8.5 software and can be accessed in section S.1 (Supplementary Material). The distance between the resistor and the tray was 50 mm. The temperatures of the sample (22), the chamber ambient (15), and the condenser surface (5a) were measured by sensors of the same model and also transmitted to the microprocessor. Note that flexible cables were used for the electrical wiring of the temperature sensors (12 and 22) placed on the sample holder tray (11), which were attached to the load cell extension. This configuration was adopted to reduce the influence of the movement of the cables on load cell measurements. The temperature sensors were calibrated using a calibrator block (Tchne®, Model DB-35L) in the temperature range employed in the experiments.

A t-connector was attached to the drying chamber cover (13) so that the pressure (14) inside the chamber could be accessed. Thus, one outlet of the t-connector leads to a needle valve (16) for removing the vacuum. The other outlet was connected (3) (using a ¼" poly-flux hose) to a pressure sensor (1b), with an operating range from 0 kPa to 500 kPa and an accuracy of 2.5%, for measuring the internal pressure of the vessel. The pressure data was also transmitted to the microprocessor. Figure S1 details the wiring connections between these devices. The pressure sensor was calibrated with an air vacuum/pump station (Cole-Parmer®, Model 470-5942).

A pressure, temperature, and humidity sensor (1c) with the accuracies of ±3% (humidity), ±0.5 °C (temperature), and ±0.1 kPa (pressure) was used to monitor the environmental conditions outside the chamber during the freeze-drying processes.

The wire connections of the load cell, temperature sensors, and electrical resistance were made with stainless steel screws (25) through the acrylic chamber cover (13), sealed with o-rings (27), as shown in Detail A of Figure 1. This type of connection was necessary to prevent vacuum leakage. The sensor data were acquired by the microprocessor (1a) and were transmitted to a computer (Intel® Core™ i7-930 processor, 4 GB RAM) through a USB cable (baud rate of 9600). The data were recorded in real-time, using a Microsoft® Excel spreadsheet. The communication between the microcontroller and the Excel software was performed using the PLX-DAQ add-in (Parallax Inc.).

It's important to highlight that the system developed in this study proposes the use of a microcontroller based on the Arduino® platform due to its low cost, high processing velocity (16 MHz), and relatively good analog input channel resolution (10 Bits), when compared to other commercial products available or proposed by previous works [11,25,28]. Arduino® is open-source hardware with easy installation, control, and operation that does not require

extensive technical support [29–32]. In addition, all sensors used are easily accessible and of low cost, which facilitates the use of the methodology described in this work.

Evaluation of the online mass measurement system

To verify the reliability of the obtaining methodology of mass measurements in the drying chamber, over 80,000 blank data were acquired before and after the freeze-drying procedures for 20 h. The tests were performed in duplicate, without adding a test specimen (avocado), with a heating temperature of 40 °C and without temperature control, to observe the effect of temperature on the stability of the measurements. The vacuum pressure and the condenser temperature were approximately 0.2 kPa and -50 °C, respectively.

The data were analyzed using the main performance indicators of measurements, such as precision and accuracy. Precision represents the random system errors and quantifies how well a measurement can be carried out without a real reference value [33,34]. In the present paper, precision was estimated by the standard deviation (*SD*) between the data obtained by the load cell (y_i) and the average between the same ($\bar{y}$):

$$SD = \sqrt{\frac{1}{N}\sum_{i=1}^{N}(y_i - \bar{y})^2} \quad (1)$$

Accuracy represents systematic errors and may be defined as the compliance degree of an average quantity related to its actual value [33,34]. Accuracy was estimated through the mean absolute deviation (*MAD*) between data obtained by the sensor (y_i) and the reference values (y_f), according to Eq. (2). In this case, the tare value before the vacuum and temperature control activation was used as a reference.

$$MAD = \frac{1}{N}\sum_{i=1}^{N}(y_i - y_f) \quad (2)$$

Experimental procedure for the dehydration process

Sample preparation

Avocados (*Persea americana*) from a local market in São Carlos (São Paulo State, Brazil) were used. The selection and cleaning process of the fruit was carried out as described by Dal-Bó and Freire [8]. The pulp was cut with a manual slicer, producing pieces with sizes of 25 x 25 x 15 mm (width x length x height). The samples were frozen on a PVC film on a tray in the lyophilizer condenser for 24 h at -30 °C. Each test employed a new fruit from the same batch that had been stored in an air-conditioned room for a maximum of three days. All the tests were performed in duplicate.

Moisture content

The moisture content of the fruit pulp was determined before and after the freeze-drying process, according to AOAC method 934.06 [35], by drying in a vacuum oven (Model TE-395, Tecnal®). The procedure was performed (in triplicate) for 24 h, at 70 °C, under reduced pressure of approximately 8 kPa.

The mass of each sample was measured using an analytical balance with a precision of 0.0001 g (A&D®, FR-200 MKII) before and after treatment in the vacuum oven. The moisture contents, based on wet and dry mass, were calculated using Eqs. (3) and (4), respectively:

$$X_{wb} = \frac{m_w}{m_o} \quad (3)$$

$$X_{db} = \frac{m_w}{m_f} \quad (4)$$

where X_{wb} is the moisture content on a wet basis [$kg_{water}/kg_{wet\ material}$]; X_{db} is the moisture content on a dry basis [$kg_{water}/kg_{dry\ solid}$]; m_0 and m_f are the masses [kg] of the sample before and after drying for 24 h in the oven, respectively; and m_w is the mass of water [kg] in the sample, determined as the difference between the initial and final masses of the sample.

Dehydration of the avocado pulp by freeze-drying

A slice of frozen avocado pulp was transferred using a clamp to the central region of the tray connected to the load cell, the system was closed, and the vacuum pump was activated. After starting the pump, the mean absolute operating pressure was 0.22±0.01 kPa, and the condensing surface temperature was -50.15±0.54 °C. It is important to highlight that these conditions are lower than those of triple point of water at 0.01°C and 0.611 kPa [36], which is generally required to perform the sublimation process [37,38]

The effect of heating temperature on the load cell measurements and the drying kinetics was investigated. For this, freeze-drying of the avocado pulp was performed using the sample tray with a heating temperature of 40 °C and without temperature control. The change in moisture content was monitored by recording the sample mass value every 3 s until constant mass. The reliability of the mass measurement system was evaluated under the conditions mentioned above by comparing the mass of the sample obtained by the developed system with that provided by an analytical balance (A&D®, Model FR-200 MKII) before and after the freezing-drying process.

Energy Aspect

To determine the effectiveness of the lyophilization system, with and without temperature

control, the values of specific moisture extraction rate (*SMER*), specific energy consumption (*SEC*), and moisture extraction rate (*MER*) were calculated by Eqs. (5), (6), and (7), respectively [39,40]:

$$SMER = \frac{m_w}{E_t} \quad (5)$$

$$SEC = \frac{1}{SMER} \quad (6)$$

$$MER = \frac{m_w}{t_d} \quad (7)$$

where m_w is the amount of water removed during drying, [kg water], E_t is the total energy supplied in the drying process, and [kJ]; e t_d is the drying time, [h].

The amount of energy required by the lyophilization process (primary and secondary drying stages) was calculated according to Huang *et al.* [41] and Dincer and Rosen [42] and includes six parts: the energy required for sublimation and water desorption, the energy required to raise the temperature of the material, condense the steam, evacuate the system, and provide heat by conduction (through the resistor) to heat the tray.

The values used for the energy calculations were based on the data provided by the equipment manual and on experimental data obtained for each studied condition. Enthalpy was determined from the thermodynamic tables [43]. It is important to highlight that although energy parameters analyzed for such a small system are hardly representative of an industrial process, they are useful o compare the effect of operational conditions on the energy saving of the freeze-drying process.

Data treatment and analysis

The moisture content (dry basis) and temperature data were used to obtain drying and temperature curves, as a function of freeze-drying time. The data were acquired every 3 s, but the graphs were plotted using intervals of 240 s to facilitate data visualization.

The dimensionless moisture contents were calculated as follows:

$$MR = \frac{X_t - X_{eq}}{X_0 - X_{eq}} \quad (8)$$

where X_t is the moisture content (dry basis) at a given instant [$kg_{water}/kg_{dry\ solid}$], and X_0 and X_{eq} are the moisture contents (dry basis) at the start of the process and dynamic equilibrium, respectively [$kg_{water}/kg_{dry\ solid}$].

Comparing the values of X_t or X_0 with the equilibrium moisture content, X_{eq} was relatively small (approximately zero), so the dimensionless moisture content could be simplified to Eq.(9), as described by Midilli *et al.* [44]:

$$MR = \frac{X_t}{X_0} \quad (9)$$

RESULTS AND DISCUSSION

Evaluation of the online mass measurement system

Figure 2 shows the mass data as a function of time for the blank tests under both analyzed conditions. When the system was evacuated, the drying chamber pressure reached equilibrium about 1 min after activating the pump, as displayed in Figure 3. The inset graph of Figure 2 shows that in both conditions studied, the mass recorded increased to 0.2 g after vacuum equilibrium was attained, followed by a slight decrease. This change was caused by the airflow during the evacuation, as described by Tribuzi and Laurindo [10]. Nevertheless, the mass measurement increased again after this event and reached a plateau-like state. In the test without tray heating temperature control, the mass measurement increased and stabilized in values close to 0.2 g, while for the test with heating temperature control, the stabilization was observed in values similar to 0.35 g. The difference between the curves obtained with and without temperature control can be attributed to the influence of temperature on the load cell. Temperature affects the load cell output by altering the sensitivity of the load cell [45]. Note that in the process without tray heating temperature control, the masses obtained for the duplicates presented greater oscillations because the ambient temperature influenced them due to radiation heat transfer (even though the tests were performed in an air-conditioned room, closed to the sunlight, under artificial light source).

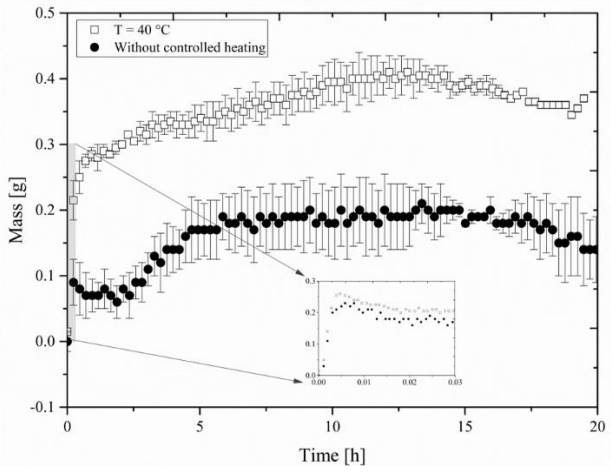

Figure 2. Mass, as a function of time, is in the blank test to evaluate the data acquisition system.

Using the data shown in Figure 2, the overall precision and accuracy of the mass measurement system could be determined as 0.107 g and 0.240 g, respectively. Considering that 8.8 g of fruit was used, on average, and the weight variation due to the drying process was approximately 7.4 g, the error introduced by the system's accuracy represents only 3.2% of the mass variation. Thus, the system developed can be considered precise and accurate for determining the sample mass variation induced by drying. Nevertheless, Figure 2 shows that the data obtained were not randomly distributed around zero, and the deviations observed were reproducible (low confidence intervals). Thus, blank curves were obtained (in duplicate) for the different operating conditions before and after each sample dehydration test to increase the system's accuracy and correct the avocado pulp mass values obtained during the freeze-drying process. The results of using blank curves to correct the mass of the material will be shown in the next section.

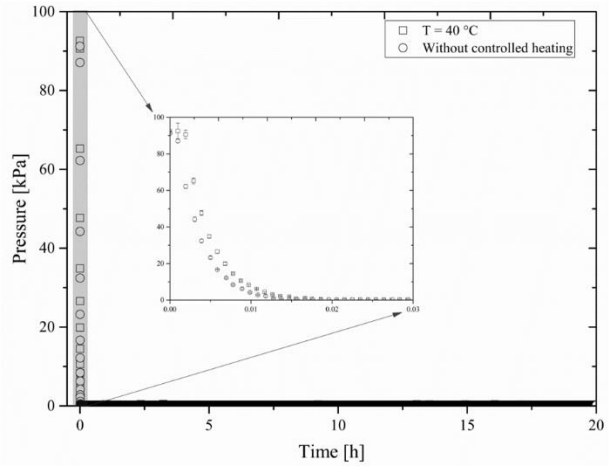

Figure 3. Pressure in the freeze-drying system as a function of drying time.

The deviations from the reference value (zero) and oscillations observed can be attributed to many factors. Typical load cells use strain gauges that deform when a load is applied to the contact area, consequently increasing the resistance [46–48]. As Hernandez [49] and Muller *et al.* [50] pointed out, temperature, linearity, hysteresis, repeatability, and/or flux density influence the signal obtained using a strain gauge. Noise from the electricity supply network can also affect the ability of a load cell to produce the same value when the same weight is applied [49,51]. It is because the response given by the amplifier module is a voltage difference, depending on the amplifier gain. In addition to these factors, vibrations caused by the vacuum pump and oscillations in the degree of vacuum affect the precision of the mass measurement.

Freeze-drying of the avocado pulp

After the blank assays, the avocado pulp was dried with either an unheated tray or heated at 40 °C. The air temperature, pressure, and relative humidity of the environment outside of the chamber were monitored during the freeze-drying tests, with mean values of 23.71 ± 0.46 °C, 91.99 ± 0.10 kPa, and 37.18 ± 2.35%, respectively. Figure 4 shows the results of the avocado pulp mass as a function of drying time.

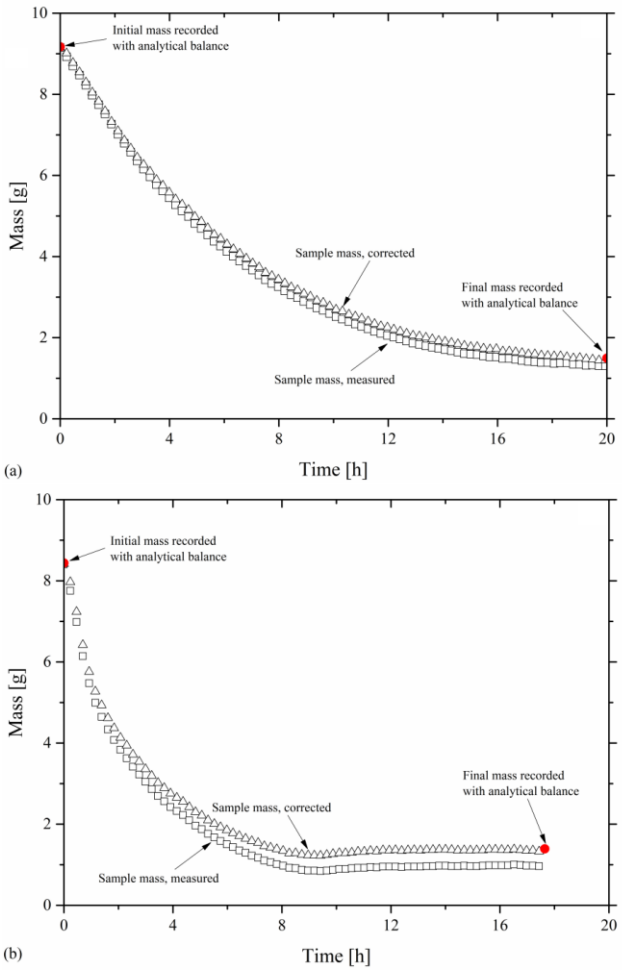

Figure 4. Sample mass as a function of drying time. Drying conditions: (a) without temperature control of the heating tray; and (b) heating plate temperature at 40 °C.

As shown in Figure 4b, the heating temperature greatly influenced the mass obtained with the load cell and registered with the microcontroller in Arduino®. Note that the difference between curves is greater in the final drying period, which is justified due to the lower mass of the sample. Greater masses added may reduce errors during data collection [10].

The avocado pulp's mass value was measured by an analytical balance (accuracy of ± 0.0001 g) before and after the freezing-drying process to check the system's reliability. The values obtained by the analytical balance were marked in Figure 4 with red dots. A Student's t-test was performed between the values measured by the analytical balance and those recorded by the data acquisition system, with and

without the application of correction curves, before and after the freezing-drying process, for both temperature control conditions tested. The results are presented in Table 1 and showed, with 95% of reliability, that there is no statistically significant difference (*p-value* > 0.05) between the data obtained by the analytical balance and by the acquisition system before the freezing-drying process, for both temperature conditions, with or without curves of corrections. Nevertheless, after the freezing-drying process, the results showed that values obtained without the blank curve correction were statistically significantly different from those obtained by the analytical balance for both temperature control conditions. On the other hand, the application of correction curves turned the values obtained by the data acquisition system statistically equal to those obtained by the analytical balance. These results reinforce the need for corrections by blank curves to obtain reliable values of the mass of material during the freezing-drying process.

Table 1. Results of probability value (p-value) of the Student's t- test.

Temperature control	Blank curve correction	Freezing drying process	
		Before	After
No	Yes	0.388	0.089
	No	0.921	0.023
Yes (40 °C)	Yes	0.227	0.134
	No	0.360	0.006

Figure 5 shows the temperature of the sample, with tray heating temperature at 40 °C and without temperature control, as a function of time, together with the corresponding standard deviations. During the freeze-drying process, the mean experimental errors for the temperature curves of the sample and the heating plate were ±1.40 and ±0.21 °C (Figure 5a) and ±2.28 and ± 0.52 °C (Figure 5b), respectively. Greater deviations were observed for the sample temperature due to the variability of the composition of the same fruit. As shown in Figure 5a, the sample temperature remained low (during the sublimation stage), despite the heat supply, due to the high heat of sublimation of the ice. The shift to the desorption step occurred when the ice was sublimated entirely and the sample temperature approached the heating temperature. The start of the transition from sublimation to desorption was observed when the mean sample temperature reached 21 °C (after 8 h). When the heat was not supplied during the freeze-drying process, the temperature of the sample showed a constant increase (Figure 5b). The shift from sublimation to desorption occurred at the end of the process (after around 18 h of freeze-drying), reaching a mean equilibrium temperature of 21 °C. This result shows that the freeze-drying chamber was not completely thermally insulated from the external environment, which hampers the possibility of transferring the drying kinetics results obtained, and constitutes a point of improvement in the system. Nevertheless, as shown below, the proposed methodology allowed for obtaining the materials' highly reproducible drying kinetics curves, meeting the final moisture content control goal.

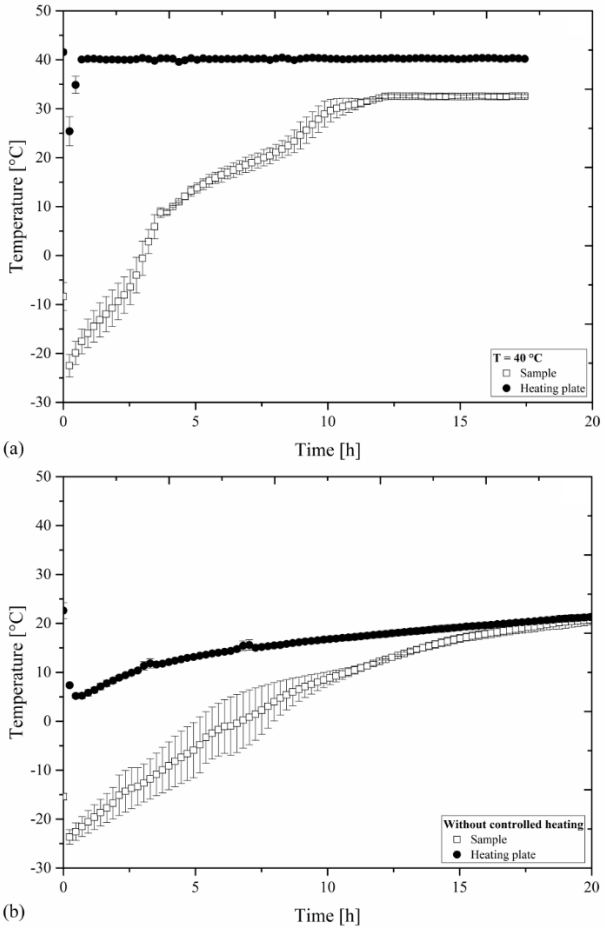

Figure 5. The temperature of the sample, as a function of time, during the freeze-drying process: (a) with heating at 40 °C and (b) without heating temperature control.

The controlled supply of heat during the freeze-drying process is essential for decreasing the drying time, consequently reducing the energy expenditure associated with the application of a vacuum. However, a substantial increase in the plate temperature is not recommended because the region of the sample in direct contact with the plate could overheat, compromising the product's quality and altering its visual appearance. Furthermore, as pointed out by Levi and Karel [52] and Pikal and Shah [53], exceeding certain temperature limits could cause the sample to collapse, with the sealing of capillaries, reduction of the pore size, loss of structure, decreased dehydration, and swelling.

The mean moisture content of *natural* avocado

pulp was 0.86 ± 0.01 $kg_{water}/kg_{wet\ material}$ (6.12 ± 0.51 $kg_{water}/kg_{dry\ solid}$, on a dry basis). Figure 6 shows the results for the dimensionless moisture content (dry basis) as a function of the avocado pulp drying time. The curves presented satisfactory reproducibility, with a mean standard deviation of ± 0.03, which allows for controlling the final moisture content of the freeze-dried sample produced. The application of the proposed system to produce freeze-dried samples can be observed in more detail elsewhere [8]. The authors pointed out good reproducibility and efficiency in temperature control, allowing to study the effect of drying temperature on the drying time and quality of the final product.

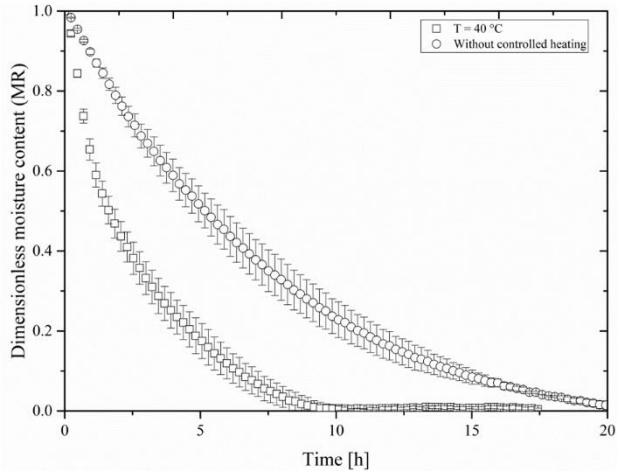

Figure 6. Dimensionless moisture content, as a function of the avocado pulp freeze-drying time, with and without tray heating temperature control.

As expected, the controlled heat supply during the freeze-drying accelerated the dehydration process, decreasing the drying time by about 0.63 times. The freeze-drying process without heating control reached dynamic equilibrium after around 20 h. In previous work, Souza *et al.* [54] found that equilibrium was reached after around 13 h. This difference could have been due to factors related to the freezing of the sample, the operating conditions, the freeze-drying system, and the qualities of the raw materials used.

As shown in Figure 7, higher drying rates were observed when the heat was supplied in a controlled manner during the process. The driving force in freeze-drying is the temperature difference and, therefore, the vapor pressure difference between the sublimation surface of the sample and the ice layer on the condenser. Thus, a greater temperature difference is expected to provide higher drying rates. Besides, with the addition of excess heat, there was the initiation of the induction period, with the temperature of the product increasing, consequently increasing the drying rate. The average duration of these periods was around 21 min and 7 min for the processes with and without the tray heating temperature control, respectively.

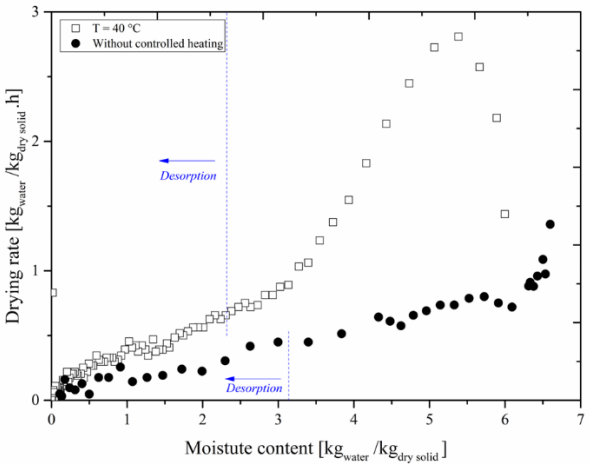

Figure 7. Drying rates as a function of moisture content (dry basis).

After the induction period, there was a period during which the drying rate decreased, which is characteristic of biological materials. During this period, the average drying rates were 1.42 and 0.56 $(kg_{water}/kg_{dry\ solid}).h^{-1}$ for the processes with and without tray heating temperature control, respectively. The material presented greater water loss during the sublimation stage since the water was not bound to the molecular structure of the pulp [55], so the drying rate was faster. Only residual water was removed during the desorption stage, so the drying rate was slower.

Energy Aspect

Table 2 shows the freeze-drying process's drying time and energy indexes, with and without heating temperature control. The specific moisture extraction rate indicates the energy efficiency in drying. The results showed that the process with temperature control had a higher *SMER* index, indicating a greater amount of water removed and, consequently, better thermal efficiency than without temperature control.

A higher value of specific energy consumption for the process without temperature control was also reported by Liu *et al.* [57], and this may be related to the long operational time linked to the low pressure of the drying chamber and the low-temperature state of the cold trap, which result in high energy consumption per kilogram of water removed [1,57,58].

By analyzing the valid energy consumption of the system, it is observed that despite the controlled heat supply, the process with temperature control showed less energy required to operate. It is due to the shorter operational time and the balance between the sublimation and desorption steps. In general, as shown in Table 2, the lyophilization process covered in this study showed better energy indexes when compared to

Table 2. Energy indexes of freeze-drying avocado pulp.

	T = 40 °C	Without temperature control	Black chokeberry puree[1]	Purple basil leaves[2]
Drying time [h]	12.13	19.48	3.00	8.00
Energy consumption [kWh]	0.0398	0.0492	1.36	5.67
SMER [kg/kWh]	0.1943	0.1601	0.016	0.001
SEC [kWh/kg]	5.15	6.24	61.72	709.09
MER [kg/h]	6.37×10^{-4}	4.04×10^{-4}	72.5×10^{-4}	10×10^{-4}

[1][39]; [2][56].

CONCLUSION

This paper showed in extensive detail the adaptation methodology of a laboratory-scale freeze dryer to monitor the production process of freeze-dried samples. The following conclusions can be drawn from this study:

The methodology described permitted the development of a precise and accurate data acquisition system for measuring the temporal changes in the sample mass and temperature and chamber pressure variations, estimating the drying rates, temperature heating behavior, and energy aspects of the production process of freeze-dried samples.

The use of higher temperatures (40 °C) in the freeze-drying process increased the errors involved in measuring the mass of material; nevertheless, the application of correction blank curves statistically significantly reduced those errors.

The controlled heat supply accelerated the freeze-drying process and enabled the evaluation of the effect of temperature on the drying rate. Besides, the temperature control decreased the specific energy consumption of the process.

Overall, the methodology described in this paper can be extended to adapting similar freeze-drying equipment, using low-cost devices, making the equipment more efficient and automated, especially for producing freeze-dried samples for research purposes.

ACKNOWLEDGMENT

The authors are grateful for the financial support provided by CNPq (process 140907/2017-3), CAPES (Finance Code 001), and PPGEQ/UFSCar.

REFERENCES

[1] G. Caliskan, S.N. Dirim, Heat Mass Transfer 53 (2017) 2129–2141. https://doi.org/10.1007/s00231-017-1967-x.

[2] Y. Wang, X. Li, X. Chen, B. Li, X. Mao, J. Miao, C. Zhao, L. Huang, W. Gao, Chem. Eng. Process. 129 (2018) 84–94. https://doi.org/10.1016/j.cep.2018.03.020.

[3] E. Lopez-Quiroga, L.T. Antelo, A.A. Alonso, J. Food Eng. 111 (2012) 655–666. https://doi.org/10.1016/j.jfoodeng.2012.03.001.

[4] L.G. Marques, M.C. Ferreira, J.T. Freire, Chem. Eng. Process. 46 (2007) 451–457. https://doi.org/10.1016/j.cep.2006.04.011.

[5] R.L. Monteiro, B.A.M. Carciofi, A. Marsaioli, J.B. Laurindo, J. Food Eng. 166 (2015) 276–284. https://doi.org/10.1016/j.jfoodeng.2015.06.029.

[6] A.S. Mujumdar, Handbook of Industrial Drying, CRC Press, Boca Raton, (2014), p. 1352. https://doi.org/10.1080/07373938808916399.

[7] X.C. Tang, M.J. Pikal, Pharm. Res. 21 (2004) 191–200. https://doi.org/10.1023/B:PHAM.0000016234.73023.75.

[8] V. Dal-Bó, J.T. Freire, Food Control. 132 (2022) 108526. https://doi.org/10.1016/j.foodcont.2021.108526.

[9] A. Carullo, A. Vallan, Measurement 45 (2012) 1706–1712. https://doi.org/10.1016/j.measurement.2012.04.017.

[10] G. Tribuzi, J.B. Laurindo, Dry. Technol. 32 (2014) 1119–1124. https://doi.org/10.1080/07373937.2014.886258.

[11] V. Kirrmaci, H. Usta, T. Menlik, Dry. Technol. 26 (2008) 1570–1576. https://doi.org/10.1080/07373930802467037.

[12] J.P. George, A.K. Datta, J. Food Eng. 52 (2002) 89–93. https://doi.org/10.1016/S0260-8774(01)00091-7.

[13] T. Menlik, M.B. Özdemir, V. Kirmaci, Expert Syst. Appl. 37 (2010) 7669–7677. https://doi.org/10.1016/j.eswa.2010.04.075.

[14] C. Moino, E. Bourlés, R. Pisano, B. Scutellà, Ind. Eng. Chem. Res. 60 (2021) 9637–9645. https://doi.org/10.1021/acs.iecr.1c00536.

[15] S.C. Schneid, H. Gieseler, W.J. Kessler, S.A. Luthra, M.J. Pikal, AAPS PharmSciTech. 12 (2011) 379–387. https://doi.org/10.1208/s12249-011-9600-7.

[16] X. (Charlie) Tang, S.L. Nail, M.J. Pikal, Pharm. Res. 22 (2005) 685–700. https://doi.org/10.1007/s11095-005-2501-2.

[17] P. Chouvenc, S. Vessot, J. Andrieu, P. Vacus, Dry. Technol. 22 (2004) 1577–1601. https://doi.org/10.1081/DRT-200025605.

[18] R. Daoussi, S. Vessot, J. Andrieu, O. Monnier, Chem. Eng. Res. Des. 87 (2009) 899–907. https://doi.org/10.1016/j.cherd.2008.09.007.

[19] S.A. Velardi, H. Hammouri, A.A. Barresi, Chem. Eng. Res. Des. 87 (2009) 1409–1419. https://doi.org/10.1016/j.cherd.2009.03.011.

[20] C. Vilas, A.A. Alonso, E. Balsa-Canto, E. López-Quiroga, I.C. Trelea, Processes 8 (2020) 1–21. https://doi.org/10.3390/pr8030325.

[21] R. Pisano, Dry. Technol. 40 (2022) 140–157. https://doi.org/10.1080/07373937.2020.1774891.

[22] A.A. Barresi, R. Pisano, D. Fissore, V. Rasetto, S.A. Velardi, A. Vallan, M. Parvis, M. Galan, Chem. Eng.

Process. Process Intensif. 48 (2009) 408–423. https://doi.org/10.1016/j.cep.2008.05.004.

[23] A. Vallan, Instrumentation and Measurement Technology Conference, in Proceeding of IEEE Instrumentation & Measurement Technology Conference, Warsaw, Poland, (2007). p. 1–5. https://doi.org/10.1109/IMTC.2007.379000.

[24] M.J. Pikal, S. Shah, D. Senior, J.E. Lang, J. Pharm. Sci. 72 (1983) 635–650. https://doi.org/10.1002/jps.2600720614.

[25] C. Roth, G. Winter, G. Lee, J. Pharm. Sci. 90 (2001) 1345–1355. https://doi.org/10.1002/jps.1087.

[26] J. Xiang, J.M. Hey, V. Liedtke, D.. Wang, Int. J. Pharm. 279 (2004) 95–105. https://doi.org/10.1016/j.ijpharm.2004.04.011.

[27] D. Fissore, R. Pisano, A.A. Barresi, Dry. Technol. 36 (2018) 1839–1865. https://doi.org/10.1080/07373937.2018.1440590.

[28] G. Rovero, S. Ghio, A.A. Barresi, Chem. Eng. Sci. 56 (2001) 3575–3584. https://doi.org/10.1016/S0009-2509(01)00025-2.

[29] S. Grassini, S. Corbellini, M. Parvis, E. Angelini, F. Zucchi, Meas.: J. Int. Meas. Confed. 114 (2018) 508–514. https://doi.org/10.1016/j.measurement.2016.07.014.

[30] V.D. Sabadoti, A.C. Miano, P.E.D. Augusto, J. Food Process. Preserv. 44 (2020) 1–10. https://doi.org/10.1111/jfpp.14769.

[31] O.I. Obajemihi, J.O. Olaoye, J.H. Cheng, J.O. Ojediran, D.W. Sun, J. Food Process. Preserv. 45 (2021) 1–14. https://doi.org/10.1111/jfpp.15287.

[32] A. D'Ausilio, Behav. Res. Methods 44 (2012) 305–313. https://doi.org/10.3758/s13428-011-0163-z.

[33] A. Kilpela, Pulsed time-of-flight laser range finder techniques for fast, high precision measurement applications, University of Oulu, (2004) p. 98. https://oulurepo.oulu.fi/handle/10024/35963.

[34] X. Li, B. Yang, X. Xie, D. Li, L. Xu, Sensors (Switzerland). 18 (2018) 1–16. https://doi.org/10.3390/s18041156.

[35] AOAC, Official methods of analysis of Association of Official Analytical Chemists, AOAC, Arlington (1990), p. 771. ISBN 0-935584-42-0.

[36] P. Jacobs, Thermodynamics, Imperial College Press, London (2013), p. 456. ISBN 184816971X.

[37] W. Yang, D.E.O. III, R.O.W. III, in Formulating Poorly Water Soluble Drugs, R.O. Williams III, A. B. Watts, D. A. Miller, Springer, New York (2012), p. 646. https://doi.org/10.1007/978-1-4614-1144-4.

[38] A. Bhushani, C. Anandharamakrishnan, in Handbook of Drying for Dairy Products, C. Anandharamakrishnan, John Wiley & Sons, Chichester (2017) p. 316. https://doi.org/10.1002/9781118930526.ch6.

[39] O. Taskin, Heat Mass Transfer 56 (2020) 2503–2513. https://doi.org/10.1007/s00231-020-02867-0.

[40] T. Kovacı, E. Dikmen, A.Ş. Şahin, J. Food Process Eng. 43 (2020) 1–9. https://doi.org/10.1111/jfpe.13528.

[41] L.L. Huang, M. Zhang, A.S. Mujumdar, D.F. Sun, G.W. Tan, S. Tang, Dry. Technol. 27 (2009) 938–946. https://doi.org/10.1080/07373930902901844.

[42] I. Dincer, M.A. Rosen, Energy, Environment and Sustainable Development, Springer, Vienna, (2012) p. 349. https://doi.org/10.1007/978-3-7091-0109-4.

[43] Y.A. Çengel, M.A. Boles, Thermodynamics: an engineering approach, Mc Graw Hill Education, New York, (2014) p. 1024. ISBN 9780073398174.

[44] A. Midilli, H. Kucuk, Z. Yapar, Dry. Technol. 20 (2002) 1503-1513. https://doi.org/10.1081/DRT-120005864.

[45] T. Kopczynski, Five Factors That Can Affect Your Weighing System's Accuracy, Hardy, San Diego, (2011). https://www.hardysolutions.com/images/uploaded/5Factors_WP_0323%20(1).pdf.

[46] C.D. Johnson, Process Control Instrumentation Technology, Pearson Education Limited, Harlow, (2013) p. 684. ISBN 9781292026015.

[47] A.L. Silva, M. Varanis, A.G. Mereles, C. Oliveira, J.M. Balthazar, Rev. Bras. Ensino Fis. 41 (2019). https://doi.org/10.1590/1806-9126-RBEF-2018-0206.

[48] A.R. Gorbushin, A.A. Bolshakova, Measurement 152 (2020) 107381. https://doi.org/10.1016/j.measurement.2019.107381.

[49] W. Hernandez, Sensors 6 (2006) 697–711. https://doi.org/10.3390/s6070697.

[50] I. Muller, R. De Brito, C.E. Pereira, V. Brusamarello, IEEE Instrum. Meas. Mag. 13 (2010) 15–19. https://doi.org/10.1109/MIM.2010.5399212.

[51] A. Karaus, H. Paul, Measurement 10 (1992) 133–139. https://doi.org/10.1016/0263-2241(92)90009-S.

[52] G. Levi, M. Karel, Food Res. Int. 28 (1995) 145–151. https://doi.org/10.1016/0963-9969(95)90798-F.

[53] M.J. Pikal, S. Shah, Int. J. Pharm. 62 (1990) 165–186. https://doi.org/10.1016/0378-5173(90)90231-R.

[54] D.S. Souza, L.G. Marques, E. de B. Gomes, N. Narain, Dry. Technol. 33 (2015) 194–204. https://doi.org/10.1080/07373937.2014.943766.

[55] R.J. Brandão, M.M. Prado, L.G. Marques, Defect Diffus. Forum 365 (2015) 11–16. https://doi.org/10.4028/www.scientific.net/ddf.365.11.

[56] K. Altay, A.A. Hayaloglu, S.N. Dirim, Heat Mass Transfer 55 (2019) 2173–2184. https://doi.org/10.1007/s00231-019-02570-9.

[57] W. Liu, M. Zhang, B. Adhikari, J. Chen, Innov. Food Sci. Emerg. Technol. 66 (2020) 102516. https://doi.org/10.1016/j.ifset.2020.102516.

[58] X. Duan, X. Yang, G. Ren, Y. Pang, L. Liu, Y. Liu, Dry. Technol. 34 (2016) 1271–1285. https://doi.org/10.1080/07373937.2015.1099545.

[59] X. Cao, M. Zhang, A.S. Mujumdar, Q. Zhong, Z. Wang, Ultrason. Sonochem. 40 (2018) 333–340. https://doi.org/10.1016/j.ultsonch.2017.06.014.

[60] T. Baysal, N. Ozbalta, S. Gokbulut, B. Capar, O. Tastan, G. Gurlek, F. Engineering, M. Engineering, K. Tarihi, J. Therm. Sci. Technol. 35 (2015) 135–144. http://tibtd.org.tr/2015-1/135-144.pdf.

VANESSA DAL-BÓ[1]
HEITOR OTACÍLIO NOGUEIRA ALTINO[1,2]
JOSÉ TEIXEIRA FREIRE[1]

[1]Federal University of São Carlos, Department of Chemical Engineering, Drying Center of Pastes, Suspensions and Seeds, São Carlos, São Paulo, Brazil

[2]Federal University of Uberlandia, Faculty of Chemical Engineering, Uberlândia, MG, Brazil

NAUČNI RAD

RAZVOJ SISTEMA ZA PRAĆENJE PROCESA PROIZVODNJE UZORAKA OSUŠENIH ZAMRZAVANJEM: JEDNOSTAVAN I JEFTIN PRISTUP

Prikupljanje podataka iz procesa sušenja zamrzavanjem je važno za dobijanje liofiliziranih uzoraka sa željenim konačnim sadržajem vlage u različitim radnim uslovima. Ovo istraživanje opširno predstavlja jednostavnu i jeftinu metodologiju za implementaciju sistema za prikupljanje podataka u laboratorijskoj sušari zamrzavanjem. Rezultati su pokazali da više temperature sušenja (40 °C) povećavaju greške u merenju mase materijala; ipak, primena ispravnih praznih krivih je statistički značajno smanjila te greške. Generalno, razvijeni sistem je obezbedio precizna i tačna merenja vremenskih promena mase i temperature uzoraka, kao i varijacije pritiska u komori, omogućavajući praćenje procesa proizvodnje zamrzavanjem osušenih uzoraka sa niskim sadržajem finalne vlage..

Ključne reči: liofilizacija, sušenje, zamrzavanje, temperatura grejanja, Arduino, avokado.

CI&CEQ
Chemical Industry & Chemical Engineering Quarterly

Available online at
Association of the Chemical Engineers of Serbia AChE
www.ache.org.rs/CICEQ

Chem. Ind. Chem. Eng. Q. 30 (2) 123–133 (2024) CI&CEQ

KADHUM AUDAA JEHHEF[1]
MUSAAB KADEM RASHEED[2]
MOHAMED ABED AL ABAS SIBA[2]

[1]Technical Engineering College, Baghdad, Middle Technical University, Baghdad, Iraq

[2]Institute of Technology, Middle Technical University, Baghdad, Iraq

NUMERICAL SIMULATION OF THE OSCILLATING THIN PLATE IMPACT ON NANOFLUIDS FLOW IN CHANNEL

Article Highlights

- The titled oscillating thin plate inside the flow direction increases pressure drop
- The pressure increased from 2.61 to $6.21 \cdot 10^3$ Pa when increasing the plate angle from 30 to 90°
- The Nusslet number increases by 8% when decreasing the angle from 90° to 60° near the thin plate
- Increasing the inclined angle from 30° to 90°, the maximum drag force increased from 220 to 850 N/m

Abstract

The present numerical study aims to present the effect of a titled oscillating thin plate with different inclination angles on the Al_2O_3-water nanofluid flow and heat transfer performance. The subsequent work establishes methods for forming fluid-structure interactions by the impact of Al_2O_3-water nanofluid at 0.1-1.0 vol. % volume fraction upon the thin plate using COMSOL Multiphysics 5.4. The turbulent model is solved using the (k-ε) model, and the flow assembly around the thin plate obstacle has been confirmed at the Reynolds number of $Re=4\times10^4$. It exemplifies how Nanofluid flow interaction can distort structures. The turbulent, two-dimensional, stationary, and incompressible flow around an oscillating thin plate with inclined angles with upstream and downstream mounted inside a horizontal channel was studied. The numerical study includes an investigation of the effect of five inclination angles of the thin plate (30, 60, 90, 120, and 150°) on the pressure, velocity, and temperature contours of the Al_2O_3-water nanofluid. Also, the study presented the drag profile and left a force on the thin plate caused by the fluid flow. The results showed that a titled oscillating thin plate inside the flow direction increases pressure drop, von Mises deformation stress, x-displacement and drag force fields, and the Nusselt number. Where the pressure increased from 2.61×10^3 to 6.21×10^3 pa, the von Mises stress increased from 4.43×10^6 to 1.78×10^7 N/m, and the X-displacement increased from 1.6 to 5.5 mm when increasing the plate angle from 30 to 90°.

Keywords: fluid-structure interactions, Lagrangian-Eulerian (ALE) technique, Multiphysics, nanofluid.

SCIENTIFIC PAPER

UDC 51:53:66

The study of the hydrodynamic forces behavior on thin plates can oscillate in relation to the regimes of observable flow. Many quantitative and qualitative researches on the flow arrangements were used to classify the corresponding performance of the hydrodynamic forces. Investigate the flow rate patterns in the variety enclosed performance of zones of diverse flowrate and study the influence of these flow rates on the fluid pressure of thin plate upstream flow. Among much experimental research alarmed with solid structures with sharp edges, the effect of solid flat plates on the aerodynamic characteristics at various attack inclinations in an oscillatory movement was

Correspondence: M.K. Rasheed, Institute of Technology, Middle Technical University, Baghdad, Iraq.
E-mail: musaabk.rasheed@mtu.edu.iq
Paper received: 1 April, 2023
Paper revised: 12 June, 2023
Paper accepted: 23 June, 2023

https://doi.org/10.2298/CICEQ230401017J

considered by Okajima *et al.* [1].

Carberry *et al.* [2] studied a circular cylinder at $Re < 10^4$ to measure the effect of the circular cylinder's presence on the sinusoidal oscillations transverse to a uniform stream. Outcomes showed several performances of fluid action and transitions passed through the Strouhal frequency would change only slightly during the transition. Sarpkaya [3] examined the simple examination to achieve the limitations of monitoring the crosswise vibration by vortex-induced of the rigid cylinder. The limitations as the density of the fluid, flow speed, cylinder length, cylinder diameter, spring constant, and structural damping factor were studied. Mao *et al.* [4] explored the flow oscillating near the parallel plates placed in a vertical wave resonator. As a result, the Reynolds number vagaries, a range of distinct flow patterns is reported for the fluid being expelled from the stack.

Dahl [5] specified the flow of natural instability that happens at the frequency of Strouhal. The vortex frequency detaching will be associated with the frequency of structural oscillation when the structure (body) moves. The results showed that the frequency band grows, accumulated in the amplitude of fluid motion. Lee and Allen [6] detected that softer structures take a wider “lock-in” band than harder solid constructions. Therefore, the parameters of mass, stiffness, and damping of interest control the response amplitude.

Amandolèse and Hémon [7] used a square tube in the flow of the storm channel. The free vibrations indicated the self-excited vibration. Numerous donations have been made to increase the kinematics of vibrations of self-excited solid cylinders. Yang [8] examined a bluff structure placed in a fluid flow by subjecting it to VIV. The VIV is a flat plate oscillation with a lone rotating notch of freedom. The result specified that reverberation seems a huge rejoinder bounty happens in the “lock-in” region. Lam *et al.* [9] used FSI (Fluid Structure Interaction) of cylindrical structures to examine the meaningful advance in understanding unsteady phenomena. The occurrence of structures with sharp edges can meaningfully change the behavior of fluid flow problems by viscous layer departure. Shrestha *et al.* [10] accessible a trial investigation on plate oscillations flooded in a Newtonian fluid. The FSI tricky is examined by particle image velocimetry (PIV). The results showed the association between vortex shedding and flow physics.

Zhang and Ishihara [11] calculated the coefficients of the hydrodynamic of multiple plates in fluctuating streams. LES (Large eddy simulations) of fluid with the finite volume method is used to calculate the fluid forces on oscillated plates. Sun *et al.* [12] investigated the effect of flow-induced vibration (FIV) caused by a deformable fin on the convective heat exchange mechanism. Also, the properties of heat transmission for various fin rigidity combinations were studied. The results showed that forced convection heat transfer can significantly increase when the fin exhibits large-amplitude oscillation. Yaseen and Ismael [13] focus on how a baffle designed to improve heat transmission in an open trapezium filled with non-Newtonian fluid deflects. A parallel plate channel and a trapezoidal cavity make up the computational domain. A flexible baffle is hung on the channel's top wall, with its free end pointing toward the cavity's center. The flow in the channel and the convective currents are affected by the baffle's interactions.

Ram *et al.* [14] offered a mathematical model to examine non-Newtonian Casson fluid flow in the presence of radiation, thermo-diffusion, and Ohmic dissipation over an infinite vertical plate domain. The results showed that magnetic and radiation fields increased heat distribution and improved yield stress through an enhancement in the Casson term decreased the flow speed. Usman *et al.* [15] discussed the heat transfer in the Williamson fluid flow, in a ciliated channel with a magnetic field and porous medium. The intended problem mathematical model complicates the PDE system in different dissipation. The conduction process escalated the heat transfer through the liquid molecules.

Shamshuddin *et al.* [16] studied the influence of Hall current, heat source, and Soret number in a rotating channel by describing three-dimensional mixed convection flow with convective mass and heat transfer on a squeezing nanofluid. Material properties were studied by deploying a nanoscale formulation with the Tiwari-Das model. The findings show that the squeezing term enhances the flow rate motion but decreases species diffusion and nanoparticle conductivity. Salawu *et al.* [17] investigated theoretically the thermal ignition and double exothermic combustible reaction for a viscous liquid in a channel. The flow is propelled by the upper wall motion, reaction activation energy, and pre-exponential chemical kinetics that activate the inner temperature. The dimensionless viscoelastic exothermic reaction model solutions are obtained by integrating collocation-weighted residual techniques. Shamshuddin *et al.* [18] presented a theoretical study on a micropolar fluid medium channel in mixed and nonlinear convection with the assumptions of reactive agent species and thermal radiation. It was found that the concentration, dimensionless velocity, and temperature of the micropolar fluid have a maximum value at the center of the channel.

A few works studied the interaction between the nanofluid flow and the titled movable thin plate. This work is dedicated to the problem of harmonic oscillations of titled thin plates with numerous inclination angles using a viscous incompressible nanofluid. Also, the two-dimensional flows caused by the plate oscillations and their hydrodynamic effect on the plates were investigated. The fluid motion is described by the non-stationary Navier-Stokes equations, which are solved numerically based on the finite volume method. The simulation is carried out for plates with different angles of control parameters of the oscillatory process. The analysis of the flow hydrodynamic effects on the plates allows the establishment of new effects associated with the influence of the shape on the drag and inertia forces. The present numerical simulation focused on the effect of oscillating thin plate inclination angles on the hydrodynamic forces and heat transfer of Al_2O_3-water nanofluid at 0.2-1.0 vol.% volume fraction flow upon the thin plate using COMSOL Multiphysics 5.4.

METHODOLOGY AND ANALYSIS

Model geometry

The present model includes a thin plate as an obstacle and a narrow vertical structure that achieved in the middle of a horizontal flow channel as a model geometry as presented in Fig.1. Al_2O_3-water nanofluid flow inlets to the horizontal flow channel as a fully developed flow from the left of the channel and exit from the right and the Al_2O_3-water nanofluid flow will strike the obstacle flat plate powers the fluid flow paths toward the upper part of the duct. The thin plate structure was made from a deformable material that will bend under the applied force of the moving fluid. The dimension of the flow channel chosen as the channel length is 100 cm and the channel height is 10 cm and the plate length is 5 cm, and the thin plate thickness is 1 cm.

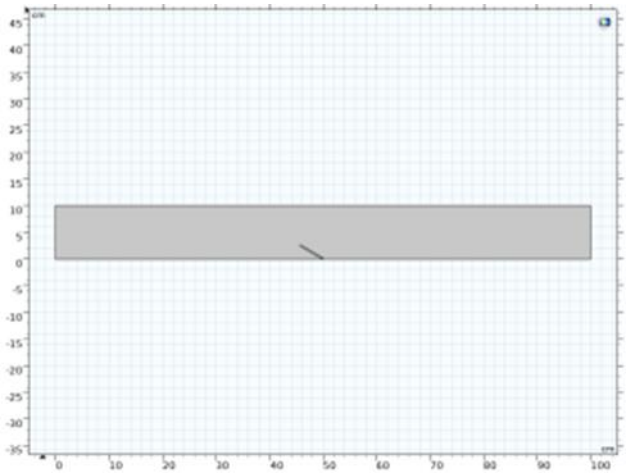

Figure 1. Model geometry of flow domain of present problem (all dimensions in cm).

Governing Equations

Fluid deformed mechanics

The Al_2O_3-water nanofluid current in the duct flow is defined using the equations of Navier-Stokes of pressure (p) and velocity u = (u, v) in the coordinate of deformed moving as follows:

Mass conservation equation:

$$\nabla u = 0 \tag{1}$$

Momentum conservation equation:

$$\rho\frac{\partial u}{\partial t} - \nabla\cdot\left[-pI + \eta\left(\nabla U + (\nabla U)^T\right)\right] + \rho\left((u-u_m)\cdot\nabla\right)u = F \tag{2}$$

Energy equation:

$$\frac{\partial}{\partial t}(\rho E) + \nabla\left(\vec{v}(\rho E + p)\right) = \nabla\left[k_{eff}\nabla T - \sum_j h_j J_j + \left(\overline{\overline{\tau}}\vec{v}\right)\right] + S_h \tag{3}$$

Assume that no gravitation that affects the Al_2O_3-water nanofluid F = 0.

Turbulent kinetic energy

$$\frac{\partial uk}{\partial x} + \frac{\partial vk}{\partial y} = \frac{1}{\rho}\frac{\partial}{\partial x}\left[\left(\mu + \frac{\mu_t}{\sigma_k}\right)\frac{\partial k}{\partial x}\right] + \frac{1}{\rho}\frac{\partial}{\partial y}\left[\left(\mu + \frac{\mu_t}{\sigma_k}\right)\frac{\partial k}{\partial y}\right] + \frac{1}{\rho}(G_k - G_b) - \varepsilon \tag{4}$$

Dissipation rate (Ɛ)

$$\frac{\partial u\varepsilon}{\partial x} + \frac{\partial v\varepsilon}{\partial y} = \frac{1}{\rho}\frac{\partial}{\partial x}\left[\left(\mu + \frac{\mu_t}{\sigma_\varepsilon}\right)\frac{\partial \varepsilon}{\partial x}\right] + \frac{1}{\rho}\frac{\partial}{\partial y}\left[\left(\mu + \frac{\mu_t}{\sigma_\varepsilon}\right)\frac{\partial \varepsilon}{\partial y}\right] + C_1\frac{\varepsilon}{\rho k}(G_k + C_3G_b) - C_2\frac{\varepsilon^2}{k} \tag{5}$$

Where μ_{eff} is effective viscosity coefficient

$$\mu_{eff} = \mu + \mu_t \tag{6}$$

Γ_{eff} is effective diffusion coefficient

$$\Gamma_{eff} = \frac{\mu}{p_r} + \frac{\mu_t}{\sigma_t} \tag{7}$$

μ_t is turbulent viscosity

$$\mu_t = \rho C_\mu\frac{k^2}{\varepsilon} \tag{8}$$

$$S_u = -\frac{2}{3}\frac{\partial k}{\partial x} \tag{9}$$

$$S_v = g\beta(T_f - T_{in}) \tag{10}$$

G_k is kinetic energy generation by shear

$$G_k = \mu_t \left(2\left[\left(\frac{\partial u}{\partial x}\right)^2 + \left(\frac{\partial v}{\partial y}\right)^2 \right] + \left(\frac{\partial u}{\partial y} + \frac{\partial v}{\partial x}\right)^2 \right) \quad (11)$$

G_b is kinetic energy generation by buoyancy

$$G_b = \frac{\mu_t}{\sigma_t} \frac{\partial T}{\partial y} g\beta \quad (12)$$

where "Cμ " is the value of an empirical constant for a flow with a high Reynolds number. The working fluid is air, which has a Prandtl number of (0.7) and produces a uniform heat flux on the absorber wall. The values of constants in the (K–Ɛ) models are presented in Table.1.

Table 1. Values of constants in the (K–Ɛ) models [15].

C μ	C_1	C_2	C_3	σ_ε	σ_k
0.09	1.44	192	1.0	1.3	1.0

Local heat transfer coefficient (h_x)

$$h_x = \frac{k_f \left(\partial T / \partial y \right)_{y=0}}{(T_s - T_b)} \quad (13)$$

Local Nusselt number can be calculated from:

$$\overline{Nu}_x = \frac{h_c D_h}{K_f} = -\frac{1}{\theta_w} \frac{\partial \theta}{\partial \overline{n}} \quad (14)$$

The mean Nusselt number can be calculated from:

$$\overline{Nu}_m = \frac{1}{A} \int_A Nu_x dx \quad (15)$$

To demonstrate the desired techniques, the following assumption will be illustrated:

1. Turbulent fluid flow.
2. Two-dimensional.
3. Stationary and incompressible flow around an oscillating thin plate.
4. Assume that the structure is long in the direction perpendicular to the image.
5. Assume the structure consists of a flexible material with a density ρ = 7850 kg/m^3 and Young's modulus E = 200 kPa.

Assume that no gravitation or other volume forces affect the fluid so that F = 0.

Solid structural mechanics

Deformations of the solid structure are resolved through nonlinear geometry formulation and an elastic preparation to agree with the deformations of the solid. The thin plate hitch is attached at the bottom side of the bottom wall of the fluid flow duct. All other object borders involved a weight of the Al_2O_3-water nanofluid flow is given by:

$$F_T = -n\left(-pI + \eta\left(\nabla u + (\nabla u)^T\right)\right) \quad (16)$$

where n is the normal vector on a flat plate. This force denotes the sum of the viscous and pressure forces in the nanofluid flow.

Boundary conditions

At the left-hand of the inflow of the inlet of the duct boundary, the flow is considered laminar flow and fully developed at the inlet of the duct with a parabolic profile velocity. The velocity grows and gets its peak value at 0.215 and then falls to 5 cm/s, representing a steady-state value. The velocity at the centerline in the x-axis (u_{in}) comes from:

$$u_{in} = \frac{Ut^2}{\sqrt{\left(0.04 - t^2\right)^2 + (0.1t)^2}} \quad (17)$$

At the right-hand of the outflow of the channel, the boundary condition is p = 0. At the channel's top and bottom solid walls (non-deforming boundary condition), the no-slip boundary conditions are imposed: u = 0, v = 0.

At the top and sides of the thin plate's solid (deforming) walls and on the deforming, the deformation velocities boundary conditions are $u_0 = u_t$ and $v_0 = v_t$.

The fixed boundary was chosen at the thin plate's bottom solid (deforming) wall. The working fluid (Al_2O_3-water nanofluid) flows through it with various flow rates (1, 3, 5, and 7 LPM). Fig. 2 demonstrates the nanofluid channel's physical model and boundary state with an oscillating thin plate. More information for the BC (Boundary condition) was implemented in statistical models and inclined thin plates to analyze the energy balance of the main components.

Thermophysical properties of nanofluids

Introducing the volume fraction of Nanofluid, the thermophysical properties of the Nanofluid (density and heat capacity) have been estimated from the pure fluid and Nanoparticle properties at the ambient temperature. The thermophysical properties of nanofluids used in the present study are for a mixture of the water and Al_2O_3, CuO, and TiO_2 nanoparticles with a diameter of 20 nm. The values of density, specific heat, dynamic viscosity, and thermal conductivity for the base fluid and considered nanoparticles were reported in table.2. Also, the solid properties of the steel

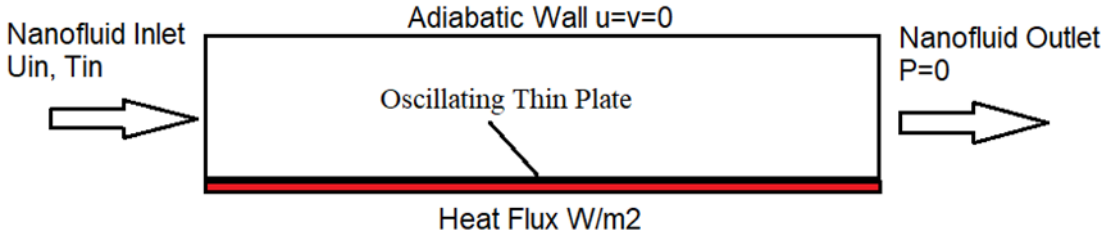

Figure 2. Geometry distribution and boundary conditions.

used in pore-level simulations were listed in Table 3. In the present study, a single-phase model is adopted, and the following equations are used to compute the thermal-physical properties of considered nanofluids.

Table 2. Water and Nanofluid properties used in present simulations [19].

Fluid properties	Water	Al_2O_3-nanofluids
ρ [Kg/m^3]	997.0	1057.17
μ [Kg/m. s]	8.899E-4	0.00169
Cp [J/Kg. k]	4181.7	3526.68
k [W/m. k]	0.6069	0.441

Table 3. Solid properties of the steel used in pore-level simulations [19].

Properties	Steel
Density [Kg/m^3]	7850
Young's modulus E [Pa]	2×10^5
Poisons ratio $^{\nu}$ [-]	0.33

Density

Equation of general relationships used to compute the effective density for a classical two-phase mixture given by Pak and Cho [19]:

$$\rho_{nf} = \varnothing\rho_p + (1-\varnothing)\rho_f \tag{18}$$

Specific heat

Calculation of the effective specific heat of nanofluid is straightforward. It can be based on the physical principle of the mixture. The specific heat is calculated from general relationships used to compute the effective specific heat at the reference temperature (T_{in}) for a classical two-phase mixture [20]:

$$Cp_{nf} = \frac{\varnothing\rho_p Cp_p + (1-\varnothing)\rho_f Cp_f}{\rho_{nf}} \tag{19}$$

Thermal expansion

Equation of general relationships used to compute the effective thermal expansion at the reference temperature (T_{in}) for a classical two-phase mixture given by Maiga *et al.* [21]:

$$B_{nf} = \frac{\varnothing\rho_p B_p + (1-\varnothing)\rho_f B_f}{\rho_{nf}} \tag{20}$$

Dynamic viscosity

The effective viscosity is calculated with the Einstein equation, which applies to spherical particles in volume fractions of less than 5.0 vol.% and is defined as follows [22]:

$$\mu_{nf} = \frac{\mu_f}{(1-\varnothing)^{2.5}} \tag{21}$$

Thermal conductivity

For particle-fluid mixtures, numerous theoretical studies have been conducted dating back to the classical work of Maxwell [23]. The effective thermal conductivity of the fluid can be determined by Maxwell-Garnett's (MG) model). For the two-component entity of spherical-particle suspension, the MG model gives:

$$k_{nf} = \left[\frac{k_p + 2k_f - 2\varnothing(k_f - k_p)}{k_p + 2k_f + \varnothing(k_f - k_p)}\right]k_f \tag{22}$$

Maxwell's formula shows that nanofluids' effective thermal conductivity relies on the spherical particle's thermal conductivity, the base fluid, and the volume fraction of the solid particles.

Solution method

The governing equations of Navier-Stokes are analyzed and explained on the mesh of a movable deformed flat plate of the commotional field, which establishes the Al_2O_3-water nanofluid flow. The mesh deformation is compared to the field's initial solid flat plate shape, calculated using the Hyperelastic smoothing method. The nearby and insider mesh of the moving plate will track the plate deformations. However, the flat plate deformation is fixed at zero in all instructions at the exterior boundaries of the nanofluid flow field. The method of Lagrangian- Eulerian adjustments the dynamic forces of the flat plate's deforming structure and the moving grid's

moving boundaries. COMSOL Multiphysics was used to investigate the systematization of the new mesh based on the solid flat plate structure's movement with mesh smoothing, as shown in Fig. 3.

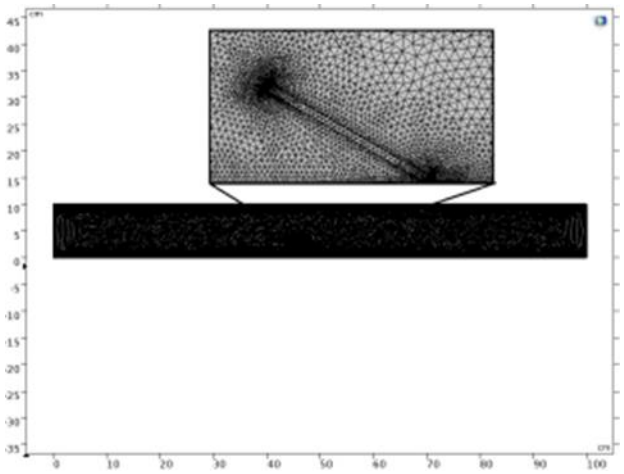

Figure 3. Mesh flow domain of the present problem.

RESULTS AND DISCUSSION

In the present numerical simulation, the nanofluids flow field supported out numerically has been equipped to confirm the Al_2O_3-water nanofluid flow appearances of the thin plate attached on the horizontal bottommost surface of the nanofluid flow duct with a height of H=10 cm and length of L=100 cm with obstacle thin plate with a height of 5 cm and a thickness of 0.5 cm placed in the middle of the channel. The assembly of the flow around the thin plate obstacle was confirmed at a Reynolds number of $Re = 4 \cdot 10^4$. The pressure distribution results in the channel are shown in Fig.4. The pressure varies with increasing the angle of the thin plate, where the pressure increased from 2.61 kPa to 6.21 kPa when increasing the plate angle from 30° to 90°. The inlet pressure changed from a low value in the case of the angle of inclination 30° and 60° of upstream angles and 120 and 150° of downstream angles. The high pressure of the inlet section is located at an inclination angle of 90° due to the blocked flow stream of the Al_2O_3-water nanofluid.

The results of the velocity contours were plotted in Fig.5. The Upstream of the obstacle thin plate, as the inclination angle in the upstream portion (30° and 60°), the flow was increased, and easy to pass the obstacle. But when the angle is put at 90°, a ratio of the Al_2O_3-water nanofluid remains choked, and a generation of small recirculation region is observed after the thin plate obstacle. However, in the downstream region of the thin plate obstacle, there is a great whirlwind, and the separation is activated. The results indicated that the thin plate obstacle in the flow field causes the separation of the fluid flow in the channel. The nanofluid flow field formulae a recirculation region near the thin plate, which increases the intensity of the turbulence due to increasing the angle of inclination from 30° to 90°. The velocity of the nanofluid grows progressively until it is attached to the near-back edge with the separation of the nanofluid flow. The length of the recirculation zone on the lower wall of the channel was indicated by the length near the thin plate, as mentioned in Fig.6. The results showed that the large area of separation developed behind the thin plate at an angle of inclination of 90°.

Heat transfer analysis

The effect of the thin plate angle of inclination on the temperature distribution in the channel is presented in Fig.S1 (Supplementary material). The results showed that increasing the thin plate angle of inclination led to decreasing the temperature in the upstream region of the thin plate from 31.02, 29.72, 29.17, 28.41, and 27.72 °C as increasing the angle of inclination from 30° to 150°, respectively, due to increasing the velocity of the nanofluid in this region. Also, the temperature in the downstream region of the thin plate increases from 30.27, 30.72, 31.42, 31.72, and 31.91°C as the inclination angle increases from 30° to 150°, respectively. Due to the decreasing velocity of the nanofluid in this region, the variation of the local Nusslet number of the heated lower surface of the channel with the increasing thin plate inclination angle was plotted in Fig.S2. The results indicated that the Nusslet number increased by 15 % when decreasing the angle from 90° to 30° and increasing by 8% when decreasing the angle from 90° to 60° in the region near the thin plate. The effect of increasing the nanoparticles' volume fraction on the local Nusselt number along the heated lower surface of the channel was illustrated in Fig. S3. The results indicated that increasing the nanoparticle volume fraction will increase the Nusslet number by about 10% when using Al_2O_3-water nanofluid instead of water.

Plate stresses analyses

Fig.S4 illustrates the geometry of the thin plate deformation of the thin plate and the stream at t = 4 s for various thin plate angles of inclination. The results indicated that a vortex exists for a small zone behind the thin plate obstacle when the flow and the moving thin plate system are near its steady state. The deformation magnitude, as well as the location and size of the vortex, are contingent on the magnitude of the velocity inflow and the thin plate angle of inclination. Therefore, the largest values of the mesh velocity are also near the thin plate. The results showed that the von Mises stress increased from 4.43×10^6 to 1.78×10^7 N/m when increasing the angle of inclination from 30° to 90°.

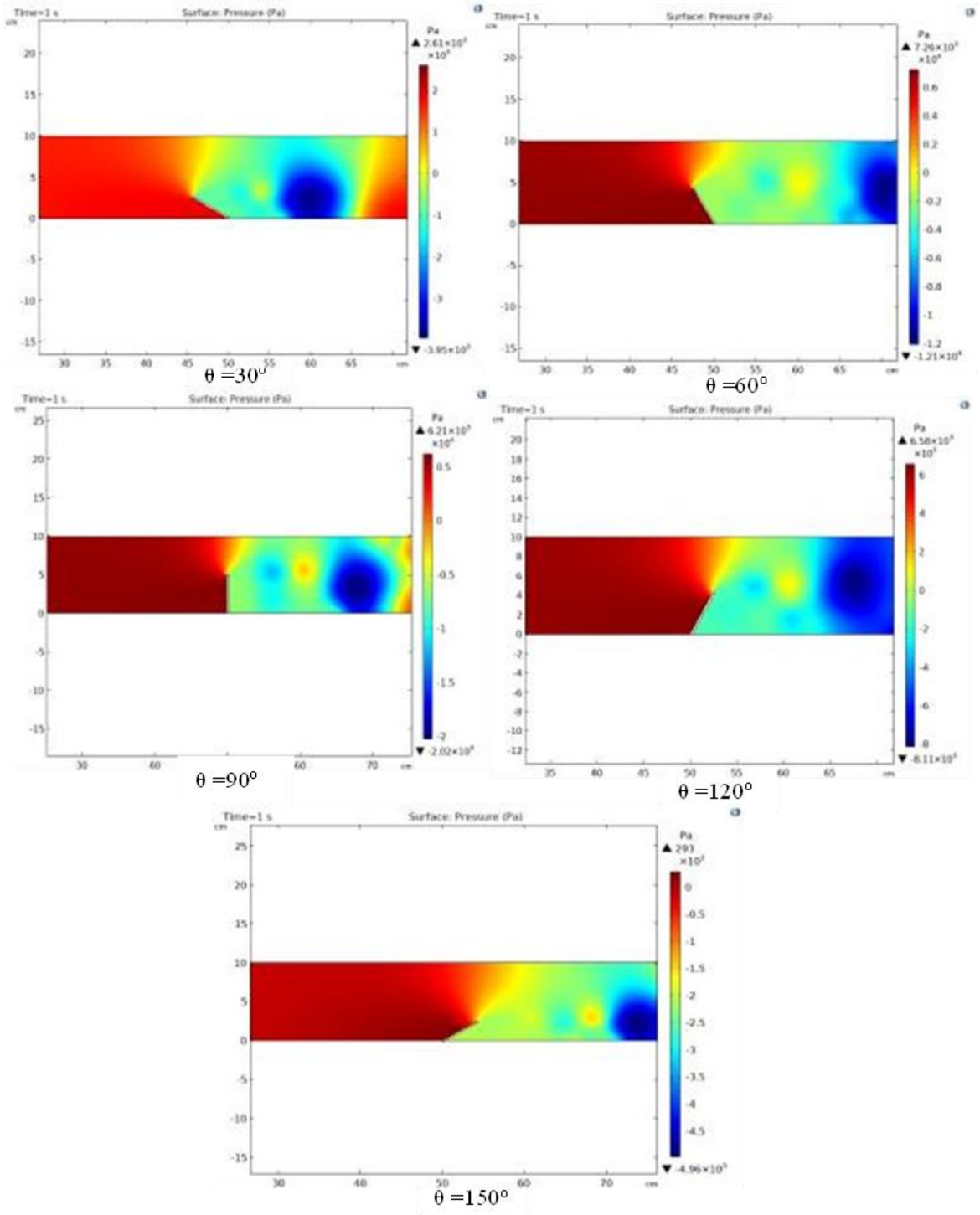

Figure 4. Nanofluid flow pressure for various thin plate obstacle angles at t = 4 s.

Whenever the angle of inclination starts to increase from 90° to 150°, the decrease of the thin plate deformation can be seen in the adverse velocity magnitude on the horizontal walls.

The effect of using different thin plate inclination angles on the drag force (left) and Y-displacement (right) with time was illustrated in Fig.S5. The outcomes display that the increasing the inclination angle from 30° to 90°, the maximum drag force will increase from 220 to 850 N/m; due to increasing the flow interception, the nanofluid flow and the thin plate will be perpendicular to the stream fluid flow in the case of the inclination angle of 90°.

Also, the X-displacement will have increased from 1.6 to 5.5 mm when increased the inclination angle from 30° to 90°. But the Y-displacement will decrease from 2.8 to 0 mm when the inclination angle increases from 30° to 90°.

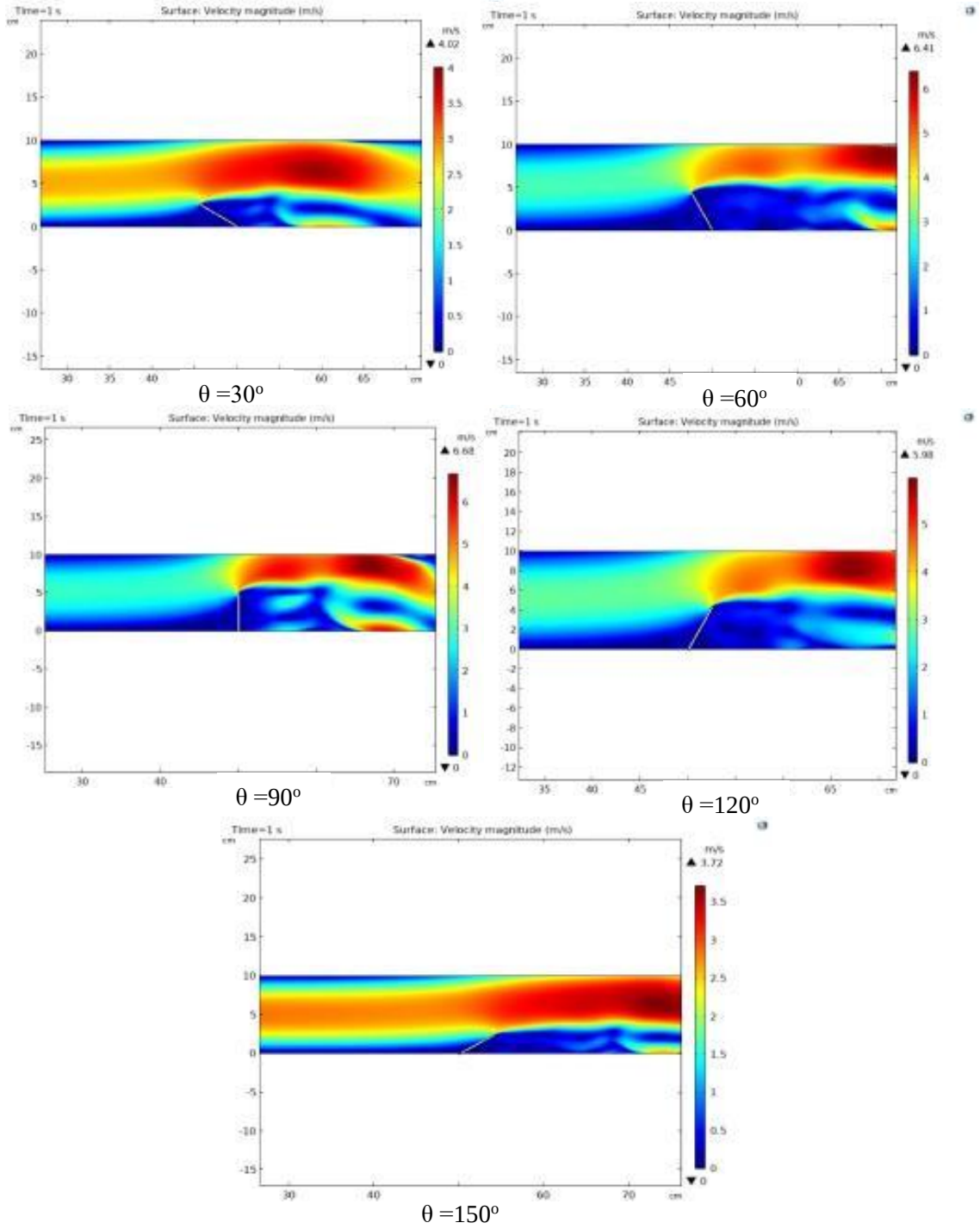

Figure 5. Nanofluid flow velocity for various thin plate obstacle angles at t = 4 s.

CONCLUSION

The numerical model presented in this simulation study is a 2D Al_2O_3-water nanofluid flow simulation by expanding the COMSOL Multiphysics 5.4 of turbulent flow around an inclined thin plate. The numerical results are presented as pressure contours, velocity contours, velocity vector, von Mises deformation stress, X and Y-displacement, and drag force fields. The effect of the nanofluid flow characteristics on the inclined thin plate obstacle deformation as a function of the Reynolds number of $Re=4\times10^4$ has been calculated with k-ε turbulence models. The results showed that an inclined thin plate obstacle in the flow direction leads to an increased pressure drop, von Mises deformation stress, X-displacement field, and drag force field. Also, increasing the inclined thin plate will increase these variables of the flow due to the interface between vortex

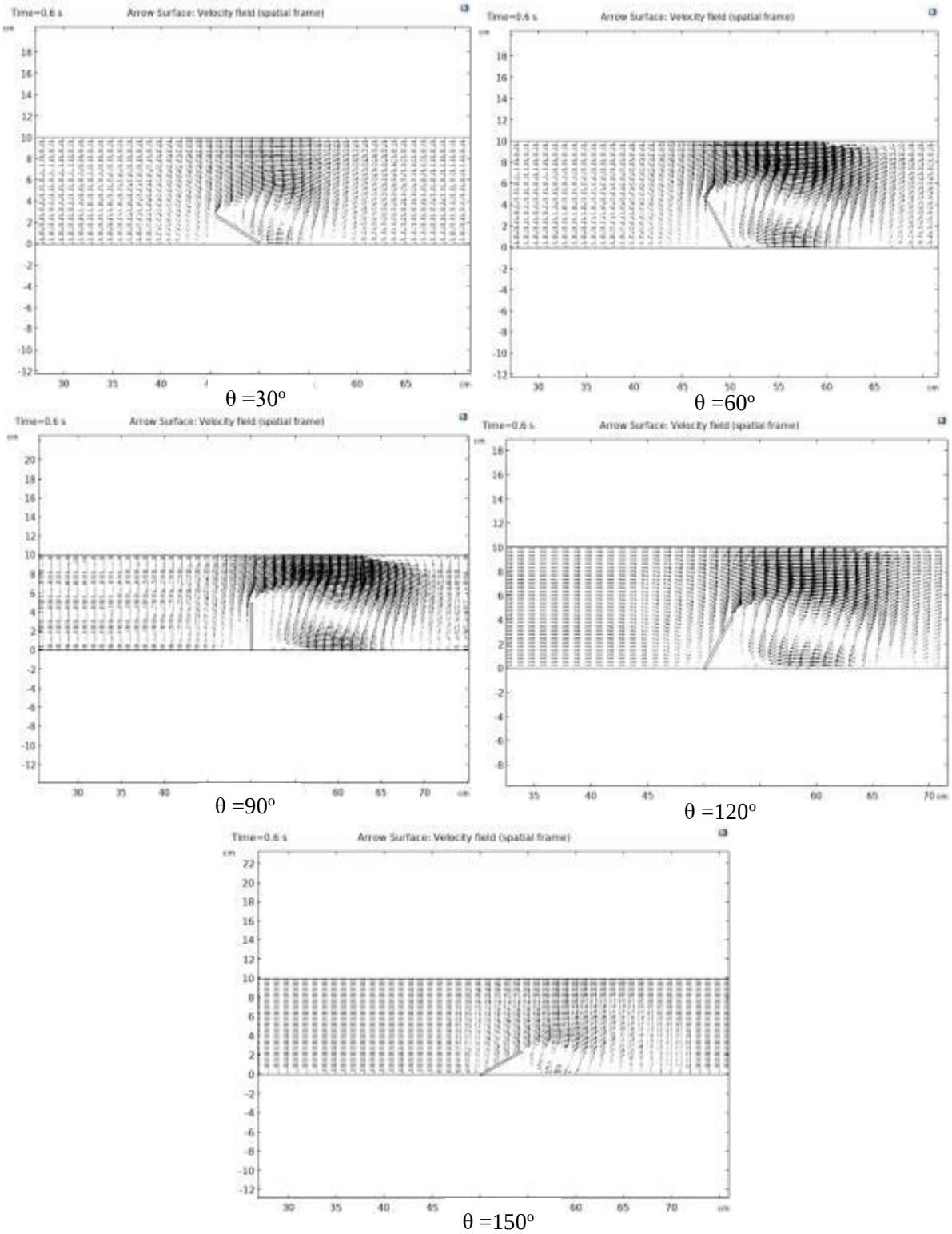

Figure 6. Nanofluid flow velocity vector for various thin plate obstacle angles at t = 4 s.

recirculation of the main nanofluids flow producing high recirculation vortex zones behind the thin plate. The result indicated that the Nusslet number increased by 15 % when the angle decreased from 90° to 30°. However, the results indicated that increasing the nanoparticle volume fraction will increase the Nusslet number by about 10% when using Al_2O_3-water nanofluid instead of water. In addition, the pressure increased from 2.61×10^3 to 6.21×10^3 Pa, the von Mises stress increased from 4.43×10^6 to 1.78×10^7 N/m, and

the X-displacement increased from 1.6 to 5.5 mm when increasing the plate angle from 30 to 90°.

NOMENCLATURE

I	The matrix of unit sloping
F	Force of volume disturbing of Al_2O_3-water nanofluid
n	Formal vector on a flat plate
Cp	Fanofluid specific heat capacity (J/kg K)
d	Particle diameter (m)
Dh	Hydraulic diameter (m)
f	Fluid friction factor (-)
Q	Fluid volumetric flowrate (m^3/s)
k	Thermal conductivity (W/m K)
k_B	Boltzmann constant (1.38×10^{-23}J/K)
L	Duct length (m)
P	Pressure (Pa)
PP	Pumping power (W)
Pe	Peclet number (-)
Qh	Heat flux (W)
Re	Reynolds number (-)
u	Fluid velocity (m/s)
x	Distance along duct cross section (m)
t	Time (sec)

Greek symbols

β	Thermal expansion coefficient, (1/K)
ϕ	Particle volume fraction (-)
μ	Viscosity (Pa.s)
ρ	Density (kg/m^3)

REFERENCES

[1] A. Okajima, T. Matsumoto, S. Kimura, JSME Int. J., Ser. B 41(1998) 214. https://doi.org/10.1299/jsmeb.41.214.

[2] J. Carberry, J. Sheridan, D.O. Rockwell, J. Fluids Struct. 15 (2001) 523–532. https://doi.org/10.1006/jfls.2000.0363.

[3] T. Sarpkaya, J. Fluids Struct. 19 (2004) 389–447. https://doi.org/10.1016/j.jfluidstructs.2004.02.005.

[4] X. Mao, Yu. Zhibin, Æ. Artur, J. Jaworski, D. Marx, Exp. Fluids 45 (2008) 833–846. https://doi.org/10.1007/s00348-008-0503-7.

[5] M. Dahl Jason, Ph.D. Thesis, Massachusetts Institute of Technology, (2008). http://hdl.handle.net/1721.1/44747.

[6] L. Lee, D. Allen, J. Fluids Struct. 26 (2010) 602–610. https://doi.org/10.1016/j.jfluidstructs.2010.02.002.

[7] X. Amandolèse, P. Hémon, Comptes Rendus Mécanique 338 (2010) 12–17. https://doi.org/10.1016/j.crme.2009.12.001.

[8] Y. Yang, M.Sc. Thesis, The Texas A&M University (2010).

[9] K. Lam, J.C. Hu, P. Liu, Phys. Fluids 22 (2010) 015105. https://doi.org/10.1063/1.3291069.

[10] B. Shrestha, S.N. Ahsan, M. Aurelia, Phys. Fluids 30 (2018) 013102. https://doi.org/10.1063/1.5001330.

[11] S. Zhang, T. Ishihara, Ocean Eng. 163 (2018) 583–598. https://doi.org/10.1016/j.oceaneng.2018.03.060.

[12] X. Sun, Y. Zehua, L. Jiajun, K. Wen,H. Tian, Int. J. Heat Mass Transfer 128 (2019) 319–334. https://doi.org/10.1016/j.ijheatmasstransfer.2018.08.123.

[13] D. Yaseen, M.A. Ismael, Exp. Tech. 47 (2022) 37–46. https://doi.org/10.1007/s40799-022-00554-9.

[14] S. Ram, N. Ashok, MD. Shamshuddin, J. of Nanofluids 12 (2023) 777–785. https://doi.org/10.1166/jon.2023.1976.

[15] Usman, S. Shaheen, M.B. Arain, K. S. Nisar, A. Albakri, MD. Shamshuddin, F. O. Mallawi, C. Stud. in Ther. Eng. 41(2023) 102523. https://doi.org/10.1016/j.csite.2022.102523.

[16] MD. Shamshuddin, F. Mabood, W. A. Khan, G. R. Rajput, Heat Trans. 52 (2023) 854–873. https://doi.org/10.1002/htj.22719.

[17] S.O. Salawu, R.A. Kareem, M.D. Shamshuddin, S.U. Khan, Chem. Phys. Lett. 760 (2020) 138011. https://doi/10.1016/j.cplett.2020.138011.

[18] MD. Shamshuddin, P. S. Rao, S.O. Salawu and A.J. Chamkha, J. Proc. Mech. Eng. 236 (2022) 1877–1888. https://doi/10.1177/09544089221076918.

[19] B. C. Pak, Y. I. Cho, Exp. Heat Trans. 11 (1998) 151–170. https://doi.org/10.1080/08916159808946559.

[20] Y. Xuan, W. Roetzel, Int. J. Heat Mass Transfer 43 (2000) 3701–3707. https://doi.org/10.1016/S0017-9310(99)00369-5.

[21] H.C. Brinkman, J. of Chem. Phys. 20 (1952) 571–581. https://doi/10.1063/1.1700493.

[22] J.C. Maxwell, A Treatise on Electricity and Magnetism, 2nd ed., Clarendon Press, Oxford University, UK (1881).

[23] S.E. Maiga, B. Nguyen, C. Tam, G. Nicolas, R. Gilles, Superlattices and Microstructures 35 (2004) 543–557. https://doi/10.1016/j.spmi.2003.09.012.

KADHUM AUDAA JEHHEF[1]
MUSAAB KADEM RASHEED[2]
MOHAMED ABED AL ABAS SIBA[3]

[1]Technical Engineering College, Baghdad, Middle Technical University, Baghdad, Iraq

[2]Institute of Technology, Middle Technical University, Baghdad, Iraq

NAUČNI RAD

NUMERIČKA SIMULACIJA UTICAJA OSCILIRAJUĆE TANKE PLOČE NA PROTOK NANOFLUIDA U KANALU

Ova numerička studija ima za cilj da predstavi efekat oscilirajuće tanke ploče sa različitim uglovima nagiba na protok nanofluida Al_2O_3-vode i performanse prenosa toplote. Naredni rad uspostavlja metode za formiranje interakcija fluid-struktura uticajem nanofluida Al_2O_3-voda na 0,1-1,0% v/v na tankoj ploči pomoću programskog paketa COMSOL Multiphisics 5.4. Turbulentni model je rešen korišćenjem (k-ε) modela, a strujanje oko tanke ploče je potvrđen pri Rejnoldsovom broju $Re=4\times10^4$. To je primer kako interakcija protoka nanofluida može da izobliči strukture. Proučavano je turbulentno dvodimenzionalno, stacionarno i nestišljivo strujanje oko oscilirajuće tanke ploče sa nagnutim uglovima uzvodno i nizvodno, postavljene unutar horizontalnog kanala. Numerička studija obuhvata istraživanje uticaja pet uglova nagiba tanke ploče (30, 60, 90, 120 i 150°) na pritisak, brzinu i temperaturu nanotečnosti Al_2O_3-voda. Takođe, studija je predstavila profil otpora i silu na tankoj ploči uzrokovanu protokom tečnosti. Rezultati su pokazali da oscilujuća tanka ploča unutar pravca strujanja povećava pad pritiska, fon Mizesov deformacioni napon, x-pomeranje, polja sile otpora i Nuseltov broj. Tamo gde se pritisak povećao sa $2,61\times10^3$ na $6,21\times10^3$ pa, fon Mizesov napon se povećao sa $4,43\times10^6$ na $1,78\times10^7$ N/m, a x-pomeraj se povećao sa 1,6 na 5,5 mm pri povećanju ugla ploče sa 30 na 90°.

Ključne reči: interakcije fluid-struktura, Lagranž-Ojlerova tehnika, Multiphysics, nanofluid.

CI&CEQ
Chemical Industry & Chemical Engineering Quarterly

Available online at
Association of the Chemical Engineers of Serbia AChE
www.ache.org.rs/CICEQ

Chem. Ind. Chem. Eng. Q. 30 (2) 135–142 (2024) CI&CEQ

ĐORĐIJE DODER
DAMIR ĐAKOVIĆ
BORIVOJ STEPANOV
NIKOLA MILIVOJEVIĆ

University of Novi Sad, Faculty of Technical Sciences, Department of Energy and Process Engineering, Novi Sad, Serbia

OPTIMIZATION OF ENERGY CONSUMPTION DURING IMMERSION FRYING OF PEANUTS

Article Highlights

- Due to non-linear temperature behavior, the existence of an optimal set of parameters was assumed
- The best solution produced approximately 570 kJ/kg of specific energy consumption
- This regime allows twice less energy consumption than the previously reported data

Abstract

This study investigated the influence of different regimes of immersion batch frying of peanuts on its specific energy consumption. The investigation was conducted via simulation, where energy consumption was calculated using various heat power/peanut mass ratios. As the result of the applied optimization procedure within the examined domain and calculation data, it was estimated that a regime with 24 kW of heating power and 28.6 kg of peanuts gave the minimum specific energy consumption. Besides that, the resulting surface could serve as a basis for designing and operating the frying equipment in more favorable regimes in terms of energy efficiency.

Keywords: immersion frying, peanuts frying, energy consumption optimization.

SCIENTIFIC PAPER

UDC 634.58:621:66

Immersion frying (or deep-fat frying) is a process of thermal treatment of food, where food is immersed in a large volume of oil (unlike the so-called shallow or contact frying, where food is placed in the frying pan that contains a thin layer of oil), as defined by Oreopoulou *et al*. [1]. Immersion frying is a usual practice in both industrial and domestic conditions since the fried food products provide unique flavor and texture, being quite popular with customers, as reported by Rossell [2]. According to Kong *et al*. [3], peanut production in the world is 34.4 billion kg/year, and it is indicated that its consumption may have various health benefits. Deep-fried peanuts are popular in Asian countries, unlike in the USA, for instance, where peanuts are usually boiled or roasted (by roasting, contact frying is understood). Immersion frying is a complex process to describe physically, as many individual processes are involved, as described by Alvis *et al*. [4]. These processes, as mentioned by Farid and Kizilel [5], primarily refer to simultaneous heat and mass transfer, in addition to oil uptake and moisture loss. Material oil uptake and its moisture loss also appear simultaneously, as the frying oil fills the space left by the evaporated moisture, described by Ziaiifar *et al*. [6].

Frying equipment in current usage is very diverse, from various industrial fryers of different types and capacities to small-scale domestic ones, according to Sahin and Sumnu [7]. What all have in common is the immersion of material in the frying oil, which is

Correspondence: Đ Doder, University of Novi Sad, Faculty of Technical Sciences, Department of Energy and Process Engineering, Trg Dositeja Obradovica 6, 21000 Novi Sad, Serbia.
E-mail: dj.doder@uns.ac.rs
Paper received: 16 January, 2023
Paper revised: 6 June, 2023
Paper accepted: 9 July, 2023

https://doi.org/10.2298/CICEQ230116018D

previously warmed up usually at 150–200°C, as mentioned by Farkas *et al.* [8], and retention in oil for a certain time – enough to be fried, but not for too long, since the product could easily become over fried and lose its nutritional quality and flavor, which is reported by Kita and Figiel [9]. Most accessible frying systems are of smaller volume and more convenient for domestic or catering services. At the same time, large continuous fryers are typically used for industrial applications, according to Oke *et al.* [10].

In the scope of this paper is a batch frying system and, in particular, the optimization of the specific energy used for heating. Since oil is preheated to the desired temperature, the temperature drop will occur as a colder material is immersed. The observed temperature difference between the oil and the material will be highly dependent on the heating power and the amount of material that undergoes frying at a particular moment. On the other hand, the amount of material per one round of batch frying will eventually influence the overall frying time, thus will reduce the overall heat consumed. In terms of the facts mentioned above, it is reasonable to assume that such processes are suitable for optimization, which could ultimately contribute to the more efficient planning of the process. Considering the widespread presence of frying systems [7], the research on possibilities for optimal energy consumption concerning treated product mass could contribute to more energy-efficient management of existing or developing new frying systems. In such conditions, process simulation could serve as a powerful tool that should ultimately provide significant data needed for a deeper understanding of the process.

MATERIALS AND METHODS

Materials

As mentioned, peanuts without shells are used as a material for the conduction of the frying simulation. Peanuts are usually fried at temperatures between 160°C and 180°C [9], which mainly depend on the capacity of frying equipment, production rate demands, and food quality requirements, according to Shi *et al.* [11]. On the other side, as the oil commonly used for peanut frying, as reported by Erickson [12], sunflower oil is chosen for the calculation. Table 1 shows raw peanut kernel composition and the heat capacities of each component [13].

Table 1. Raw peanut composition and properties.

Initial properties	Moisture content ω_{Mi} [%]	Fat content ω_{Fi} [%]	Other components content ω_{Oi} [%]	Specific heat C_p [kJ/(kg·K)]	Volume V_p [m^3]	Density ρ_p [kg/m^3]
Value	6.50	49.24	44.26	2.23	$2.143 \cdot 10^{-6}$	617

Modeling procedure

Since several different phenomena occur during the process (heat transfer and the oil uptake in one direction, moisture removal in the other direction, crust region formation, etc.), and the internal distribution of any property must be clarified, the process is usually modeled via simultaneous heat and mass transfer relations, as reported by Tangduangdee *et al.* [14]. However, in this study, only the average temperature of a kernel needs to be estimated to compare the different frying regimes in terms of specific energy consumption. Hence, there is no need to model the internal temperature distribution and the lumped capacitance method could be applied for the kernel temperature estimation. According to Miyagi [15], peanuts should be fried for up to 15 minutes at high temperatures to achieve optimal flavor, texture, and nutritional quality. Besides that, some time will be needed to achieve the wanted frying temperature since colder kernels of peanuts are expected to cool down the oil. This occurrence will delay the start of the frying process itself, so the time of kernels warming up should also be taken into account. For all the mentioned reasons, the frying time was chosen to be 10 minutes, with additional 10 minutes allowed for the material to achieve the oil temperature.

Process modeling is based on the following assumptions:

- Change of material temperature does occur, as well as the change of temperature of the oil, due to the relatively large amount of material immersed at the beginning of the process;
- Every single kernel of peanuts is fully exposed to the surrounding oil;
- Due to the small dimensions, the internal temperature of peanut kernels changes uniformly; hence the lumped capacitance model of temperature change is adopted. Another reason is that the internal temperature distribution of kernels doesn't affect the main calculation results, but only its average temperature, as mentioned;
- Safari *et al.* [16] showed that moisture removal has a small effect on heat transfer. Still, water evaporation from peanuts' surface strongly influences the heat convection coefficient (it is called the "bubbling effect"), so the heat transfer coefficient must be assessed based on experimental results from the previous work;

- Heat carried by the oil mass transfer (during the oil uptake) is neglected since this amount of heat is considerably smaller in comparison to the convection heat transfer [14];
- Physical properties of kernels change during the process, but properties of oil don't;
- The heater works in an intermittent regime and is turned on until the temperature of the oil achieves the value of 165 °C. After that, the heater is turned off;
- The external heat loss to the surroundings occurs constantly during the process.

Considering all the mentioned assumptions, the process is modeled via a system of two ordinary differential equations, one for the oil temperature change and the other for peanuts temperature change, as follows:

$$\frac{dT_o}{dt} = \frac{-h \cdot A_p \cdot (T_o - T_p) + Q_h}{m_o \cdot c_o} \tag{1}$$

$$\frac{dT_p}{dt} = \frac{h \cdot A_p \cdot (T_o - T_p)}{m_p \cdot c_p} \tag{2}$$

The mass of oil is calculated as oil density is multiplied by its volume, which is obtained as a difference between the volumes of the vessel and immersed peanuts:

$$m_o = \rho_o \cdot (V_v - V_p) \tag{3}$$

Since peanuts mass is a function of time, where it changes in dependence on current moisture content (wet basis) and current fat content, it can be expressed as:

$$m_p(t) = m_{pi} \cdot (1 + \omega_F(t) - \omega_M(t)) \tag{4}$$

where $\omega_M(t)$ and $\omega_F(t)$ are obtained by linear regression based on the moisture loss and oil intake results taken from [9]. The calculated coefficients are included as fraction numerators in the previous equations:

$$\omega_M(t) = \omega_{Mi} - \frac{0.0026}{60} \cdot t \tag{5}$$

$$\omega_F(t) = \omega_{Fi} + \frac{0.0019}{60} \cdot t \tag{6}$$

The initial specific heat of 2230 J/kgK is adopted [13]. However, the specific heat slightly changes during the process. Based on a previous investigation [9], moisture loss and fat uptake take place. Therefore, the change of the initial specific heat of peanuts is calculated according to Eq. (7) [13]. Specific heat of oil is only a function of oil temperature, based on the relation reported by Rahman [17] (Eq. (8)):

$$c_p(t) = c_{pi} + c_F \cdot (\omega_F(t) - \omega_{Fi}) + c_M \cdot (\omega_M(t) - \omega_{Mi}) \tag{7}$$

$$c_o(T) = 1.5951 \cdot (T_o + 273.15) + 0.0097 \cdot (T_o + 273.15)^2 \tag{8}$$

Calculation and optimization procedure

Figures 1a and 1b show the temperatures change as the result of preliminary simulation made for two different cases on an 1800 s basis, 6000 peanut kernels (7.8 kg) and 36000 peanut kernels (46.8 kg), respectively, both made for the maximum heating power of 28 kW. As seen, no significant temperature changes occur above 1200 s (which is, as mentioned, taken as the total time for the simulation). The observed difference in the initial oil temperature drop suggests some optimal solutions in terms of peanuts mass fried per "round" of frying and the used heat capacity – in other words, the bigger the mass of peanuts immersed, the larger the initial oil temperature drop will occur. Hence, greater heat power will be needed to warm the peanuts to the desired temperature in some reasonable time interval. On the other hand, a bigger mass of peanuts per "round" of frying means that fewer "rounds" will be needed to fry a similar amount of peanuts. Thus, the overall energy consumption will be reduced in that sense.

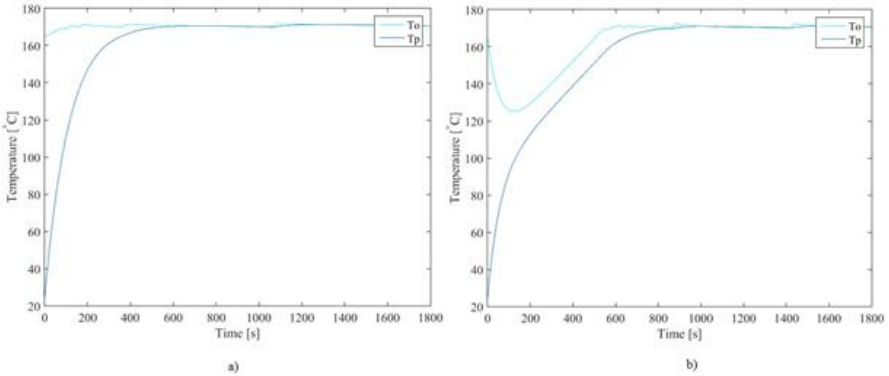

Figure 1. Preliminary model running results on an 1800 s basis with 28 kW heating power: a) 7.8 kg of peanuts (minimal mass) and b) 46.8 kg of peanuts (maximal mass).

However, not all the domain on this surface is feasible. The feasibility criterion was made under the conditions that provide high-quality products, i.e., the only feasible regimes are those in which the frying temperature is achieved at least in 10 minutes. After that, it is assumed that the frying process at around 170 °C lasts another 10 minutes. Thus, in 1 hour, three frying rounds could be obtained. In Figure 2, the simplified testing results of feasibility are shown. Only the most representative curves are displayed, i.e., the ones that express the class of feasible values or the ones that show the cases that break the feasibility criterion. Only the cases that drop in the right upper quadrant are considered feasible for usage. For instance, regimes with dark-blue, green, and red lines are feasible, and all the other cases between them are also feasible. Yellow and cyan lines represent the cases that are not suitable for such regimes and were not taken into account as they pass through the right lower quadrant.

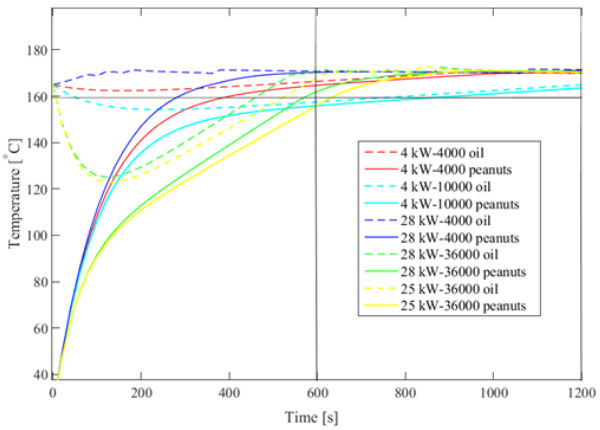

Figure 2. Representation of the feasibility assessment procedure.

Calculation procedure

The calculation was conducted by solving the system of differential Eqs. (1) and (2) via Matlab built-in solver "ode45", which utilizes the Runge-Kutta numerical method. Simultaneously, the algebraic Eqs. (3–8) were also solved for every numerical iteration step. The calculations were made for the 4–28 kW heat power range and the 6000–36000 kernel samples range (7.8 kg and 46.8 kg, respectively). The expected results are the energy consumption values per one kg of fried peanuts. Heat transfer coefficients mainly used rely on those reported by Sahin *et al.* [18]

Since the upper temperature is limited to 170°C (according to [9]), it means that the heater is turned off then the temperature exceeds the limit (the Matlab algorithm is set to make heater power Q_h = 0 in this case). The heater is turned on again when the temperature drops below the limit (the Matlab algorithm returns the current heater power Q_h value). Hence, during the observed period of 20 minutes, energy is consumed only when the heater is turned on. Following the total 60 time steps, Boolean matrix **B** is created, where zeroes are assigned to the elements that correspond to time steps where the heater was turned off, so those time steps do not contribute to the total time duration of the process. All other elements have the value "1". The Boolean matrix **B** elements were then summed to provide the total number of time steps involved in the process. Finally, this sum of "active" time steps is multiplied by the selected simulation time step of 20 seconds, which equals the ultimate time duration of the process where heat is being consumed:

$$t_{ht} = \sum_{i=1}^{60} \mathbf{B}_{1,i} \cdot \Delta t \tag{9}$$

The specific heat consumption value is then calculated as follows:

$$E = \frac{Q_h \cdot t_{ht}}{m_p} \tag{10}$$

In Table 2, the constant calculation values are summarized.

Table 2. Process parameters used for calculation.

Process parameter	Value	Unit	Source
Peanuts kernel effective diameter, d	8	mm	-
Heat transfer coefficient, h	90	W/(m^{2}K)	[17]
Oil density, ρ_o	900	kg/m^3	[7]
Peanuts density, ρ_p	617	kg/m^3	[13]
Maximum heat loss to the environment, Q_{lmax}	500	W	assumed
Total time, t	1200	s	[9]
Time step used for calculation, Δt	20	s	-
Initial oil temperature, T_{oi}	165	°C	[1], [2]
Initial peanuts temperature, T_{pi}	25	°C	assumed

Data fitting procedure

As the calculation resulted in discrete energy consumption values per one kg of fried peanuts, the calculated results were fitted by polynomial using Matlab Fitting Toolbox to obtain a functional dependence instead of discrete data.

Optimization algorithm

After the polynomial function is obtained, one can conduct an optimization procedure. For this particular

problem, the particle swarm optimization algorithm was chosen primarily because of its ability to point out an optimal domain rather than just the optimum point itself. It is achieved by selecting the large "population" number, followed by a relatively small number of iterations, so not every "individual" can achieve the optimum – but still, all the "individuals" are being closely gathered around the optimum point after the final iteration. Optimization was also run in Matlab, and the algorithm was suited following procedures described by Arora [19] and Lazzus *et al.* [20]:

1. In the first place, the initial values of i_{max}, w, φ_1, φ_2, n, x_{imin}, and x_{imax} are set;

2. Starting position of k[th] individual and velocities are calculated as:

$$x_{i,k} = x_{i,\min} + \left(x_{i,\max} - x_{i,\min}\right)u_i \quad ,k = 1\cdots n \tag{9}$$

where u_i is the random number generated between 0 and 1 (uniform distribution).

3. The fitness of the k^{th} individual is computed as:

$$p_{i,k} = f\left(x_{i,k}\right) \quad ,k = 1\cdots n \tag{10}$$

4. Since this is the initialization step, the best fitness of each individual is p_k itself. That is,

$$pbest_{i,k} = p_{i,k}$$

and global fitness is

$$g\,best_i = minimum\left(p\,best_{i,k}\right)$$

The location of $p_{best\ k}$ and gbest is given by p_{xik} and g_{ix}.

5. Starting with an initial velocity of $v_{i,k}$, the velocity of the individual is updated using the equation:

$$v_{i+1,k} = w_1 v_{i,k} + \phi_1\left(p_{xik} - x_{i,k}\right)u_i + \phi_2\left(g_{ix} - x_{i,k}\right)u_i \tag{11}$$

where w_1, ϕ_1, and ϕ_2 are the tuning factors of the algorithm.

6. The position of each individual can be updated as follows:

$$x_{i+1,k} = x_{i,k} + v_{i+1,k} \tag{12}$$

7. Based on the new position, the fitness of the k^{th} individual is computed as:

$$p_{i+1,k} = f\left(x_{i+1,k}\right) \tag{13}$$

8. If $p_{i+1,k} < p\,best_{i,k}$ then $pbest_{i+1,k} = p_{i+1,k}$, so if this fitness is lower than $pbest_{i,k}$, then $p_{best\,i,k}$ should be replaced with $p_{i+1,k}$.

9. The global best fitness is computed as

$$gbest_{i+1} = minimum\left(pbest_{i+1,k}\right) \tag{14}$$

10. The steps are repeated for a certain number of iterations. If the final iteration is not reached, the algorithm returns to step 5.

Optimization parameters are presented in Table 3.

Table 3. Particle swarm optimization parameters.

Optimization parameter	Value
Number of iterations, i_{max}	20
Weight, w	1–20 (for each iteration)
Tuning parameter 1, φ_1	1.05
Tuning parameter 2, φ_2	1.1
Population size, n	50
Lower boundary, x_{imin}	4000
Upper boundary, x_{imax}	28000

RESULTS AND DISCUSSION

Figure 3 and Figure 4 show the surface representations of the simulation results. In Figure 3, the blank surface represents the unfeasible data that were not considered, while the colored surface shows the feasible results. Figure 4 presents the unfeasible data with the dark-blue field (upper-left area of the contour diagram). These data are discrete results of numerical simulation and were subject to later data fitting, as the usage of the data alone could lead to the finding of minimum values that are exclusively valid for the shown data and wouldn't have any universal meaning. Besides that, finding a minimum discrete data array is trivial. Three values with the lowest value are shown in Figure 4 with red circles and are pointed with arrows.

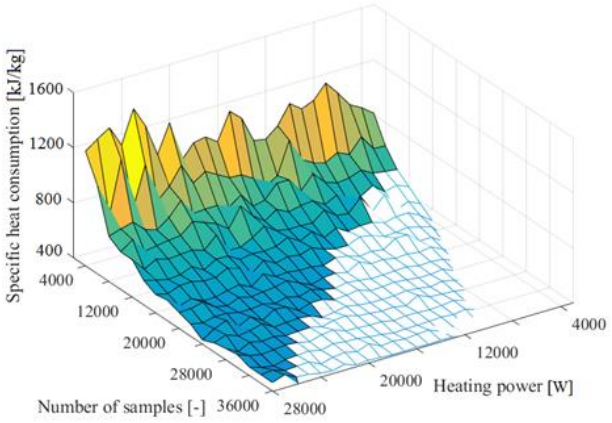

Figure 3. Main simulation results in the surface diagram with feasible (colored) and unfeasible (blank) region.

The fitted polynomial function, obtained using Matlab Fitting Toolbox, has a coefficient of determination R^2= 0.9867 and root mean square error RMSE= 29.75. This function is shown in Figure 5, together with the particle swarm optimization procedure results. Grey circles with red edges show the results of the final iteration step. The fitted polynomial function is:

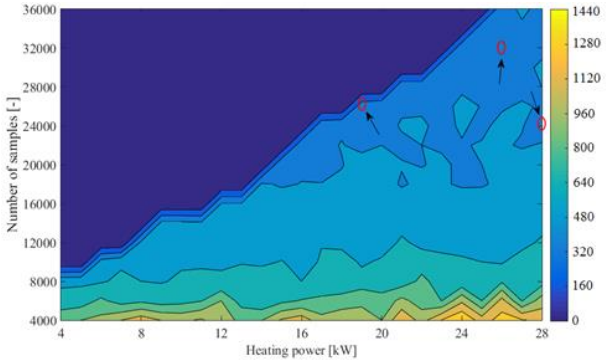

Figure 4. The main simulation results in a contour diagram with feasible (colored) and unfeasible (dark-blue) regions; red circles with arrows show the minimum values of specific energy consumption.

$$z = 1310 + 0.05349x - 0.1216y - 3.075 \cdot 10^{-6}x^2 + 3.183 \cdot 10^{-7}xy + 4.464 \cdot 10^{-6}y^2 + 6.768 \cdot 10^{-11}x^3 - 3.242 \cdot 10^{-11}x^2y + 1.91 \cdot 10^{-11}xy^2 - 6.08 \cdot 10^{-11}y^3 \quad (15)$$

The polynomial function's dependent value “z” represents the fitted specific heat consumption.

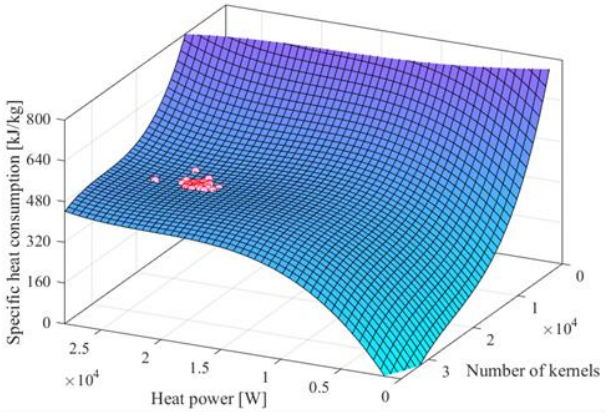

Figure 5. Optimization results on the fitted surface.

The overall analysis provided the optimal set of parameters that should be used to lower specific energy consumption as much as possible. These conclusions may provide a significant energy saving for a maximal amount of fried products per one “round” of frying. In other words, frying kinetics won’t be the same, e.g., 11 kW and 10000 kernels and 22 kW and 20000 kernels. Although the energy consumption on the same time basis would be proportional (i.e., twice as bigger for the second case), one should use a 22 kW power regime rather than an 11 kW regime twice.

The optimization results suggest that the lowest specific energy consumption appears at around 24 kW of heating power and around 22000 kernel samples (i.e., 28.6 kg of peanuts without shells). Further on, the calculated minimal specific energy consumption of around 570 kJ/kg shows a significantly lower value in comparison with the reported average energy consumption for frying nuts by Gupta [21], which is 1163 kJ/kg (500 BTU/lb as it was initially reported).

An initial temperature drop is absent for a small mass of immersed peanuts. Still, this temperature drop can increase to 40 °C for certain regimes with a high mass of material. Wu *et al.* [22] reported a temperature drop of around 20 °C while frying potato slices.

The total assumed simulation time does not significantly affect the results because the heater shuts down after reaching 170 °C. This circumstance influences the temperature profile because it practically stays uniform after approximately 800 min of a simulation run.

To assess the sensitivity of the vessel volume parameter (as the volumes of vessels usually vary in dependence on the equipment manufacturer and capacity), the simulation is repeated from the very beginning, and setting the larger volume of 0.343 m^3, while keeping all the other parameters at the same values. The simulation resulted in almost the same surface shape, having a slightly bigger energy consumption than in the case where the vessel volume is 0.125 m^3, while in some spots, two surfaces are even merging. Most important, minimum values are placed at similar spots on the surface, so the similar optimal regime parameters are valid even for different volumes. The mentioned comparison is shown in Figure 6.

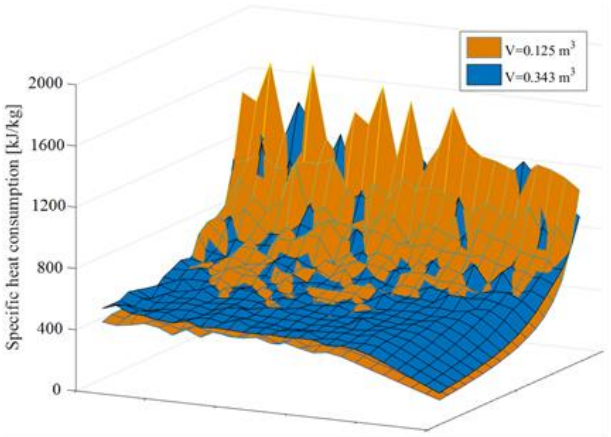

Figure 6. Comparison of resulting surfaces for two vessel volumes: blue is the basic case, while orange represents the increased volume.

CONCLUSION

Since there is a non-linear behavior of temperature functions during immersion frying, the assumption of an optimal set of process parameters for fryer power and capacity (i.e., amount of fried kernels) was valid. The presented procedure could, in a similar way, be used for other products which are subject to

immersion frying treatment. The best solution was found at around 24 kW of heating power and 28.6 kg of peanuts, resulting in approximately 570 kJ/kg of specific energy consumption. Compared with previously reported data, this regime allows twice less energy consumption. Moreover, these are only the minimum values obtained as the optimization results. Besides that, the entire resulting surface (especially the close environment of the optimal area) gives better insight into the process energy demands. It can potentially help with the improvement of the process energy consumption. Thus, the wide usage of the obtained results tends to improve overall process efficiency, which could result in certain energy savings. The variation of frying vessel dimensions resulted in no significant deviations from the first solution, while the surface curvature tendency remained practically the same.

NOMENCLATURE

A	Surface area [m^2]
c	Specific heat capacity [$kJkg^{-1}K^{-1}$]
t	Time [min]
T	Temperature [$°C$]
a,b,c,n	Constants [-]
Q	Heat flux [W]
E	Specific heat consumption [kJ/kg]
d	Diameter [m]
w	weight (refers to optimization algorithm)
n	population size (refers to optimization algorithm)
x	particle position (refers to optimization algorithm)
p	individual particle fitness (refers to optimization algorithm)
g	global fitness (refers to optimization algorithm)

Greek letters

ω	Mass fraction [%]
ρ	Density [kgm^{-3}]
h	Convection coefficient [$Wm^{-2}K^{-1}$)]
φ	tuning parameter (refers to optimization algorithm)
Δ	Increment, step [-]

Subscripts

i	initial, iteration number, matrix element
p	peanuts
o	oil
M	moisture
F	fat
ht	refers to the heating periods
v	vessel

Abbreviations

RMSE	root mean square error (statistical parameter)

REFERENCES

[1] V. Oreopoulou, M. Krokida, D. Marinos-Kouris, in Handbook of drying, A.S. Mujumdar (Ed.), CRC Press, Boca Raton, FL (2015), 1189–1208. https://doi.org/10.1201/b17208.

[2] J. Rossell, Frying: Improving quality, CRC Press, Boca Raton FL (2001). https://doi.org/10.1016/B978-1-85573-556-9.50002-X.

[3] F. Kong, M.H. Oztop, R.P. Singh, M.J. McCarthy, LWT - Food Sci. Technol. 50 (1) (2013) 32–38. https://doi.org/10.1016/j.lwt.2012.07.044.

[4] A. Alvis, C. Velez, M. Rada-Mendoza, M. Villamiel, H. S.Villada, Food Control 20 (2009) 321–325. https://doi.org/10.1016/j.foodcont.2008.05.016.

[5] M. Farid, R. Kizilel, Chem. Eng. Process. 48 (2009) 217–223. https://doi.org/10.1016/j.cep.2008.03.013.

[6] A. Ziaiifar, N. Achir, F. Curtois, I. Trezzani, G.Trystram, Int. J. Food Sci. 43 (2008) 1410–1423. https://doi.org/10.1111/j.1365-2621.2007.01664.x.

[7] S. Sahin, S.G. Sumnu, Advances in deep fat frying foods, CRC Press, Boca Raton, FL (2009). https://doi.org/10.1201/9781420055597.

[8] B.E. Farkas, R.P.Singh, T.R. Rumsey, J. Food Eng. 29 (1996) 211–226. https://doi.org/10.1016/0260-8774(95)00072-0.

[9] A. Kita, A. Figiel, Polish J. Food Nutr. Sci. 57 (4B) (2007) 285–590. http://journal.pan.olsztyn.pl/EFFECT-OF-PARAMETERS-OF-THERMAL-PROCESS-ON-THE-PROPERTIES-OF-PEANUTS,98825,0,2.html.

[10] E.K. Oke, M.A. Idowu, O.P. Sobukola, S.A.O. Adeyeye, O. Akinsola, J. Culin. Sci. Technol. 16 (2) (2018) 107–127. https://doi.org/10.1080/15428052.2017.1333936.

[11] X. Shi, J.P. Davis, Z. Xia, LWT - Food Sci. Technol. 75 (2017) 520–528. https://doi.org/10.1016/j.lwt.2016.09.030.

[12] M. Erickson, Deep Frying: Chemistry, Nutrition, and Practical Applications, 2nd ed., AOCS Press, Urbana, IL (2007). https://doi.org/10.1016/B978-1-893997-92-9.50001-3.

[13] ASHRAE, ASHRAE Handbook–Refrigeration (SI), American Society of Heating, Refrigeration and Air-Conditioning Engineers, Atlanta (2006) ISBN 1-931862-86-9.

[14] C. Tangduangdee, S. Bhumiratana, S. Tia, Int. Commun. Heat Mass Transf. 31 (1) (2004) 73–84. https://www.semanticscholar.org/paper/Heat-and-Mass-Transfer-during-Deep-Fat-Frying-of-as-Tangduangdee-Bhumiratana/56cdfa70773daa659e2f1bd386fc3cf6c4bd7644.

[15] A. Miyagi, J. Food Process. Preserv. 37 (2013) 701–708. https://doi.org/10.1111/j.1745-4549.2012.00685.x.

[16] A. Safari, R. Salamat, O-D. Baik, J. Food Eng. 230 (2018) 114–123. https://doi.org/10.1016/j.jfoodeng.2018.01.022.

[17] S. Rahman, Food Properties Handbook, CRC Press, Boca Raton, FL (1995) https://doi.org/10.1201/9781420003093.

[18] S. Sahin, S.K. Sastry, L. Bayindirli, J. Food Eng. 39 (3) (1999) 307–311. https://doi.org/10.1016/S0260-8774(98)00171-X.

[19] R. Arora, Optimization Algorithms and Applications: CRC Press, Boca Raton, FL (2015) https://doi.org/10.1201/b18469.

[20] J.A. Lazzus, M. Rivera, I. Salfate, G. Pulgar-Villarroel, P. Rojas, J. Eng. Thermophys. 25 (2) (2016) 216–226. https://doi.org/10.1134/S1810232816020065.

[21] M. Gupta, in Advances in Deep-Fat Frying of Foods, S. Sahin, S.G. Sumnu (Eds.), CRC Press, Boca Raton, FL (2009), pp. 263–286. https://doi.org/10.1201/9781420055597.

[22] H. Wu, H. Jouhara, S.A. Tassou, Appl. Therm. Eng. 51 (2013) 926–936. https://doi.org/10.1016/j.applthermaleng.2012.10.002.

ĐORĐIJE DODER
DAMIR ĐAKOVIĆ
BORIVOJ STEPANOV
NIKOLA MILIVOJEVIĆ

Univerzitet u Novom Sadu, Fakultet tehničkih nauka, Departman za energetiku i procesnu tehniku, Novi Sad, Srbija

NAUČNI RAD

OPTIMIZACIJA POTROŠNJE ENERGIJE PRI POTAPAJUĆEM PRŽENJU KIKIRIKIJA

Cilj ovog istraživanja bio je da se ispita uticaj različitih režima potapajućeg šaržnog prženja kikirikija na specifičnu potrošnju energije u procesu. Istraživanje je sprovedeno putem simulacije, gde je potrošnja energije izračunata korišćenjem različitih odnosa toplotne snage i mase kikirikija. Kao rezultat primenjenog postupka optimizacije u okviru ispitivanog domena i proračunskih podataka, procenjeno je da režim sa 24 kW grejne snage i 28,6 kg kikirikija daje minimalnu specifičnu potrošnju energije. Osim toga, dobijena površina bi mogla da posluži kao osnova, kako za projektovanje, tako i za rad uređaja za prženje u povoljnijim režimima u pogledu energetske efikasnosti.

Ključne reči: prženje potapanjem, prženje kikirikija, optimizacija potrošnje energije.

CI&CEQ
Chemical Industry & Chemical Engineering Quarterly

Available online at
Association of the Chemical Engineers of Serbia AChE
www.ache.org.rs/CICEQ

Chem. Ind. Chem. Eng. Q. 30 (2) 143–149 (2024) CI&CEQ

AYSU KAYALIOĞLU

Toros Agri Industry and Trade R&D Center, Mersin, Turkey

ECO-FRIENDLY COATINGS COMPOSED OF LIGNOSULFONATE-MODIFIED BIOPOLYMER AND VEGETABLE WAXES FOR NITROGENOUS FERTILIZERS

Article Highlights

- Biopolymer and vegetable oil coatings are strong alternatives to paraffinic fertilizer coatings
- Biopolymers perform better anti-caking effects than petroleum derivative coatings
- Vegetable coatings showed a significant moisture-repellent behavior
- The polymeric coatings showed high efficiency in both mechanical strength and hydrophobicity

Abstract

Fertilizer coatings are considered mandatory to protect the physical quality of fertilizer granules. They continue to be developed due to compliance with novel fertilizer types and, most importantly, future environmental and animal-plant health regulations. As known, bio-based contents are sustainable and eco-friendly compared to petroleum-based materials. However, many types of coatings are commonly composed of unsustainable, costly, and can be ecologically toxic, such as paraffin or mineral oil. This article presents a comparative research study to provide eco-friendly anticaking coatings composed of lignosulfonate-modified biopolymer and vegetable waxes instead of conventional coatings. This research mainly aims to find alternative ingredients instead of a petroleum-derivatives in conventional coatings. According to the results, an anticaking coating containing lignosulfonate-modified biopolymer improved the granule structure of calcium ammonium nitrate fertilizer. It showed the best anticaking performance compared to other coating types. Vegetable-based coatings, on the other hand, gave results in appropriate intervals, especially at low concentrations, and showed a valuable way to develop better versions in future studies. As a result, it is seen that biopolymers can replace paraffin-based products.

Keywords: anticaking coatings, caking, bio-based coatings, crushing strength, moisture absorption.

SCIENTIFIC PAPER

UDC 631.84:66:502/504

The fertilizer industry depends on agriculture and has seasonal sales; therefore, the products are shipped in large quantities and stored for long storage times. It is quite possible to encounter quality problems such as degradation, dusting, water uptake, and, accordingly, caking in fertilizers due to the exposed harsh climatic conditions and intense handling. The caking tendency of fertilizer is mainly caused by its characteristics such as moisture absorption capacity, crushing strength, and abrasion resistance and is related to its chemical structure. In addition, it is strongly triggered by environmental conditions where it is stored, such as temperature, humidity, and pressure [1]. Caking proceeds with the phase change and the adhesion mechanisms between contact points of fertilizer granules that show substantial caking with increasing temperature, humidity, pressure, and handling. The application of a suitable anti-caking agent controls these parameters, and the tendency to cake remains

Correspondence: A. Kayalıoğlu, Toros Agri Industry and Trade R&D Center, Mersin, Turkey.
E-mail: aysu.kayalioglu@toros.com.tr
Paper received: 14 February, 2023
Paper revised: 1 June, 2023
Paper accepted: 25 July, 2023

https://doi.org/10.2298/CICEQ230214019K

significantly low. Consequently, chemical agents are used to minimize that caking phenomenon. External chemical agents are applied as a coating which is important to improve a hydrophobic surface against high humidity conditions, and a film layer to provide mechanical strength on fertilizer granules [2].

The most common coating agents are paraffin oil-based. Mineral oils of high paraffin content can be considered particularly more effective. Purified paraffin-based oils are distinguished from aromatic oils because they biodegrade, albeit slowly, and are not directly toxic [3]. Traditional paraffin-based coatings usually comprise various ratios of alkylamines, petroleum-based oils, fatty acids, paraffins, or waxes combined with an inert powder. All of these ingredients are strongly hydrophobic molecules. However, the use of heavy oils such as fuel oil is carcinogenic because it contains PAHs above the restrictions, and it is prohibited by regulations in many countries [4–5]. For this reason, paraffinic oils, which are a controversial issue and banned in and around the EU, are substances that may be prohibited around the whole world by future environmental regulations. Therefore, there is a need for research on sustainable alternative products [6–7]. In addition, many anti-caking materials contain fatty amines coated on the fertilizer granule within paraffin or mineral oil solvents and act as surfactants [4]. Instead of amine derivatives, lignin derivatives and vegetable fatty acid (e.g., coconut fatty acid, lauric acid) ingredients that work as surfactants to increase the hydrophobic effect are also being investigated. Moreover, lignin, the second largest biomass resource on earth, can be a sustainable and non-toxic feedstock for fertilizer coating [8].

Today, the fertilizer agents' biodegradability has become an important parameter. The use of products with the potential to create toxic effects in fertilizers is dangerous for human health and creates soil contamination. These products can be expected to be removed from the shelf in the next few years [9]. Eco-friendly coatings that are alternative to traditional coatings should have an ecologically non-toxic oil base instead of mineral oil or paraffin base, application concentrations should have a reasonable and economical price, and the granular healing performance should be at a level that can compete with commercial size paraffin-based coatings [10]. In recent years, studies have been carried out on vegetable oils as oil derivatives, biodegradable polymers, and natural by-products of vegetable oils [8, 11–12]. Vegetable oils do not contain branched and cyclic alkanes, i.e., PAHs, like mineral oils. For this reason, it draws attention to its non-toxicity and eco-friendly nature. Although it has hydrophobic solid structures, it may lag in terms of performance in a moisture absorption test compared to paraffinic oils [13–15].

Developing inhibitory mechanisms to comply with the green consensus process is essential to contribute to sustainable agricultural management due to both greenhouse gas production and ecological transformation for the fertilizer production industry and the use of produced fertilizers in agricultural areas. In this respect, there are initiatives by developed countries to develop models for sustainable development goals (SDG) within the scope of the green agreement on a global scale. Thus, models supporting the inhibitory mechanism, such as biopolymer, can be considered an important alternative to the manufacturer in the green accord compliance process.

The presented research study explains conventional amine-containing paraffin, amine-free paraffinic, biodegradable polymer, and vegetable oil-based coatings. It provides information on the possibility of replacing amine-derived coatings with plant-natural products and biodegradable polymers, which are defined as sustainable and eco-friendly in terms of their resources and following limitations from the environmental point of view. Three concentrations of each coating were tried on CAN/26 fertilizer to determine the optimum dosage for the desired coating. The coatings' performance on the fertilizer's physical properties could be compared. For CAN/26, the best coating type and ratio will be seen for different features.

MATERIALS AND METHODS

Experimental

In this study, five different commercially available coatings were applied to CAN/26 fertilizer. The coating process was applied in three different concentrations between commercially recommended minimum and maximum dosages of coating agents. The main ingredients and application rates of coating agents are given in Table 1.

All fertilizer samples were produced in Toros Agri Ind., and the research was conducted in Toros R&D Center.

The unique prill form and the diameter between 2 and 4 mm were selected for the experiments. The fertilizer granules were heated to 60 °C, and anti-caking agents were injected at around 80 °C on fertilizer. Finally, fertilizer samples were coated in a manually rotated plastic chamber, and final products were evaluated in terms of crushing strength, moisture uptake capacity, critical relative humidity value, and caking tendency by comparing with uncoated CAN/26 and CAN/26 coated with conventional coatings which

Table 1. The main ingredients and dosages of coating agents.

Fertilizer coatings	Type	Dosage	Surfactant
A	Biopolymer	500-1000-2000 ppm	Sodium Lignosulfonate in biopolymer
B	Paraffinic	500-1000-3000 ppm	Amine-free fatty acids in paraffinic oil.
C	Vegetable	500-2000-3000 ppm	Plant-based fatty acids in vegetable oil.
D	Vegetable	500-2000-3000 ppm	Plant-based natural polymers in water.
R (Reference)	Paraffinic	500 ppm	Amines in paraffinic oil.
E	Petroleum-based	<1000 ppm	3-10% Alkylamine + 2.5-10% Organic P-compounds

have paraffines and alkyl amines. With this aim, crushing strength, moisture absorption, and accelerating caking tests were done. All tests based on granules were run in at least ten parallels, while the other tests were run in 3.

Crushing strength analysis

Crushing strength (CS, kg/granule) is the maximum load at which 2 mm fertilizer granule can sustain. It was measured with universal test equipment by applying a compression pressure on one granule until it collapsed [16]. In this study, a crushing strength testing machine, Lutron FG-5000A, was used. Average crushing strength values were determined by testing ten granules for each fertilizer sample.

Moisture absorption test

Moisture absorption test (MA, wt.%) was performed in a JSR JSPC-200C model climate-controlled chamber by exposing fertilizer samples to a specific humidity range at a constant temperature. In this study, around 30 g of fertilizer samples were loaded in the cylindrical volumetric vessels, and the samples were kept at 25 °C and 40, 50, 60, and 70% humidity values each for 3 hours [17].

It was calculated as the moisture uptake capacity from the highest amount of moisture the fertilizers can hold. In addition, the relative atmospheric humidity value at which the fertilizers tested at a constant temperature increasing humidity value first started to retain moisture was determined as the critical relative humidity value of that fertilizer.

Accelerating caking test

An accelerated caking test is a procedure to evaluate the caking tendency of fertilizer over time by simulating storage conditions. To simulate the conditions of storage, transportation, and handling of fertilizers, the samples were exposed to a climatic cycle in the climatic chamber. In this study, fertilizer samples, which were prepared in polyethylene sample bags for the accelerated caking test, were kept in a JSR JSPC-200C model climate-controlled chamber for 32 h at 32 °C and 80% relative humidity conditions and then three days under the conditions, 40 °C and 20% relative humidity [18]. After climatic conditioning, the fertilizers were stored under a pressure of 0.28 kg/cm^2 for three days in a conventional small bag storage test, as shown in Figure 1. In the small bag storage test, dummy weights were used to apply a pressure of 0.28 kg/cm^2 on the surface of the lowest fertilizer bag. This test represented a situation where fertilizer was stored in bags at a standard suitable pressure which is a standard suitable pressure to keep fertilizer in good quality. After the test, caking tendencies were calculated by measuring the caking parts in the fertilizers.

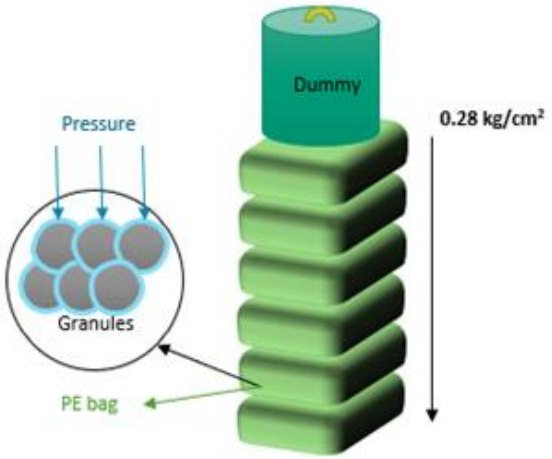

Figure 1. Small-bag storage test scheme.

RESULTS AND DISCUSSION

The crushing strength results of prepared fertilizer samples with various types of coatings at different dosages are given in Table 2. A crushing strength test was employed to determine the effect of coating type, coating ratio, and climatic cycle on the crushing strength of CAN/26.

According to the results, the uncoated fertilizer sample has the weakest granules, probably due to any coating providing a thin film cover on the granules against mechanical interactions and handling. In general, the crushing strength of fertilizer granules is

Table 2. Crushing strength test results for fertilizer samples.

Coating	Dosage (ppm)	CS (kg/granule)	CS after climatic cycle (kg/granule)
Uncoated	-	1.72	1.55
	500	2.24	1.77
A	1000	2.39	2.35
	2000	2.50	2.03
	500	2.46	1.96
B	1000	2.29	1.84
	3000	2.19	2.15
	500	2.46	2.16
C	2000	2.30	1.98
	3000	2.48	1.79
	500	2.43	1.93
D	2000	2.38	2.06
	3000	2.59	2.39
R	500	2.60	1.95
E	<1000	1.41<CS<2.70	<2.40

expected to be at least 2 kg/granule [3]. However, after the climatic cycle test, some fertilizer samples showed less than 2 kg/granule crushing strength, which is probably due to the low moisture resistance of their coating. Thus, although all coatings provided mechanical film protection, the protection of most of the coating decreased by about 10-20% when exposed to moisture and temperature.

After the climatic cycle, it can be said that the coatings are compatible with good performance for the fertilizer samples that still have a crushing strength of more than 2 kg/granule. The fertilizer sample coated with 1000 ppm of biopolymer coating-A shows 2.35 kg/granule crushing strength after the climatic cycle, probably due to the intermolecular forces such as van der Waals among the polymeric chains [12]. The presence of long-chain polymers in the coating enhances the adhesion of the coating on the fertilizer surface by increasing a polymer-salt interaction by forming a hydrogen bonding network [19–20]. The fertilizer coated with 3000 ppm of amine-free paraffinic coating-B shows a competitive crushing strength of 2.15 kg/granule, while the fertilizer coated with 500 ppm reference coating, which contains amine and paraffines, has 1.95 kg/granule after the climatic cycle. Since it does not contain amines which are moisture-repellent supportive compounds, its performance was good at a higher coating rate. Both coatings (B & R) have paraffins, which are hydrophobic mixtures of linear and branched alkanes with a carbon number of 20–40 that show moisture-repellent properties. Petroleum waxes contain mostly branched alkanes with a carbon number of 30–80, and most anticaking agents are paraffin-based, requiring highly branched alkanes [21]. However, although it was effective, B-coating may not be economically interpreted as a 3000 ppm dosage.

According to the complete vegetable coating materials, 500 ppm of coating-C and 2000–3000 ppm of coating-D have good results for crushing strength, such as 2.16, 2.06, and 2.39 kg/granule, respectively. Compared with paraffinic and biopolymeric coatings, the durability of vegetal-based coatings is competitive, probably due to vegetable coatings having branched chains that enhance coating-fertilizer surface adhesion. Vegetable oils contain glycerol trailers from C12–C24 fatty acids, and several double bonds are susceptible to crosslinking or polymerization reactions [22]. Basically, the function of a coating is to cover the granule with a protective film layer in order to avoid interactions between granules [23]. Therefore, it can be pointed out that the compatibility between coating and fertilizer surface enhances granules' mechanical resistance and gives relatively higher crushing strength.

Moisture absorption and CRH results of prepared fertilizer samples with various types of coatings at different dosages are given in Table 3. Moisture absorption tests of CAN/26 were carried out to understand the interaction of fertilizers with moisture and to evaluate the effect of coating type and coating ratio on this situation.

Table 3 shows that biopolymer-coated fertilizers kept above the critical humidity value (at 70% RH) retained a maximum moisture content of 1.39-1.41%. A 1.58% moisture uptake was observed in the fertilizer to

Table 3. Moisture uptake and CRH values for fertilizer samples.

Coating	Dosage (ppm)	Moisture uptake% @70 RH	CRH @25 °C
Uncoated	-	2.40%	60%
A	500	1.39%	58%
	1000	1.40%	58%
	2000	1.41%	58%
B	500	6.29%	58%
	1000	1.38%	58%
	3000	1.31%	58%
C	500	1.46%	60%
	2000	1.37%	58%
	3000	2.95%	52%
D	500	1.42%	58%
	2000	1.59%	52%
	3000	2.67%	52%
R	500	1.58%	60%
E	<1000	0,7%	60%

which the reference coating was applied. All concentrations of the biopolymer coating-A showed better moisture repellency than the reference paraffin coating. It can be due to the good adhesion of polymeric coatings on the fertilizer surface with crosslinking reactions and the lignin-based moisture-repellent components, which have the potential for use in anticaking agents for fertilizer due to hydrophobicity, bonding ability, and film formation capability [24]. On the other hand, it has been observed that the amine-free paraffin coating performs better than the amine-containing coating. It shows that some fatty acid derivatives, such as coconut and lauric acids, which have a very high moisture-repellent function, can replace amine contents. Vegetable coatings' moisture-repellency performance was found to be good at most dosages. Due to the hydrophobic nature of the high content of vegetable fatty acids, vegetable oils showed a significant hydrophobic effect [25–26]. Table 4 shows accelerating test results of prepared fertilizer samples to determine the effect of the coating type and coating concentration on free-flowing fertilizer.

Biopolymer coatings cover the surface in a way that does not allow the passage of air molecules on the particle surface due to its surface wetting or surface tension-increasing properties. In addition, the film layer formed on the fertilizer surface is more advantageous than other organic coating chemicals due to the cross-linking feature of biopolymers, that moisture molecules reach the fertilizer surface. Because the effect of the cross-link structure to slow down moisture diffusion has also been reported in the literature [27]. Considering the results of the accelerated caking test, fertilizer samples were coated with 500 ppm of amine-free paraffinic coating-B, 500 ppm of vegetable coating-C, and all concentrations of biopolymer-containing coating-A

Table 4. Accelerating test results of prepared fertilizer samples.

Coating	Dosage (ppm)	Caking(%)
Uncoated	-	34.70
A	500	2.52
	1000	2.40
	2000	3.00
B	500	3.63
	1000	15.00
	3000	13.72
C	500	7.71
	2000	21.17
	3000	31.58
D	500	23.10
	2000	49.75
	3000	44.58
R	500	3.14
E	<1000	<5

were found to be in proper free-flowing. It has been determined that the biopolymer coating performs better than other coatings in reducing the tendency to caking. Even after the climatic cycle, the granule quality is within appropriate intervals, and the tendency to cake is below 3%. It is because polymer coatings and lignin-based surfactants enhance the resistance to crushing and moisture absorption [11,26]. When amine-containing and non-amine-containing paraffin coatings were compared, the caking tendencies of the 500 ppm applied fertilizers were around 3% and close to each other. Many anti-caking materials contain fatty amines that cause the displacement of ammonia by reacting with ammonium salts in the nitrogenous fertilizer, which ensures a good coating adhesion. It has been observed that crystals form on the surface of fertilizer coated with

fatty amine when subjected to high humidity cycles. These crystals may spill from the surface and cause dust formation in the future. Although similar anticaking performance has been obtained, it has been reported that dust formation can occur on the surface, especially in ammonium nitrate fertilizers, in amine-containing coatings, but this dusting risk does not exist in coatings containing fatty acids that do not contain amines [28]. When the anticaking performance of the coatings produced entirely with vegetable ingredients was evaluated, it was seen that the low-concentration coatings of 500 ppm vegetable-based products performed slightly better. Vegetable coating-C was more effective on caking tendency than coating-D. Since the vegetable D-coating is water-based, it has been determined that it penetrates and easily dissolves the fertilizer structure at high concentrations and causes caking.

CONCLUSION

In this study, three coating amounts were tried for each coating material in CAN/26 fertilizer, and optimum concentrations were determined. For different properties of CAN/26, the best coating type and ratio was determined as 1000 ppm biopolymer coating ratio. When the physical strength properties of CAN/26 fertilizers prepared with different coatings were compared, the highest tensile strength was obtained in vegetal-containing coatings; however, the agglomeration tendency was observed to increase at high concentrations of these coatings. It was determined that the critical humidity value of CAN/26 for coating types decreased. However, uncoated CAN/26 fertilizer can hold up to 2.4% of its weight when moisture retention is taken into account; In coated fertilizers, this ratio has generally decreased below 1.5%. The coating type and ratio with the best moisture repellency can be listed as 1000 and 1200 ppm amine-free paraffinic coating and 1000 ppm biopolymer coating. It has been observed that the vegetal-containing coatings show higher performance in terms of agglomeration and moisture repellency, especially in low-concentration applications such as 500 ppm for CAN/26 fertilizer. The 500 ppm concentration of the oil-based vegetable coating showed an anti-caking performance of about 7%. Finally, a comparison with petroleum-based formulas would be an excellent addition.

REFERENCES

[1] A. Ulusal, C. Avsar, Chem. Biochem. Eng. Q. 34 (2020) 209–222. https://doi.org/10.15255/CABEQ.2020.1866.

[2] A. Tyc, D. Nieweś, S. Penkala, R. Grzesik, K. Hoffmann, J. Hoffmann, Coatings 10 (2020) 1–10. https://doi.org/10.3390/coatings10111093.

[3] T.P. Hignett, Fertilizer Manual, Vol. 15, Alabama, Springer Sci. & Business Media BV; (2013).

[4] J.A.R. Martinez, M.M. Blanch MM. Patent No. ES2922301T3 (Accessed 13 Sep 2022).

[5] A.T. Lawal, Cogent Environ. Sci. 3 (2017) 1–89. https://doi.org/10.1080/23311843.2017.1339841.

[6] S. Zhang, T. Shen T, Y. Yang, X. Ma, B. Gao, Y.C. Li, P. Wang, Progr. Org. Coat. 151 (2021) 106018. https://doi.org/10.1016/j.porgcoat.2020.106018.

[7] K. Heister, A.T. Lima, Environ. Monit. Assess. 191 (2019) 1. https://doi.org/10.1007/s10661-019-7776-6.

[8] Y. Chen, W. Li, S. Zhang, Progr. Org. Coat. 154 (2021) 106158. https://doi.org/10.1016/j.porgcoat.2021.106158.

[9] Official website of the European Union URL:http://ec.europa.eu/science-environment-policy. (Accessed December 29, 2022).

[10] L.R. Moore, World Fertilizers. Mag. (July/August 2020). https://fertiliser-society.org/wp-content/uploads/2021/04/Measuring-the-Sustainability-of-Fertilizer-Coatings-World-Fertilizer-JulAug-2020.pdf.

[11] A. El Gharrak, Y. Essamlali, O. Amadine, S. Aboulhrouz, A. Hafnaoui, H. Ghalfi, M. Zahouily, Progr. Org. Coat. 170 (2022) 106982. https://doi.org/10.1016/j.porgcoat.2022.106982.

[12] T. El Assimi, O. Lakbita, A. El Meziane, M. Khouloud, A. Dahchour, R. Beniazza, R. Boulif, M. Raihane, M. Lahcini, Int. J. Biol. Macromol. 161 (2020) 492–502. https://doi.org/10.1016/j.ijbiomac.2020.06.074.

[13] I. Kassem, E.H. Ablouh, F.Z. El Bouchtaoui, Z. Kassab, H. Hannache, H. Sehaqui, M. El Achaby, Progr. Org. Coat. 162 (2022) 106575. https://doi.org/10.1016/j.porgcoat.2021.106575.

[14] C. Wang, S. Song, Z. Yang, Y. Liu, Z. He, C. Zhou, L. Du, D. Sun, P. Li. Progr. Org. Coat. 165 (2022) 106756. https://doi.org/10.1016/j.porgcoat.2022.106756.

[15] G. Karmakar, P. Ghosh, B.K. Sharma, Lubricants. 5 (2017) 1–17. https://doi.org/10.3390/lubricants5040044.

[16] A.O. Gezerman, Heliyon 6 (2020) 1–9 https://doi.org/10.1016/j.heliyon.2020.e03628.

[17] M.C. Paré, S.E. Allaire, L. Khiari, C. Nduwamungu, Canad. Biopsy. Engin. 51 (2009) 1–7.

[18] J.A.R. Martinez JAR, Fajardo MR. U.S. Patent No. 8932490 (13 January 2015).

[19] M. Lavorgna, F. Piscitelli, P. Mangiacapra, G.G. Buonocore, Carbohydr. Polym. 82 (2010) 291–298. https://doi.org/10.1016/j.carbpol.2010.04.054.

[20] A. Giannakas, K. Grigoriadi, A. Leontiou, N.M. Barkoula, A. Ladavos, Carbohydr. Polym. 108 (2014) 103–111. https://doi.org/10.1016/j.carbpol.2014.03.019.

[21] M. Guzmann, Y. Liu, R. Konrad, D. Franz, U.S. Patent No 20100130385A1 (27 May 2010).

[22] G. Lligadas, J.C. Ronda, M. Galia, V. Cadiz, Mater. Today Commun. 16 (2013) 337–343. https://doi.org/10.1016/j.mattod.2013.08.016.

[23] D. Lawrencia, S.K. Wong, D.Y.S. Low, B.H. Goh, J.K. Goh, U.R. Ruktanonchai, A. Soottitantawat, L.H. Lee, S.Y. Tang, Plants 10 (2021) 1–25.

https://doi.org/10.3390/plants10020238.

[24] W. Quan, L. Zhang, J. Chen, Z. Tong, X. Zhou, L. Shao, Z. Wu, P. Zhan, F. Wang, N. Liu, H. Lin, H. Dong, Polym. Test. 102 (2021) 107335. https://doi.org/10.1016/j.polymertesting.2021.107335.

[25] S. Yuan, L. Cheng, Z. Tan, J. Controlled Release 345 (2022) 675–684. https://doi.org/10.1016/j.jconrel.2022.03.040.

[26] A. Abbas, Z. Wang, Y. Zhang, P. Peng, D. She, Int. J. Biol. Macromol. 222 (2022) 1801–1817. https://doi.org/10.1016/j.ijbiomac.2022.09.265.

[27] S. Durpekova, A. Di Martino, M. Dusankova, P. Drohsler, V. Sedlarik, Polymers, 13 (2021), 3274. https://doi.org/10.3390/polym13193274.

[28] A.O. Gezerman, B.D. Çorbacıoğlu, Chem. Ind. Chem. Eng. Q. 21 (2015) 359–367. https://doi.org/10.2298/CICEQ140705038G.

AYSU KAYALIOĞLU

Toros Agri Industry and Trade R&D Center, Mersin, Turkey

EKOLOŠKI PREMAZI ZA AZOTNA ĐUBRIVA OD LIGNOSULFONATOM MODIFIKOVANOG BIOPOLIMERA I BILJNIH VOSKOVA

Premazi za đubriva se smatraju obaveznim za zaštitu fizičkog kvaliteta granula đubriva. Ona nastavljaju da se razvijaju zbog usklađenosti sa novim tipovima đubriva i, što je najvažnije, budućim propisima o zaštiti životne sredine i zdravlja životinja i biljaka. Kao što je poznato, sadržaji na bazi bioloških materijala su održivi i ekološki prihvatljivi u poređenju sa materijalima na bazi nafte. Međutim, mnoge vrste premaza se obično sastoje od neodrživih, skupih i često ekološki toksičnih, kao što su parafin ili mineralno ulje. Ovaj članak predstavlja rezultate istraživanja ekološki prihvatljivih premaza protiv zgrušavanja koji se sastoje od biopolimera modifikovanog lignosulfonatom i biljnih voskova umesto konvencionalnih premaza. Ovo istraživanje uglavnom ima za cilj pronalaženje alternativnih sastojaka umesto derivata nafte u konvencionalnim premazima. Prema rezultatima, premaz protiv zgrušavanja koji sadrži biopolimer modifikovan lignosulfonatom poboljšao je strukturu granula đubriva kalcijum-amonijum-nitrata. Pokazao je najbolje performanse protiv zgrušavanja u poređenju sa drugim tipovima premaza. Premazi na bazi povrća su, s druge strane, dali rezultate u odgovarajućim intervalima, posebno pri niskim koncentracijama, i pokazali vredan način za razvoj boljih verzija u budućim istraživanjima. Jasno je da biopolimeri mogu zameniti proizvode na bazi parafina.

NAUČNI RAD

Ključne reči: premazi protiv zgrušavanja, zgrušavanje, premazi na biološkoj bazi, čvrstoća na drobljenje, apsorpcija vlage.

CI&CEQ
Chemical Industry & Chemical Engineering Quarterly

Available online at
Association of the Chemical Engineers of Serbia AChE
www.ache.org.rs/CICEQ

Chem. Ind. Chem. Eng. Q. 30 (2) 151–159 (2024) CI&CEQ

JASIM I. HUMADI[1]
MUAYAD A. SHIHAB[1]
GHAZWAN S. AHMED[2]
MUSTAFA A. AHMED[3]
ZEYAD A. ABDULLAH[4]
SHANKAR SEHGAL[5]

[1]Department of Petroleum and Gas Refining Engineering, College of Petroleum Processes Engineering, Tikrit University, Slah Al-deen, Iraq

[2]Chemical Engineering Department, College of Engineering, Tikrit University, Iraq

[3]Ministry of Oil, North Refineries Company, Baiji Refinery, Slah Al-deen, Iraq

[4]The State Company for Drugs Industry and Medical Appliances, Slah Al-deen, Iraq

[5]Mechanical Engineering, UIET, Panjab University, Chandigarh, India

SCIENTIFIC PAPER

UDC 546.22:546.47-31:662.756.3

PROCESS MODELING AND KINETIC ESTIMATION FOR DESULFURIZATION OF DIESEL FUEL USING NANO - ZnO/Al_2O_3

Article Highlights

- Nano ZnO/γ-Al_2O_3 was synthesized, characterized, and used for the desulfurization of diesel fuel
- The process was conducted in a batch reactor at 30 to 90 °C and 20 to 80 min
- Sulfur removal was 93.781% using 9% ZnO/γ-Al_2O_3 at 90°C and 80 min
- Process modeling and kinetic estimation for desulfurization were investigated
- Simulation results indicate less than 5% error between experimental and predicted results

Abstract

In the present paper, a gamma alumina (γ-Al_2O_3) loaded zinc oxide (ZnO) nano-catalyst (ZnO/γ-Al_2O_3) has been synthesized and used to accelerate the removal of sulfur compounds from light gas oil by oxidative desulfurization (ODS) process. The synthesized nano-catalysts have been characterized by atomic force microscopy (AFM) and Brunauer-Emmett-Teller (BET). The ODS process has been conducted in a batch reactor at various reaction temperatures and batch times varying between 30 to 90 °C and 20 to 80 min, respectively. DBT removal was highest (93.781%) while using synthesized nano-catalyst (9% ZnO/γ-Al_2O_3) at 90°C and 80 min reaction time. Based on the obtained experimental data, a new mathematical modeling technique was performed for the ODS operation under mild experimental conditions to evaluate the most appropriate kinetic variables for the newly synthesized nano-catalysts. Simulation results indicate a good match with experimental observations with less than 5% absolute average error for all runs. The optimization procedure of the process condition displays that > 98% DBT could be eliminated within 200 min, at 87 °C, in the existence of synthesized nano-catalyst (9% ZnO/γ-Al_2O_3).

Keywords: gamma alumina; model; nano-catalyst; optimization; sulfur; zinc oxide.

Recently, the produced hydrocarbon feedstock has contained a high amount of sulfur compounds, negatively influencing the refining operations and the quality of the resulting fuels. Sulfur oxides (SO_2) emitted while burning fuels have an adverse effect on human health and the environment and lead to acid rain and corrosion [1–3]. In this regard, strict environmental regulations have been applied in many countries limiting the sulfur concentration in light fuels to 10 ppm. Since the rise in sulfur compounds level in oils causes an increase in the hydrodesulfurization (HDS) cost, the concern of researchers has been growingly attracted by non-hydrogen desulfurization techniques [4,5]. Oxidative desulfurization (ODS) is the most advantageous and promising technique among the non - hydrogen desulfurization techniques (bio

Correspondence: J.I. Humadi, Department of Petroleum and Gas Refining Engineering, College of Petroleum Processes Engineering, Tikrit University, Slah Al-deen, Iraq.
E-mail: jasim_alhashimi_ppe@tu.edu.iq
Paper received: 8 February, 2023
Paper revised: 17 July, 2023
Paper accepted: 31 July, 2023

https://doi.org/10.2298/CICEQ230208020H

desulfurization, adsorption, extraction) [5–7]. The major features of ODS are lower pressures and temperatures and the absence of hydrogen [8,9]. Another feature of ODS is the ability to eliminate organic sulfur compounds not cracked in the process of HDS [5]. Organic sulfur compounds are treated with an oxidizing agent and a catalyst to oxidize first to their corresponding sulfoxides and then to their sulfones, which are more polar compounds, and then these oxidized sulfur compounds are separated from the fuel by employing an extraction technique with a polar extractant such as dimethyl formamide, acetonitrile, methanol, etc. or by utilizing adsorption technique [10]. Mathematical modeling is the description of a system by employing mathematical equations. It is significant to capture the fundamental characteristics of a system to design (describe), predict (forecast), optimize the operating conditions, and design an appropriate controller. Some utilizing areas of mathematical modeling are operation control, process design, operations training simulators, process safety, environmental effect assessment, etc. Each field of application may need various systems of mathematical model equations. Mathematical modeling includes analysis, numerical simulation, and experimental tests [11]. The optimization process is utilized in several fields to determine solutions of studies that minimize or maximize some interesting parameters, like maximizing profits, lowering costs in the production of a good or service, enhancing production, or reducing raw materials [12]. Nanostructures (size of particle less than 100 nm) have been recently utilized in catalytic processes. Nano-catalysts applied in this technique are environmentally friendly, lower cost, and have good mechanical strength. Also, nanostructured materials have significant porosity, purities, chemical and thermal stability, and density tunable. In addition, nano-catalysts have significant recyclability in the oxidative desulfurization technology [13]. Developing a new nanocatalyst with remarkable properties that enhances its activity towards the high efficiency of the ODS process for fuel is an interesting goal in the industrial and academic fields. Also, finding a mathematical model that evaluates the optimal kinetic variables of the oxidation process in the presence of the newly synthesized nano-catalysts is the main matter in improving, designing, and scaling up the ODS for the industrial fields. Two reported works in the literature studied oxidative desulfurization of fuel in the presence of heterogeneous catalysts composed of gamma-alumina (γ-Al_2O_3) as support and ZnO as active metal. Nawaf *et al.* [14] investigated the removal of sulfur compounds in kerosene by employing (18% ZnO / γ-Al_2O_3) as a catalyst and air as an oxidizing agent in a batch reactor. It was found that 70.5% of sulfur compounds were removed under a reaction time of 50 min and a reaction temperature of 190 °C. Abdulateef *et al.* [15] investigated the oxidative desulfurizing experimentally by utilizing (12.5% ZnO-12.5% MgO)/γ-Al_2O_3 as a catalyst, where sulfur conversion of 84.6% was achieved under reaction time of 45 min and reaction temperature of 190°C employing a batch mode reaction.

In this study, a new mathematical model has been built, validated, and optimized for ODS technology to evaluate the optimal kinetic variables in the presence of the newly synthesized nano-catalysts based on the obtained results of the oxidation experiments at mild operating conditions. Finally, the evaluated kinetic parameters will be utilized to estimate the optimal ODS operating condition, maximize the sweetening of diesel fuel, and produce cleaner fuel.

MATERIALS AND METHODS

Diesel fuel produced by OMV Company (Pendik-Istanbul-Turkey) was utilized as a feedstock in the ODS process with an Initial sulfur concentration of 9 ppm. Dibenzothiophene (DBT) supplied by (Sigma Aldrich) was employed as the model refractory aromatic sulfur compounds (purity of ~98%). Nanoparticles of gamma alumina (obtained from Sky Spring Nanomaterials Inc.) were utilized as catalyst support< the γ-Al_2O_3 properties are illustrated in Table 1.

Table 1. Properties of γ-Alumina nanoparticle.

Properties	Values	Unit
Bulk density	0.333	g/m^3
BET surface area	500.0	m^2/g
Pore volume	1.50	cm^3/g
Pore size	20	nm

Zinc acetate {$Zn(CH_3COO)_2.2H_2O$)} obtained from (Sigma) has been employed as the active metal in the prepared nano-catalyst with a purity of 99%. Hydrogen peroxide (H_2O_2), provided by Aldrich Company with a purity of 99.99%, has been used in the ODS reaction as a source of oxygen atoms that oxidize the sulfur compounds to sulfoxides and sulfones. Zinc oxide (ZnO) was loaded on γ-Al_2O_3 with 3%, 6%, and 9% (weight %) via an incipient wetness impregnation (IWI). At first, γ-Al_2O_3 was introduced in deionized water with stirring for half an hour. After that, $Zn(CH_3COO)_2{\cdot}2H_2O$) was mixed with the dispersed γ-Al_2O_3 support with stirring for 5 h under 95 °C. The resultant material was dried under 95 °C in an oven overnight and finally calcined for 3 h at 300 °C by using a furnace with a temperature ramping rate of 3 °C/min to produce nano-

catalysts (ZnO/ γ-Al_2O_3) with various loading of ZnO. The oxidative desulfurization process was applied in a batch reactor by employing hydrogen peroxide (H_2O_2) as an oxidizing agent and diesel fuel as feedstock with an initial sulfur (DBT) concentration of 611 ppm. The oxidation reaction was conducted at various process conditions (reaction temperature and operating time) to evaluate the ODS reaction efficiency in the presence of the synthesized nano-catalyst. The ODS technology is presented in Figure 1.

The mathematical modeling technique for the ODS process was applied by the software of gPROMS (General Process Modeling System) [13]. The group of equations employed in the mathematical modeling technique for ODS operations is summarized in Table 2.

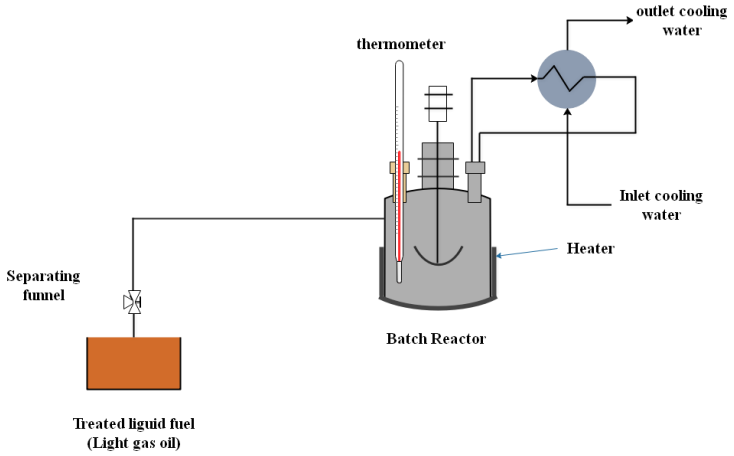

Figure 1. Schematic diagram of the ODS process.

Table 2. Equations employed in the Mathematical modeling technique.

Parameter	Equations/values	Eq.	Reference
Reaction rate ($-r_{DBT}$)	$(-r_{DBT}) = \eta_0 \, A \, {C_{DBT}}^n$	(1)	[16]
Arrhenius equation (A)	$A=A_0 e^{(-\frac{EA}{RT})}$	(2)	[17,18]
The final sulfur concentration (C_{DBT})	$C_{DBT} = [\, {C_{DBT,t}}^{(1-n)} + (n-1).t.A_{in}\,\eta_0]^{(\frac{1}{1-n})}$	(3)	[19]
The effectiveness factor (η_0)	$\eta_0 = \frac{3(\phi \coth\phi - 1)}{\phi^2}$	(4)	[19,20]
Thiele modulus (ϕ)	$\phi = \frac{V_P}{S_P}\sqrt{(\frac{n+1}{2})\frac{A_{in}\,{C_{DBT}}^{(1-n)}\rho_p}{D_{ei}}}$	(5)	[19,20]
Effective diffusivity (D_{ei})	$D_{ei} = \frac{\varepsilon_B}{\mathcal{T}}\frac{1}{\frac{1}{D_{mi}}+\frac{1}{D_{ki}}}$	(6)	[16,20]
Porosity (ε_B)	$\varepsilon_B = V_g \rho_p$	(7)	[16,20]
Particle density (ρ_p)	$\rho_p = \frac{\rho_B}{1-\varepsilon_B}$	(8)	[16,20]
The tortuosity factor ($\mathcal{T}$)	The tortuosity factor value ($\mathcal{T}$) of the pore network ranged between (2.0 to 7.0)	----	[20]
The Knudsen diffusivity (D_{ki})	$D_{ki} = 9700\, r_g (\frac{T}{Mw_{DBT}})^{0.5}$	(9)	[16,19]
Mean pore radius (r_g)	$r_g = 2V_g/S_g$	(10)	[21]
The molecular diffusivity (D_{mi})	$D_{mi} = 8.93 * 10^{-8}(\frac{{v_{DF}}^{0.267}T}{{v_{DBT}}^{0.433}\mu_{DF}})$	(11)	[22,23]
DBT molar volume (v_{DBT})	$v_{DBT} = 0.285(v_{cDBT})^{1.048}$	(12)	[22]
Diesel fuel molar volume (v_{LGO})	$v_{DF} = 0.285(v_{cDF})^{1.048}$	(13)	[20]
Critical volume of diesel fuel (v_{cLGO})	$v_{cDF} = (7.5214 * 10^{-3}(T_{meABP})^{0.2896}(\rho_{DF,15.6})^{-0.7666})Mw_{DF}$	(14)	[20]
The catalyst's external volume (Vp) (sphere particle)	$V_p = \frac{\pi}{6}(d_p)^3$	(15)	[23]
The catalyst's external surface (Sp) (sphere particle)	$S_p = \pi(d_p)^2$	(16)	[23]
Viscosity of fuel (μ_{LGO})	$\mu_{LGO} = 3.141 * 10^{10}(T-460.0)^{-3.444}(logAPI)^{\alpha}$	(17)	[24]
Dimensionless No. (α)	$\alpha = 10.3130[log_{10}(T-460)] - 36.4470$	(18)	[24]
American petroleum institute (API)	$\text{API} = \frac{141.50}{sp.gr_{DF15.6}} - 131.50$	(19)	[25]

The most accurate values of kinetic parameters can be determined by minimizing the difference between the results of practical experiments and the estimated results by applying the model. To estimate the accurate parameters values of the kinetic model, the minimization of the following objective function was:

$$OBJ = \sum_{n=1}^{N_t} \left(C_{DBT}^{\exp} - C_{DBT}^{pred} \right)^2 \quad (1)$$

where Nt is the experimental runs number, C_{DBT}^{exp} is the experimental results, and C_{DBT}^{pred} is the predicted modeling results.

The amount of DBT removal can be estimated based on the following equation:

$$X_{DBT} = 1 - \frac{C_{DBT}}{C_{DBT_t}} \quad (2)$$

where, X_{DBT} is the conversion of the DBT compound.

An optimization problem has been formulated for the evaluation of the kinetic model parameter to obtain the order of reaction (n), the pre-exponential factor (*A*o), and activation energy (EA) for each prepared catalyst by minimizing the sum of squared error (SSE) by subjecting the constraints of operation under given ODS conditions. The estimation of kinetic parameters is formulated as described in Table 3.

Table 3. Formulation of optimization problem of parameter estimation.

Given	Obtain	So as to minimize	Subjected to
Synthesized nanocatalyst Reactor formation ODS conditions	Order of reaction (n), the pre-exponential factor (Ao), and activation energy (EA) for each prepared catalyst.	Sum of squared error (SSE).	Constraints of operation

RESULTS AND DISCUSSION

Characterization of (ZnO/ γ-Al_2O_3) nano-catalyst

The BET test was achieved to reveal the pore dimensions and BET surface area of the synthesized nano-catalyst. As illustrated in Table 4, the results of BET detected that after zinc oxide (ZnO) loading, the volume of pores and the specific surface area reduce remarkably while the pore size rises. This behavior is attributed to the occupancy of zinc oxide in some spaces within the samples [13]. So, improving the performance of oxidative desulfurization reactions employing (ZnO/γ-Al2O3), nano-catalyst can be returned to enhance the catalyst properties and activity via ZnO loading.

The average particle size distribution of synthesized (ZnO/ γ-Al_2O_3) nano-catalysts was estimated by utilizing the AFM test. As shown in Figure S1 (Supporting material), the average particle size for all synthesized nano-catalysts is less than 100 nm, where the average nanoparticle diameter (d_p) is 79.05 nm for 3% ZnO/ γ-Al_2O_3, 81.35 nm for 6% ZnO/ γ-Al_2O_3 and 84.54 nm for 9% ZnO/ γ-Al_2O_3.

Table 4. BET results of synthesized (ZnO/ γ-Al_2O_3) nano-catalysts.

Sample	Pore volume (cm^3/gm)	Specific surface area (m^2/gm)	Pore size (nm)
γ-Al_2O_3	1.5	500	20
3% ZnO/ γ-Al_2O_3	0.6342	457.462	27.183
6% ZnO/ γ-Al_2O_3	0.2954	413.218	33.149
9% ZnO/ γ-Al_2O_3	0.0846	388.765	39.543

Oxidative desulfurization results

The effect of ZnO loaded over the catalyst support on the removal of DBT compounds was evaluated by loading various amounts of ZnO (3%, 6%, and 9%) over the support of the catalyst. Figure 2 displays the impact of ZnO loading on the ODS efficiency. The removal of DBT compounds was enhanced by raising the loading ZnO over the catalyst's support. It might be owing to the availability of active sites that promote the activity of the ODS reaction. Also, the performance of the ODS process is remarkably improved via upgrading the catalyst properties and activity after ZnO loading.

The influence of temperature on the efficiency of the ODS reaction was investigated, and the results are presented in Figure 3.

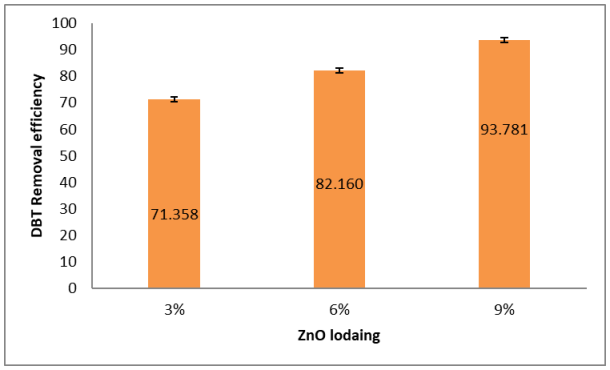

Figure 2. The effect of ZnO loading on the DBT elimination efficiency in ODS reaction.

For all synthesized nano-catalysts, the results detected that the removal of DBT accelerated with a rising reaction temperature. An increase in the reaction temperature enhances the movement of the molecules, which enhances the chance of collision and reaction between sulfur compounds and the oxidant. Also, at higher temperatures, the most robustly adsorbed sulfones will be eliminated from the catalyst surface readily [26–30]. The enhancement in the oxidation reactions can also be returned to improve the mass and heat transfer rates between the reacting species by enhancing the oxidation temperature. The increase in oxidation temperature can impact the physical properties of the fuel, like the density and viscosity, by reducing it, which leads to a high mass transfer rate and significantly faster oxidation reaction [1,2].

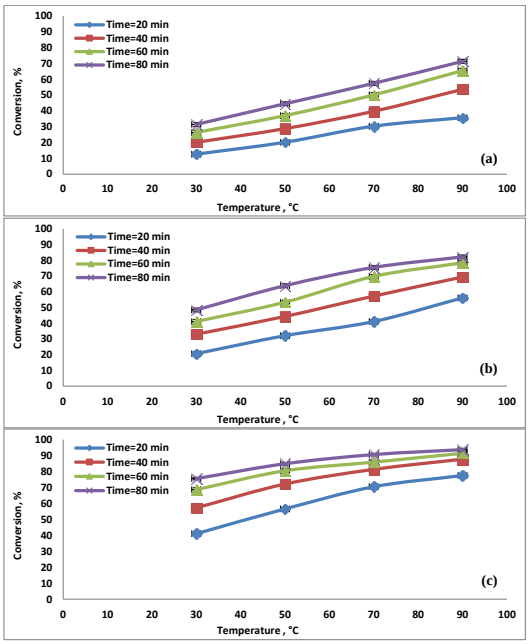

Figure 3. The effect of reaction temperature on the efficiency of ODS reaction for (a) 3% ZnO/ γ-Al_2O_3 (b) 6% ZnO/ γ-Al_2O_3 (c) 9% ZnO/ γ-Al_2O_3.

The reaction times effect on the removal of DBT compounds is illustrated in Figure 4. The DBT removal was promoted with increasing reaction time due to the enhanced reaction chance between DBT compounds and oxidizing agents with increasing reaction times. Also, the increasing collision time improved the mass transfer between the reacting materials and gave more time for catalyst activity through the reacting media, which led to high removal efficiency for sulfur compounds from the fuel [1,3].

Kinetic parameters estimation

The constant parameters utilized in the mathematical model are listed in Table 5. The optimal kinetic parameter values determined via the mathematical modeling are summarized in Tables S1–S3 next.

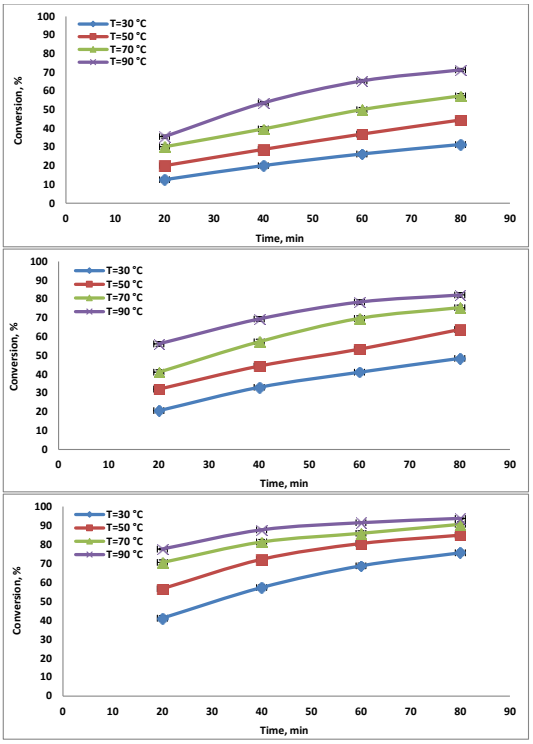

Figure 4. The effect of reaction time on the efficiency of ODS reaction for (a) 3% ZnO/ γ-Al_2O_3 (b) 6% ZnO/ γ-Al_2O_3 (c) 9% ZnO/ γ-Al_2O_3.

According to the data illustrated in these Tables, it is concluded that the (9% ZnO/ γ-Al_2O_3) nano-catalyst is superior to the other catalysts based on the reaction order at similar operation conditions. The reaction order of the (9% ZnO/ γ-Al_2O_3) is less than other catalysts, which denotes that the reaction rate in existence (9% ZnO/ γ-Al_2O_3) is faster than the other synthesized nano-catalysts.

Experimental and simulation data

The simulation of ODS technology is conducted by employing the gPROMS software. The experimental data and expected simulation are summarized in Tables S4 to S6.

Optimal operation conditions for a minimum DBTconcentration

The best values of process conditions are estimated using the most accurate values of kinetic parameters attained by applying the simulation process. Predicting the best operating conditions values for achieving the minimum sulfur content is essential. Therefore, the optimization technique is built as follows:

Given: Interaction order, reactor performance, catalyst, and k_o and EA for the interaction.

Obtain: The better operating conditions for high

Table 5. Constant parameters employed in the mathematical modeling technique.

Parameter, unit	Value
Initial concentration of DBT compounds ($C_{DBT.t}$), ppm	611
Time, min	$time_1$=20, $time_2$=40, $time_3$=60, $time_4$=80
Temperature (T), °C	T_1 = 30, T_2 = 50, T_3 = 70, T_4 = 90
Diesel fuel density at 15.5°C (ρ_{DF}), gm/cm^3	0.8205
Mean average boiling point (T_{meABP}), °R	957
Acceleration gravity (g), m/sec^2	9.81
Gas constant (R), J/mole.°K	8.314
Pore volume per unit mass of catalyst (Vg), cm^3/gm	Vg, (3% ZnO/ γ-Al_2O_3) = 0.6342 Vg, (6% ZnO/ γ-Al_2O_3) = 0.2954 Vg, (9% ZnO/ γ-Al_2O_3) = 0.0846
Specific surface area of a particle (Sg), cm^2/gm	Sg, (3% ZnO/ γ-Al_2O_3) = 4574620 Sg, (6% ZnO/ γ-Al_2O_3) = 4132180 Sg, (9% ZnO/ γ-Al_2O_3) = 3887650
Catalyst particle volume (Vp), cm^3	Vp, (3% ZnO/ γ-Al_2O_3) = 3.163*10^{-16} Vp, (6% ZnO/ γ-Al_2O_3) = 2.818*10^{-16} Vp, (9% ZnO/ γ-Al_2O_3) = 3.163*10^{-16}
External surface area of a particle (Sp), cm^2	Sp, (3% ZnO/ γ-Al_2O_3) = 1.963*10^{-10} Sp, (6% ZnO/ γ-Al_2O_3) = 2.079*10^{-10} Sp, (9% ZnO/ γ-Al_2O_3) = 2.245*10^{-10}
Bulk density (ρ_B), gm/cm^3	$\rho_{B.}$ (3% ZnO/ γ-Al_2O_3) =0.343 $\rho_{B.}$ (6% ZnO/ γ-Al_2O_3) =0.351 $\rho_{B.}$ (9% ZnO/ γ-Al_2O_3) =0.386
Diesel fuel molecular weight (M_{wLDF}), gm/mole	200.468
Sulfur molecular weight (M_{wDDT}), gm/mole	32.06
Mean pore radius (r_g), nm	r_g, (3% ZnO/ γ-Al_2O_3) =2.772 r_g, (6% ZnO/ γ-Al_2O_3) =1.429 r_g, (3% ZnO/ γ-Al_2O_3) =0.352

removal of sulfur.

So as to minimize: Sulfur content.

Subjected to: Constraints in the operation.

The problem is formulated mathematically as follows:

$$Min \quad C_{DBT}$$

$$T^j, time_i^j, C_{DBT}^j \quad \begin{pmatrix} j = 3\% ZnO / \gamma - Al_2O_3, \\ 6\% ZnO / \gamma - Al_2O_3 \ \& \\ 9\% ZnO / \gamma - Al_2O_3 \end{pmatrix}$$

$$S.t.f\left(z, x(z), \dot{x}(z), u(z), v\right) = 0 \quad time_L^j \le time^j \le time_U^j$$

$$C_{DBT.tL}^j \le C_{DBT.t}^j \le C_{DBT.tU}^j$$

$$T_L^j \le T^j \le T_U^j$$

$$X_{DBT.tL}^j \le X_{DBT.t}^j \le X_{DBT.tU}^j$$

The optimization solution method is conducted by applying the gPROMS program. The optimal operating conditions for each synthesized nano-catalysts are illustrated in Tables S7 to S9.

CONCLUSION

The desulfurization of DBT via oxidation technology in diesel fuel fraction was conducted in a batch reactor at various operating conditions (reaction temperatures and reaction times), utilizing a synthesized nano-catalyst (ZnO/γ-Al_2O_3) and oxidant of hydrogen peroxide as oxidant, at (1 atm) to reach the minimum DBT content. The ODS system in this paper is highly effective in eliminating DBT compounds found in the light gas oil cut, where the maximum DBT removal of (93.8%) was achieved under a temperature of 90 °C in 80 min in the presence of a synthesized nano-catalyst (9% ZnO/γ-Al_2O_3). Also, the high quality of light gas oil fuel was achieved by minimizing the sulfur concentration by applying mathematical modeling technology. The optimal values of operating conditions to obtain cleaner fuel (DBT elimination > 98%) were a processing time of 200 min and a process temperature of 87 °C with the synthesized nano-catalyst (9% ZnO/γ-Al_2O_3). The new mathematical model for the ODS reactions is evaluated as the most appropriate kinetic variable for the newly synthesized nano-catalysts under mild operating conditions. Also, finding a mathematical model is the main matter in improving, designing, and scaling up the ODS for the industrial fields.

REFERENCES

[1] S.A. Jafar, A.T. Nawaf, J.I. Humadi, Mater. Today: Proc. 42 (2021) 1777–1783. https://doi.org/10.1016/j.matpr.2020.11.821.

[2] J.I. Humadi, S.A. Gheni, S.M.R. Ahmed, G.H. Abdullah, A.N. Phan, A.P. Harvey, Process Saf. Environ. Prot. 152 (2021) 178–187. https://doi.org/10.1016/j.psep.2021.05.028.

[3] G.S. Ahmed, J.I. Humadi, A.A. Aabid, Iraqi. J. Chem. Pet. Eng. 22 (2021) 11–17. https://doi.org/10.31699/IJCPE.2021.3.2.

[4] A.T. Albayrak, A. Tavman, Ultrason. Sonochem. 83 (2022) 105845. https://doi.org/10.1016/j.ultsonch.2021.105845.

[5] A. Akopyan, E. Eseva, P. Polikarpova, A. Kedalo, A. Vutolkina, A. Glotov, Molecules 25 (2020) 536. https://doi.org/10.3390/molecules25030536.

[6] H. Zhao, G.A. Baker, Front. Chem. Sci. Eng. 9 (2015) 262–279. https://doi.org/10.1007/s11705-015-1528-0.

[7] N.P. Radhika, R. Selvin, R. Kakkar, A. Umar, Arabian J. Chem. 12 (2019) 4550–4578. https://doi.org/10.1016/j.arabjc.2016.07.007.

[8] P. Polikarpova, A. Akopyan, A. Shigapova, A. Glotov, A. Anisimov, E. Karakhanov, Energy Fuels 32 (2018) 10898–10903. https://doi.org/10.1021/acs.energyfuels.8b02583.

[9] S. Subhan, A.U. Rahman, M. Yaseen, H.U. Rashid, M. Ishaq, M. Sahibzada, Z. Tong, Fuel 237 (2019) 793–805. https://doi.org/10.1016/j.fuel.2018.10.067.

[10] Z. Ismagilov, S. Yashnik, M. Kerzhentsev, V. Parmon, A. Bourane, F. M. Al-Shahrani, A. A. Hajji, O. R. Koseoglu, Catal. Rev.: Sci. Eng. 53 (2011) 199–255. https://doi.org/10.1080/01614940.2011.596426.

[11] J. I. Humadi, S. A. Gheni, S. M. Ahmed, A. Harvey, RSC Adv. 12 (2022) 14385–14396. https://doi.org/10.1039/D2RA01663J.

[12] J. I. Humadi, A.T. Nawaf, A.T. Jarullah, M.A. Ahmed, S.A. Hameed, I. M. Mujtaba, Chem. Eng. Res. Des. 190 (2023) 634–650. https://doi.org/10.1016/j.cherd.2022.12.043.

[13] J.I. Humadi, Y.S. Issa, D. Y. Aqar, M. A. Ahmed, H.H. Ali Alak, I.M. Mujtaba, Int. J. Chem. React. Eng. 21(6) (2023) 727–741. https://doi.org/10.1515/ijcre-2022-0046.

[14] M.I. Fathi, J.I. Humadi, Q.A. Mahmood, A.T. Nawaf, R.S. Ayoub, AIP Conf. Proc. 2660 (2022) 020026 https://doi.org/10.1063/5.0109089.

[15] A.A. Aabid, J.I. Humadi, G.S. Ahmed, A.T. Jarullah, M.A. Ahmed, W.S. Abdullah, Appl. Sci. Eng. Prog. (2023). https://doi.org/10.14416/j.asep.2023.02.007.

[16] A.T. Nawaf, A.T. Jarullah, L.T. Abdulateef, Bull. Chem. React. Eng. Catal. 14 (2019) 79–92. https://doi.org/10.9767/bcrec.14.1.2507.79-92.

[17] P. Huang, G. Luo, L. Kang, M. Zhu, B. Dai, RSC Adv. 7 (2017) 4681–4687. https://doi.org/10.1039/C6RA26587A.

[18] B. Saha, S. Kumar, S. Sengupta, Chem. Eng. Sci. 199 (2019) 332–341. https://doi.org/10.1016/j.ces.2018.12.063.

[19] S.A. Ghazwan, A.T. Jarullah, B. Al-Tabbakh, I.M. Mujtaba, J. Cleaner Prod. 257 (2020) 120436. https://doi.org/10.1016/j.jclepro.2020.120436.

[20] A.T. Jarullah, K. Sarmad, B. Al-Tabbakh, I.M. Mujtaba, Chem. Prod. Process Model. 17(3) (2022) 213–233. https://doi.org/10.1515/cppm-2020-0097.

[21] A.T. Nawaf, H.H. Hamed, S.A. Hameed, A.T. Jarullah, I.M. Mujtaba, Chem. Eng. Sci. 232 (2021) 116384. https://doi.org/10.1016/j.ces.2020.116384.

[22] A.T. Nawaf, A.T. Jarullah, Sh. A. Hameed, I.M. Mujtaba, Chem. Prod. Process Model. 16(3) (2021) 229–249 (2021), https://doi.org/10.1515/cppm-2020-0107.

[23] A.T. Jarullah, S.K. Aldulaimi, B.A. Al-Tabbakh, I.M. Mujtaba, Chem. Eng. Res. Des. 160 (2020) 405–416. https://doi.org/10.1016/j.cherd.2020.05.015.

[24] K.I. Hamad, J.I. Humadi, Y.S. Issa, S.A. Gheni, M.A. Ahmed, A.A. Hassan, Cleaner Eng. Technol. 11 (2022). 100570. https://doi.org/10.1016/j.clet.2022.100570.

[25] A.T. Jarullah, I.M. Mujtaba, A.S. Wood, Fuel 90 (2011) 2165–2181. https://doi.org/10.1016/j.fuel.2011.01.025.

[26] N. Ghorbani, G. Moradi Chin. J. Chem. Eng. 27 (2019) 2759–2770. https://doi.org/10.1016/j.cjche.2019.01.037.

[27] S. A. Barham, L. O. Hamasalih, K. H. H. Aziz, K. M. Omer, & I. Shafiq, Proc. 10 (2022) 2327. https://doi.org/10.3390/pr10112327.

[28] B. S. Ahmed, L. O. Hamasalih, K. H. H. Aziz, Y. M. Salih, F. S. Mustafa, & K. M. Omer, Sep. 10 (2023) 206. https://doi.org/10.3390/separations10030206.

[29] J. I. Humadi, S. A. Jafar, N. S. Ali, M. A. Ahmed, M. J. Mzeed, R. J. Al-Salhi, & T. M. Albayati, Sci. Rep. 13 (2023) 9931. https://doi.org/10.1038/s41598-023-37188-9.

[30] G. H. A. Razzaq, M. A. Shihab, J. I. Humadi, K. K. Saxena, C. Prakash, & L. I. Saeed, Mater. Today: Proc. (2023). https://doi.org/10 .1016/j.matpr.2023.05.432.

JASIM I. HUMADI[1]
MUAYAD A. SHIHAB[1]
GHAZWAN S. AHMED[2]
MUSTAFA A. AHMED[3]
ZEYAD A. ABDULLAH[4]
SHANKAR SEHGAL[5]

[1]Department of Petroleum and Gas Refining Engineering, College of Petroleum Processes Engineering, Tikrit University, Slah Al-deen, Iraq

[2]Chemical Engineering Department, College of Engineering, Tikrit University, Iraq

[3]Ministry of Oil, North Refineries Company, Baiji Refinery, Slah Al-deen, Iraq

[4]The State Company for Drugs Industry and Medical Appliances, Slah Al-deen, Iraq

[5]Mechanical Engineering, UIET, Panjab University, Chandigarh, India

NAUČNI RAD

MODELOVANJE I KINETIČKA PROCENA PROCESA DESUMPURIZACIJE DIZEL GORIVA KORIŠĆENJEM NANO- ZnO/Al_2O_3

U ovom radu, sintetisan je nano-katalizator sa cink-oksidom (ZnO) nanetim na γ-alumini (γ-Al_2O_3), tj. ZnO/g-Al_2O_3, namenjen ubrzavanje uklanjanja jedinjenja sumpora iz lakog gasnog ulja oksidativnom desulfurizacijom. Sintetizovani nanokatalizatori su okarakterisani mikroskopijom atomskih sila i Brunauer-Emet-Telerove metode. Oksidativna desulfurizacija je sproveden u šaržnom reaktoru na različitim temperaturama i vremenima reakcije (30–90 °C i 20–80 min). Uklanjanje dibenzotiofena je bilo najveće (93,8%) pri korišćenju sintetizovanog nanokatalizatora (9% ZnO/ γ-Al_2O_3) na 90 °C za 80 min. Na osnovu dobijenih eksperimentalnih podataka, izvedena je nova tehnika matematičkog modelovanja oksidativne desulfurizacije u blagim eksperimentalnim uslovima kako bi se procenile najprikladnije kinetičke promenljive za novosintetizovane nanokatalizatore. Rezultati simulacije ukazuju na dobro poklapanje sa eksperimentalnim zapažanjima sa manje od 5% apsolutne prosečne greške za sve serije. Procedura optimizacije uslova procesa sa nanokatalizatora (9% ZnO/ γ-Al_2O_3) pokazuje da se više od 98% dibenzotiofena može eliminisati u roku od 200 min, na 87 °C.

Ključne reči: γ-alumina; model; nano-katalizator; optimizacija; sumpor; cink oksid.

CI&CEQ
Chemical Industry & Chemical Engineering Quarterly

Available online at
Association of the Chemical Engineers of Serbia AChE
www.ache.org.rs/CICEQ

Chem. Ind. Chem. Eng. Q. 30 (2) 161–177 (2024) CI&CEQ

RICARDO ARBACH FERNANDES DE OLIVEIRA
JULIO HENRIQUE ZANATA
GABRIELA CANTARELLI LOPES

Department of Chemical Engineering, Federal University of São Carlos, São Carlos - São Paulo – Brazil

NUMERICAL STUDY OF TURBULENCE ON DRAG COEFFICIENT DETERMINATION FOR PARTICLE AGGLOMERATES

Article Highlights

- A numerical study of the flow around particle agglomerates was performed
- Steady RANS turbulence models were tested to estimate the drag coefficient
- SST k-ω and Spalart-Allmaras turbulence models better represented the flow
- SST k-ω turbulence model presented lower deviations from the empirical correlation
- RNG k-ε presented the worst results, mainly for intermediate Reynolds number

Abstract

Numerical simulations of the flow surrounding particle agglomerates were carried out using computational fluid dynamics to assess the ability of five RANS turbulence models to estimate the drag coefficient in particle agglomerates. Simulations were carried out in steady conditions for Reynolds numbers between 1 and 1500. Streamlines showed that symmetrical agglomerates present a velocity profile similar to the single sphere profile. Results showed that both Spalart-Allmaras and SST k-ω turbulence models could represent the flow profile in the regions near and far from the walls of the agglomerates and the wake region in the rear of the agglomerates. The RNG k-ε model showed poor quality in predicting the velocity profile and the drag coefficient. The drag coefficient obtained by simulations presented a trend better represented by the Tran-Cong model, also showing that deviations from the predictions decreased as the packing density of the agglomerate increased. The use of steady RANS simulations showed to be a feasible and efficient method to predict, with low computational cost, the drag coefficient in particle agglomerates. For the transition and turbulent flows, results presented good agreement, with deviations between -15% and 13%, while for lower Reynolds numbers, deviations varied between -25% and 5%.

Keywords: particulate matter, particle agglomerates, turbulence, drag coefficient, computational fluid dynamics.

SCIENTIFIC PAPER

UDC 532.5:519

In designing equipment involving particle-laden flows, it is essential to correctly model the interaction between the two phases to obtain consistent results. The forces of fluid-particle interaction are directly related to the characteristics of the particles, such as size, shape, elasticity, and roughness, which are determinants in the performance of equipment such as the fluidized bed [1–4]. Usually, in models that simulate fluidized bed reactors, the drag force is related to the porosity of the bed, assuming that the particles are distributed homogeneously [5–8]. However, depending on their physical, superficial, and mechanical characteristics, the collision, attraction, and friction between the particles can lead to the formation and irregular distribution of agglomerates, altering the flow dynamics through pressure oscillations [9,10].

Indeed, the behavior of particle agglomeration in different arrangements deserves attention, as it occurs in almost all forms, whether naturally or artificially. One can find such kind of irregularly shaped particles in

Correspondence: G.C. Lopes, Department of Chemical Engineering, Federal University of São Carlos, Rodovia Washington Luís, km 235 - SP-310, São Carlos - São Paulo - Brazil, P.O. Box: 13565-905.
E-mail: gclopes@ufscar.br
Paper received: 6 December, 2022
Paper revised: 4 June, 2023
Paper accepted: 14 August, 2023

https://doi.org/10.2298/CICEQ221206021O

many applications, such as sedimentation and flocculation of fine particle aggregates in rivers and lakes, chemical mixing, mineral processing, stirred tanks, powder sintering, and manufacturing with phase change processes [11–13]. For several of these processes, determining the particle's terminal velocity is an important stage for designing and optimizing processes and equipment. Since this velocity is straightly dependent on the body's drag coefficient, such a study is important to simulate the movement of such particles.

Due to the lack of an analytical solution, the literature presents several empirical correlations designed to predict the drag coefficient of spherical and non-spherical particles associated with different ranges of validity and precision [14–19]. To obtain predictions that better represent the empirical observations, shape descriptors have been developed in recent decades to quantify aspects such as shape, circularity, roughness, and sphericity. However, the correlations present some disadvantages, such as the fact that the first studies are mainly, based on experiments with regularly-shaped particles such as cubes, cylinders, and disks, which reduces the level of detail and accuracy in the description of the local scale phenomena [20,21].

For the evaluation of the drag coefficient of isolated groups of ordered packed spheres moving through Newtonian fluids, Tran-Cong *et al.* [11] conducted laboratory measurements, leading to a correlation with good agreement over a limited range of Reynolds numbers and body dimensions but covering most of the irregularly shaped particles in engineering applications. Beetstra *et al.* [20] compared these experimental data with lattice-Boltzmann simulations for the same conditions, aiming to expand the field of the influence of the geometry on the disturbance of fluidized beds, stating that, indeed, the drag force on each particle is strongly dependent on the inter-particle distance variation. The results showed how the omission of the agglomeration effect could cause deviations between the simulated equipment behavior and experimental results.

The literature presents studies using the lattice-Boltzmann method (LBM) and Direct Numerical Simulation (DNS) to evaluate particle drag coefficients. For industrial-scale problems, these approaches are considered impractical, due to the high computational effort, mainly for high Reynolds numbers, since the simulations must be carried out in a transient formulation with small timesteps and the mesh must be fine enough, to respect the Kolmogorov scales [22,23]. However, in the field of sub-grid scale, they are very useful for understanding the influence of turbulence in small-scale vortices. The LBM is useful for CFD to understand particle flow due to the algorithm's simplicity and explicit methods [24]. Since the method presents a high resolution of the domain, the studies present better accuracy, as observed in studies such as Dietzel and Sommerfeld [25], that used the LBM to investigate complex geometry with a high discretization around the agglomerate and obtained deviations lower than 10% for lower values of Reynolds, where deviations are generally by the order of 20% [25].

DNS is an important tool to estimate, with accuracy, correlations for the micro-scale transport coefficients, one of the essential parameters for coarse-grained models of fluid-particle systems [21]. To understand the fluid-particle mass transfer in random arrays of particles, Mehrabadi *et al.* [26] performed DNS in a homogeneous flow, aiming to isolate the effect of interphase interactions on a particle agglomerate, developing a gas-solid drag law for clustered particles based on the conclusion that particle clusters lead to a drag reduction. Another recent example of this method is the study of Chen *et al.* [27], where the drag and lift in particle agglomerates were studied for different orientations and sizes of particles and presented deviations between 2 and 4%. However, due to the method's constraints, the study focused on understanding the hydrodynamic on agglomerates for a range of Reynolds below 100, highly dependent on the projected area [25].

In contrast to the large number of empirical correlations to predict the drag coefficient of irregular particles, there is a scarcity of studies in which specific correlations have been proposed to determine drag forces acting on particle agglomerates. The literature in the computational field using the unsteady formulation, such as LES and DNS, focuses on analyzing simple bodies – such as regularly-shaped single bodies – due to the difficulty in generating uniform meshes around complex bodies, as well as limited to low Reynolds flows, generally below 250, due to the computational demands associated with higher Reynolds numbers [22]. The use of LBM eliminates the difficulty of mesh generation, so we observe studies on more complex and arbitrary bodies [25] with an agglomeration of several spheres. However, the method is still limited for low Reynolds flows since the forces acting on walls inside the flow are directly calculated in the smaller scales [20,21,24–27].

Because of the lack of studies for higher Reynolds flows and since the high computational cost needed to perform transient simulations, we focus on proposing a methodology using the steady formulation to simplify the problem of calculating the drag coefficient in complex bodies, which allowed the investigation of the flow for a wide range of Reynolds numbers. Since

turbulence plays an important role in the flow profile as we increase the velocity of the fluid, we focused on how its modeling interferes with the drag estimation in particle agglomerates. So, the present paper evaluates the drag coefficient of three different conformations of irregularly shaped particle agglomerates composed of spherical particles surrounded by a water flow, varying the turbulence model tested. The models were compared using steady RANS turbulence models to investigate their robustness to predict the drag acting in particle agglomerates for different conformations to reduce the computational costs of unsteady simulations, such as URANS, LES, DNS, or LBM.

MATERIALS AND METHODS

Materials

This study was carried out in the theoretical field, using CFD simulations to obtain the flow profile of water around particle agglomerates. The drag coefficient of the particles was calculated by CFD simulations using five different turbulence models. The results were compared with five empirical correlations for estimating the drag coefficient in irregularly-shaped particles present in literature to find which is robust enough to represent the trend of the results of the drag coefficient in particle agglomerates obtained by simulations.

In the theoretical field, the drag coefficient for spheres is simple to calculate since it depends on a balance of forces. This balance leads to Eq. (1)

$$C_p = \frac{F_D}{0.5\rho_f A\left|u_p - u_f\right|\left(u_p - u_f\right)} \quad (1)$$

where F_D is the drag force. The drag depends on the fluid, particle, and flow characteristics, i.e., fluid density and velocity, ρ_f and u_f, respectively, and the particle velocity and reference area, u_p and A, respectively. The particle in the domain of the present study is fixed, leading to a particle velocity equal to zero, so the fluid flow profile and the drag coefficient are given exclusively by the behavior of the fluid flow around the particle.

To determine which correlation better follows the trend observed in the drag coefficient obtained by CFD, we must define some criteria to compare the simulations with the correlations. The first consideration was analyzing and comparing the flow profile for each of the five turbulence models with the behavior expected by the literature. This step is important to understand if the results obtained for the drag coefficient are reliable.

Since a quantitative analysis is crucial, we also evaluated the percent deviation between simulations and correlations, estimated by Eq. (2).

$$\sigma = 100\frac{C_D^{corr} - C_D^{sim}}{C_D^{corr}} \quad (2)$$

where C_D^{corr} and C_D^{sim} are the drag coefficients obtained by the correlation and the simulation, respectively. Another quantitative analysis considered was the root-mean-square error, *RMSE*, given by

$$RMSE = \sqrt{\frac{\sum_{i=1}^{N}\left(\hat{x}_i - x_i\right)^2}{N}} \quad (3)$$

where $\hat{x}_i$ is the value of the i^{th} data of a parameter estimated by the correlation, x_i is the value of the i^{th} data of the parameter obtained by simulation – i.e., the drag coefficient – and N is the local data in the sample studied.

Numerical simulations

The numerical simulations were carried out using the software ANSYS 14.5. The computational domain and numerical meshes of the particle agglomerates in this study were generated using the software ANSYS Design Modeler and Meshing. ANSYS Fluent 14.5 was used to solve the model equations. CFD-Post was used to analyze the fluid flow profile and the drag coefficient.

Design and mesh generation

Simulations were carried out for three different computational domains, varying the geometry of the agglomerates containing three, four, and five particles, where the radius of each particle in the agglomerate measures 0.5 cm. The domain generated corresponds to a parallelepiped with a height and width of 0.1 m and a length of 0.2 m.

Aiming to generate well-structured meshes, the domain was divided into two cubes, as presented in Figure 1. The cube on the left side, close to the inlet, was subdivided into seven smaller parts to control better the quality of the elements around the agglomerate of spheres. Six of them are pyramidal-shaped, connected to an inner cube, surrounding the agglomerate of spheres, and positioned in the center of the major cube. For the second cube, on the right side and close to the outlet, it was unnecessary to divide it into smaller parts. Figure 1 also shows a cut of the lateral view of the computational domain using the agglomerate of five spheres as an example, while Figure 2 shows the isometric view of the geometry of the three agglomerates.

Meshes statistics

Before running simulations, it is important to

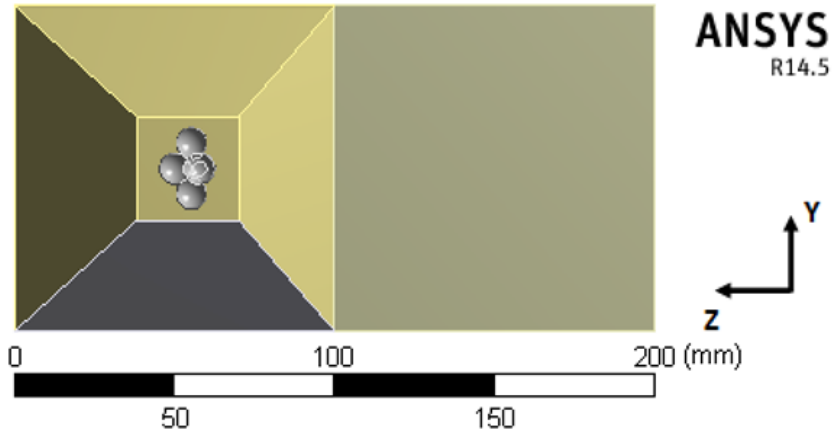

Figure 1. Example of the lateral view of the interior of the computational domains simulated.

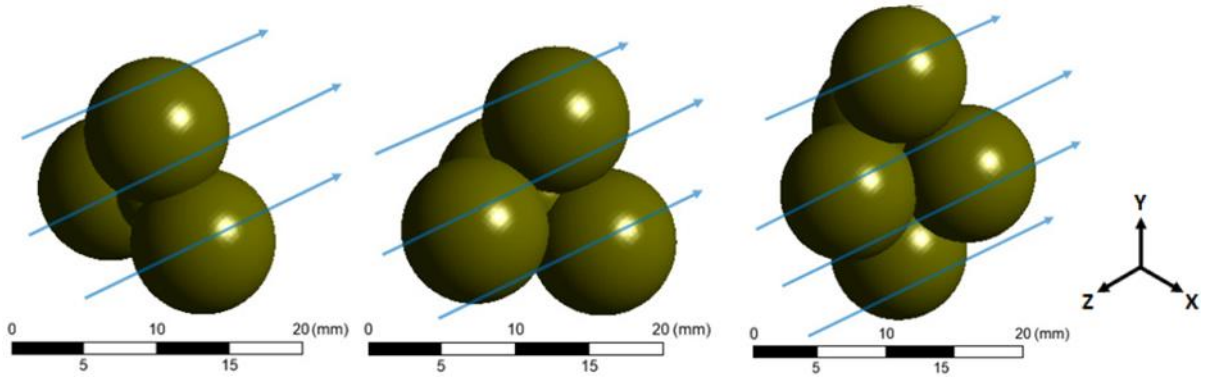

Figure 2. From left to right: Isometric view of the particle agglomeration of three, four, and five particles and a scheme of the flow direction.

analyze the quality of the mesh by verifying the elements according to their shape and criteria for several mesh quality parameters. In this study, its aspect ratio, orthogonality, and skewness were evaluated. To obtain convergence stability easier and better accuracy, it is ideal to have elements exclusively hexahedral. However, hybrid meshes were generated due to the complexity of the agglomerates' geometry. These meshes contain elements with shapes referred to as tetrahedral, six-node wedge, five-node pyramid, and hexahedral.

To avoid distorting the mean values and standard deviations, the values are presented separately according to two regions: the inner cube around the agglomerate (Figure 1), referred to as the subdomain, and the whole computational domain, referred to as the total domain. Table 1 shows the values of the minimum, maximum, mean, and standard deviation of the three parameters for the tested meshes, detailed for the subdomain and the total domain.

The minimum value possible for the aspect ratio is 1, where the quality is considered excellent for values lower than 20 [28,29]. For both the total domain and subdomain, the maximum values obtained were above 20. However, their average values are lower than 1.2, with standard deviations lower than 0.48%. Analyzing the aspect ratio of the three meshes presented in Table 2, we find many elements with values below 5, which are considered excellent for this criterion.

The orthogonality varies from 0 to 1, where values above 0.8 are considered excellent [28,29]. Even though some elements present poor quality, the mean value for each proposed domain was above 0.94, with a standard deviation lower than 0.1%, where elements with orthogonality above 0.8 correspond to at least 94% of the elements, as seen in Table 2. It occurs due to the high quantity of hexahedrons, which tend to have higher orthogonality. This effect is also present in skewness. Analyzing the skewness, where elements have excellent quality for values between 0 to 0.2 and good quality for values between 0.2 and 0.4, we observe that the mean values do not exceed 0.07, and the standard deviations do not exceed 0.12% for any mesh. The low value directly results from the high quantity of hexahedrons with good and excellent quality.

Pyramidal shapes, such as tetrahedrons and five-

Table 1. Mesh quality for the three agglomerates studied.

Mesh quality parameter		Subdomain			Total domain		
		3 spheres	4 spheres	5 spheres	3 spheres	4 spheres	5 spheres
Aspect ratio	Minimum	1	1	1	1	1	1
	Maximum	32.12	24.58	299.98	32.12	24.58	299.98
	Mean	1.123	1.186	1.187	1.061	1.069	1.076
	SD (%)	0.403	0.476	0.547	0.284	0.306	0.349
Orthogonality	Minimum	0.212	0.152	0.032	0.210	0.152	0.032
	Maximum	1	1	1	1	1	1
	Mean	0.962	0.944	0.944	0.987	0.984	0.982
	SD (%)	0.081	0.093	0.095	0.052	0.056	0.060
Skewness	Minimum	0	0	0	0	0	0
	Maximum	0.975	0.993	0.987	0.982	0.997	0.999
	Mean	0.041	0.062	0.063	0.018	0.022	0.024
	SD (%)	0.120	0.142	0.114	0.078	0.088	0.094

Table 2. Percentage of elements of the meshes attending to the criteria of the quality coefficients.

Region	Agglomerate	Number of elements	Aspect ratio Below 5 (%)	Orthogonality Above 0.8 (%)	Skewness Below 0.4 (%)
Subdomain	3 spheres	1240970	99.99	96.24	96.39
	4 spheres	1064255	99.96	94.25	94.59
	5 spheres	1328015	99.97	94.21	94.41
Total domain	3 spheres	5234907	99.99	98.67	98.64
	4 spheres	5001753	99.99	97.89	98.17
	5 spheres	5220320	99.98	97.98	97.87

node pyramids, are expected to have lower orthogonality and higher skewness [29]. Table 2 shows that the influence of such shapes on the quality of the meshes was not significant because of the low number of pyramidal elements – representing less than 2.5% of the elements of the subdomain and less than 0.5% of the total domain for all meshes.

It is relevant to emphasize the predominance of hexahedral elements for both subdomain and total domain in all meshes. The agglomerate of three spheres presented percentages of hexahedral elements above 83% in the subdomain and 93% in the total domain. In the meshes of agglomerates of four and five spheres, these percentages were above 92% in the subdomain and 95% in the total domain. Also, analyzing the meshes statistics for three main parameters, the elements have good or excellent quality, so the meshes are expected to behave with convergence stability and obtain accurate results.

The governing equations

The time-averaged conservation equations for the steady incompressible isothermal turbulent flow in the three-dimensional model, neglecting body force, can be expressed by the equations of continuity and motion [22].

The closure equations for the RANS approach depend on the turbulence model used. In this study, we investigated the effects of five turbulence models. The models are classified according to the number of transport equations used to close the modeling of the problem. The tested models are the one-equation-based Spalart-Allmaras, the two-equation-based RNG k-ε, SST k-ω, the four-equation-based Langtry-Menter, and the six-equation Reynolds stress model. The modeling of its closure equations and coefficients is better detailed in the literature [30–34].

Simulation setup

The fluid properties were set up for an isothermal operation condition of 25 °C, obtaining water density and viscosity of 998.2 kg/m^3 and 1.003 x 10^{-3} Pa·s, respectively. As a boundary condition, the inlet velocity of the water was set as an injection normal to the inlet surface. Since the drag experienced by particles flowing in a Newtonian fluid can be divided into seven main flow regimes according to its Reynolds number, we varied the velocities of the flow to obtain Reynolds numbers between 1 and 1500 to ensure that we will observe how the turbulence model interferes on the

estimation of the drag coefficient in all the regimes, from laminar to turbulent wake flow regimes [35,36]. The velocities varied from 5 x 10^{-5} to 0.10501 m/s, as presented in Table 3, according to the agglomerate, to obtain the range of Reynolds numbers proposed, calculated by Eq. (4).

$$\mathrm{Re} = \frac{\rho\, u\, d_{eq}}{\mu} \tag{4}$$

where ρ, u, μ are the density, relative velocity, and viscosity of the fluid, and d_{eq} is the diameter of the sphere equivalent to the agglomerate, i.e., with the same volume. Unsteady simulations were also carried out at the higher Reynolds number to compare the difference between the drag coefficients. Despite presenting the unsteady turbulent wake profile, the drag coefficient obtained did not present significant deviations, so we chose the steady simulations to reduce computational efforts. The boundary conditions were set to the no-slip condition for the sphere walls and specified shear for the domain walls.

Table 3. Inlet velocity of the flow for the Reynolds numbers tested.

Reynolds	Velocity (m/s)		
(-)	3 spheres	4 spheres	5 spheres
1	0.000070	0.000064	0.000059
5	0.000350	0.000318	0.000295
10	0.000700	0.000636	0.000590
30	0.002100	0.001907	0.001770
50	0.003500	0.003178	0.002950
80	0.005600	0.005085	0.004720
100	0.007000	0.006356	0.005900
300	0.021002	0.019069	0.017702
500	0.035003	0.031781	0.029503
800	0.056005	0.050849	0.047205
1000	0.070007	0.063562	0.059006
1300	0.091009	0.082631	0.076708
1500	0.105010	0.095343	0.088509

Despite the SIMPLE-based algorithms presenting lower computational effort [37], we chose the PISO algorithm since it presents greater stability, requiring fewer iterations, generating a faster convergence, and, consequently, less processing time [38,39].

The spatial discretization was set to the least-squares cell-based method for gradients, *PRESTO*! scheme for pressure and second-order upwind scheme for energy, momentum, and turbulence equations to solve the problem of underestimation of turbulent kinetic energy and its dissipation rate, as suggested in previous studies [12,13].

Turbulence closure models

The choice of the turbulence models was based on their characteristics and ability to solve specific problems presented by the complex geometry of the meshes generated. Since one of the focuses in the present study stands on analyzing the drag coefficient in an agglomerate of particles, predicting the flow in the boundary layer is essential. The Spalart-Allmaras model, a one-equation-based model, fits in this type of flow since it was developed to study the flow in the boundary layers of airfoils [28]. Two other models also developed to represent this zone are the transition models SST k-ω and the Langtry-Menter k-ω [22]. The first one is a two-equation-based model that solves the equation of the turbulent kinetic energy, k, for the flow far from the wall and, for the boundary layer, weights the influence of the turbulent kinetic turbulence and the specific turbulence dissipation rate, ω, using blending functions. The second is based on the k-ω. However, it implements two transport equations, one to solve the intermittency, γ, and one to solve the transition momentum-thickness Reynolds number, $\widetilde{Re}_{\theta t}$, to better represent profiles with strong adverse pressure gradients [32,33,40].

We also tested turbulence models developed to represent wide ranges of Reynolds numbers. With a low computational cost, the k-ε model was developed to solve several engineering in a wide range of Reynolds numbers [41]. This model has the characteristic of modeling the near-wall region and solving the transport equation for the outer region of the boundary layer. We chose to use the RNG k-ε, an improvement of the k-ε developed to solve problems where the flow presents a highly swirling profile [31]. The Reynolds stress model was another model tested in this study, with similar characteristics but more robust. The main difference in this seven-equation-based model that leads to its robustness is the addition of six transport equations, one for each independent Reynolds stress, to the solution for the dissipation equation, ε, and its anisotropic treatment [34]. The following items are reserved for modeling the transport equations of each turbulence model presented.

i. Spalart-Allmaras Model

The Spalart-Allmaras is a one-equation model that solves a viscosity-like variable's transport equation. $\tilde{\nu}$, also referred to as the Sparlat-Allmaras variable. The model is given by Eq. (5):

$$\frac{\partial \bar{\nu}}{\partial t} + \frac{\partial\left(u_j \bar{\nu}\right)}{\partial x_j} = \frac{1}{\sigma}\frac{\partial}{\partial x_j}\left[\left(\nu + \bar{\nu}\right)\frac{\partial \bar{\nu}}{\partial x_j}\right] + \frac{c_{b2}}{\sigma}\frac{\partial \bar{\nu}}{\partial x_j}\frac{\partial \bar{\nu}}{\partial x_j} + c_{b1}\bar{S}\bar{\nu} - c_{\omega 1} f_{\omega}\left(\frac{\bar{\nu}}{d}\right)^2 \tag{5}$$

where $\tilde{S}$ is the production of turbulent viscosity, c_{b1}, c_{b2}, c_{w1}, f_w, and σ are the model's closure coefficients and auxiliary relations, better described by Spalart and Allmaras [30].

ii. RNG k-ε Model

The RNG k-ε model uses the renormalization group theory to improve the Standard k-ε model, which models the turbulence kinetic energy, k, and the turbulence dissipation rate, ε, given by Eqs. (6) and (7), respectively,

$$\frac{\partial k}{\partial t}+\frac{\partial\left(u_i k\right)}{\partial x_i}=\frac{\partial}{\partial x_j}\left[\left(\nu+\frac{\nu_t}{\sigma_k}\right)\frac{\partial k}{\partial x_j}\right]+P_k-\varepsilon \tag{6}$$

$$\frac{\partial \varepsilon}{\partial t}+\frac{\partial\left(u_i \varepsilon\right)}{\partial x_i}=\frac{\partial}{\partial x_j}\left[\left(\nu+\frac{\nu_t}{\sigma_\varepsilon}\right)\frac{\partial \varepsilon}{\partial x_j}\right]+C_{1\varepsilon}\frac{\varepsilon}{k}P_k-C_{2\varepsilon}^{*}\frac{\varepsilon^2}{k} \tag{7}$$

where P_k is the production term of the turbulent kinetic energy [31].

iii. SST k-ω Model

The SST k-ω model modifies low-Reynolds number effects, compressibility, and shear flow spreading. The model is based on modeling transport equations for turbulence kinetic energy and the specific dissipation rate, given by Eqs. (8) and (9), respectively.

$$\frac{\partial k}{\partial t}+\frac{\partial\left(u_i k\right)}{\partial x_i}=\frac{\partial}{\partial x_j}\left[\left(\nu+\sigma_k \nu_t\right)\frac{\partial k}{\partial x_j}\right]+P_k-\beta^{*}k\omega \tag{8}$$

$$\frac{\partial \omega}{\partial t}+\frac{\partial\left(u_i \omega\right)}{\partial x_i}=\frac{\partial}{\partial x_j}\left[\left(\nu+\sigma_\omega \nu_t\right)\frac{\partial \omega}{\partial x_j}\right]+ 2\left(1-F_1\right)\sigma_{\omega 2}\frac{1}{\omega}\frac{\partial k}{\partial x_i}\frac{\partial \omega}{\partial x_i}+\alpha\mathcal{S}^2-\beta\omega^2 \tag{9}$$

where F_1 is the blending function, α, β, and σ refer to the closure coefficients of the model [32].

iv. Langtry-Menter SST k-ω Model

Modeled similarly to the SST k-ω model presented previously, the Langtry-Menter model implements two transport equations to solve the intermittency and the turbulent transition Reynolds number, given by Eqs. (10) and (11), respectively.

$$\frac{\partial \gamma}{\partial t}+\frac{\partial\left(u_i \gamma\right)}{\partial x_j}=\frac{\partial}{\partial x_j}\left[\left(\nu+\frac{\nu_t}{\sigma_f}\right)\frac{\partial \gamma}{\partial x_j}\right]+P_{\gamma 1}-E_{\gamma 1}+P_{\gamma 2}-E_{\gamma 2} \tag{10}$$

$$\frac{\partial \bar{\mathrm{Re}}_{\theta t}}{\partial t}+\frac{\partial\left(u_j \bar{\mathrm{Re}}_{\theta t}\right)}{\partial x_j}=\frac{\partial}{\partial x_j}\left[\sigma_{\theta t}\left(\nu+\nu_t\right)\frac{\partial \bar{\mathrm{Re}}_{\theta t}}{\partial x_j}\right]+P_{\theta t} \tag{11}$$

where $P_{\gamma 1}$ and $E_{\gamma 1}$ are the transition sources, $P_{\gamma 2}$ and $E_{\gamma 2}$ are the destruction sources and $P_{\theta t}$ is a source term [33].

v. Reynolds Stress Model

The RSM consists of modeling the Reynolds stresses, represented by the tensor τ, and the turbulence dissipation rate, ε [22]. The exact transport equation of the Reynolds stresses, in tensorial notation, is given by Eq. (12).

$$\frac{\partial \tau_{ij}}{\partial t}+\bar{u_k}\frac{\partial \tau_{ij}}{\partial x_k}=\frac{\partial}{\partial x_k}\left[\frac{\nu_t}{\sigma_k}\frac{\partial \tau_{ij}}{\partial x_k}\right]+P_{ij}-C_1\frac{\varepsilon}{K}\left[\tau_{ij}-\frac{2}{3}\delta_{ij}K\right]- C_2\left[P_{ij}-\frac{2}{3}\delta_{ij}P\right]-\frac{2}{3}\delta_{ij}\varepsilon \tag{12}$$

where the turbulence production terms P_{ij} are given by

$$P_{ij}=-\left[\tau_{ik}\frac{\partial \bar{u_j}}{\partial x_k}+\tau_{jk}\frac{\partial \bar{u_i}}{\partial x_k}\right] \tag{13}$$

where P is the fluctuation kinetic energy production and ν_t the turbulent kinematic viscosity.

The transport equation for turbulence dissipation rate, ε, is given by

$$\frac{\partial \varepsilon}{\partial t}+\bar{u_j}\frac{\partial \varepsilon}{\partial x_j}=\frac{\partial}{\partial x_j}\left[\left(\nu+\frac{\nu_t}{\sigma_\varepsilon}\right)\frac{\partial \varepsilon}{\partial x_j}\right]-C_{\varepsilon 1}\frac{\varepsilon}{K}\tau_{ij}\frac{\partial \bar{u_i}}{\partial x_j}-C_{\varepsilon 2}\frac{\varepsilon^2}{K} \tag{14}$$

where $K=\frac{1}{2}\overline{u_i' u_i'}$ is the fluctuation of kinetic energy [34].

Drag coefficient correlation modelling

For several applications in industry, the drag force is the main acting force on a particle in the opposite direction of the particle motion.

Studies generally consider the most influential parameters to estimate the drag coefficient, i.e., the particle Reynolds number, shape, orientation, and particle-to-fluid density ratio. Also, secondary parameters, such as secondary motions, turbulence, and particle/fluid acceleration, are the focus of studies [11,16,17,20,42–45].

The present study considered five correlations observed in the literature that consider only the main parameters, as follows. Four of them consider the Reynolds number and shape parameters, such as the sphericity, circularity, and flatness of the agglomerate [11,16,17,19], while one of them uses the orientation of the agglomerate to estimate two different shape parameters [18].

Haider and Levenspiel model

The study of Haider and Levenspiel [16] was the first to propose that the drag coefficient is a function of

the Reynolds number and sphericity for both spherical and nonspherical particles. Also, the Reynolds number should be calculated using an equivalent diameter, d_{eq}, corresponding to the diameter of a sphere with the same volume of the particle tested. They proposed that drag correlations could be written as

$$C_D = \frac{24}{\mathrm{Re}}\left(1 + A\mathrm{Re}^B\right) + \frac{C}{1 + \frac{D}{\mathrm{Re}}} \tag{15}$$

where A, B, C, and D are parameters given as a function of the sphericity Φ and are applicable for $Re < 2.5 \cdot 10^4$ for isometric particles [16], such as the one proposed in the present study.

Ganser model

The model proposed by Ganser [17] adapts the Haider & Levenspiel model, introducing two other shape-dependent parameters: Newton's and Stokes' parameters, k_N and k_S, respectively, and is given by Eq. (16).

$$C_D = \left(24\frac{k_S}{\mathrm{Re}}\right)\left[1 + 0.1118\left(\mathrm{Re}\frac{k_N}{k_S}\right)^{0.6567}\right] + \frac{0.4305 k_N}{1 + \frac{3305}{\mathrm{Re}\,k_N / k_S}} \tag{16}$$

where k_N and k_S are functions of the sphericity, Φ, and the model is applicable for $Re < 3 \cdot 10^5$ if k_N and k_S are known. The literature presents several proposals to estimate these parameters, such as the Tran-Cong et al. [11], Hölzer and Sommerfeld [18], and Bagheri and Bonadonna [19], tested in this study and presented in the following sections.

Tran-Cong *et al.* model

The model proposed by Tran-Cong *et al.* [11] considers that the drag coefficient is a function not only of the Reynolds number but also of the ratio between the surface-equivalent-sphere diameter, d_A, and the volume-equivalent-sphere diameter, d_{eq}, referred to as flatness, and the circularity, c. The correlation is given by Eq. (17).

$$C_D = \left(\frac{24}{\mathrm{Re}}\frac{d_A}{d_{eq}}\right)\left[1 + \frac{0.15}{\sqrt{c}}\left(\frac{d_A}{d_{eq}}\mathrm{Re}\right)^{0.687}\right] + \frac{0.42\left(\frac{d_A}{d_{eq}}\right)^2}{\sqrt{c}\left[1 + 4.25 \cdot 10^4\left(\frac{d_A}{d_{eq}}\mathrm{Re}\right)^{-1.16}\right]} \tag{16}$$

for the ranges of variables

$0.15 < Re < 1500$,

$0.80 < {}^{d_A}/_{d_{eq}} < 1.50$ and $0.4 < c < 1.0$ [11].

Hölzer & Sommerfeld model

The drag coefficient can also be modeled using the theoretical and experimental correlation for drag in the Stokes region [15], as proposed by Hölzer and Sommerfeld [18]. Their model has its base on the proposal of Leith [15] and Ganser [17] for C_D in the Stokes region, including shape and orientation-dependent terms and the Reynolds number of the particle. The correlation is given by Eq. (18).

$$C_D = \frac{8}{\mathrm{Re}}\frac{1}{\sqrt{\phi_{\parallel}}} + \frac{16}{\mathrm{Re}}\frac{1}{\sqrt{\phi}} + \frac{3}{\sqrt{\mathrm{Re}}}\frac{1}{\phi^{3/4}} + 0.421^{0.4(-\log\phi)^{0.2}}\frac{1}{\phi_{\perp}} \tag{18}$$

where the sphericity, Φ, represents the ratio between the surface area of the volume-equivalent-sphere and that of the particle, the crosswise sphericity, $\phi_{\perp}$, is the ratio between the cross-sectional area of the volume-equivalent-sphere and the projected cross-sectional area of the particle and the lengthwise sphericity, $\phi_{\parallel}$, is the ratio between the cross-sectional area of the volume-equivalent-sphere and the difference between half the surface area and the mean projected longitudinal cross-sectional area of the particle. The correlation is applicable over the entire range of Reynolds numbers up to the critical Reynolds number [18].

Bagheri & Bonadonna model

However, this model is also derived from the Ganser model, which accounts for more accurate and easier shape descriptors rather than sphericity [19]. Here, the form factors, F_S and F_N, are functions of the volume-equivalent-sphere, and three size parameters: the longest, the intermediate, and the shortest lengths of the particle, L, I, and S, respectively. The correlation is given by Eq. (19):

$$C_D = \left(24\frac{k_S}{\mathrm{Re}}\right)\left[1 + 0.125\left(\mathrm{Re}\frac{k_N}{k_S}\right)^{2/3}\right] + \frac{0.46 k_N}{1 + \frac{3305}{\mathrm{Re}\,k_N / k_S}} \tag{19}$$

where the drag corrections, k_N and k_S, are functions of the form factors F_N and F_S.

RESULTS AND DISCUSSION

Grid refinement near the agglomerate walls

To analyze if the turbulence models are applicable, it is important to evaluate the y^+ since the flow near the walls is a relevant region in the study of the drag coefficient. Turbulence models that do not use wall functions need better refinement near walls since their y^+ shall be lower than 1 [40], whereas, in turbulence models that use wall function, the value depends on the type of function treatment. The

Enhanced-Wall functions should be used for values as low as 3 [28]. Since the value of y^+ increases as the velocity of the flow increases, it is necessary to analyze only the highest velocity, i.e., for Reynolds number of 1500.

Simulations presented good results. In general, the y^+ was below 1 for over 99.5% of the elements in the walls of the agglomerates. The RNG k-ε simulations obtained the worst values, where the percentage of elements below 1 varied between 97 and 98%. The values confirm that the meshes are fine enough near the agglomerates and it is reasonable to use the Enhanced-Wall functions for the RSM and RNG k-ε turbulence models and fine enough to use k-ω-based models and the Spalart-Allmaras model.

However, wall functions are approximations for zones near the walls, leading the RSM and RNG k-ε turbulence models to lower efficiency in representing the flow surrounding the agglomerate and models without wall functions. Also, RSM and RNG k-ε turbulence models are expected to correctly represent the flow far from the agglomerates, like the models without wall functions.

Statistical analysis of results – Comparison between simulations and empirical correlations

In Figure 6, we observe three models that present promising curves where simulations are correlated: the Haider and Levenspiel model, the Bagheri and Bonadonna model, and the Tran-Cong model. However, it is important to statistically confirm which model better fits the results obtained in the simulation. The criterion used was the method known as the root-mean-square error (RMSE), calculated by Eq. (3), and which values are presented in Table 4.

Table 4. Root-mean-square error of the turbulence models compared to drag coefficient models.

Agglomerate	Drag coefficient model	Turbulence model				
		RSM	RNG k-ε	SST k-ω	Langtry-Menter	Spalart-Allmaras
3 spheres	Haider & Levenspiel	1.8179	1.5133	1.5568	1.5393	1.2398
	Ganser	2.6035	2.3056	2.3283	2.3185	2.0013
	Tran-Cong *et al.*	2.4351	2.1501	2.1497	2.1484	1.8192
	Hölzer & Sommerfeld	2.3887	2.0893	2.1123	2.1031	1.7805
	Bagheri & Bonadonna	2.4090	2.1157	2.1537	2.1377	1.8560
4 spheres	Haider & Levenspiel	0.7242	0.6639	0.7703	0.9211	0.7223
	Ganser	1.0941	1.0637	1.1173	1.3804	1.0384
	Tran-Cong *et al.*	0.3172	0.3377	0.3112	0.2489	0.3697
	Hölzer & Sommerfeld	0.8041	0.7835	0.8214	1.1276	0.7378
	Bagheri & Bonadonna	0.5447	0.5376	0.5565	0.3474	0.6151
5 spheres	Haider & Levenspiel	1.6936	1.6389	1.7408	1.7140	1.5265
	Ganser	2.4442	2.3938	2.4838	2.4670	2.2444
	Tran-Cong *et al.*	1.0611	1.0464	1.0803	1.0777	0.8359
	Hölzer & Sommerfeld	1.9699	1.9435	1.9937	1.9836	1.7369
	Bagheri & Bonadonna	1.0511	0.9939	1.1009	1.0805	0.9061

Here, we observe that, in most cases, the Tran-Cong model presents lower RMSE for the agglomerates of four and five spheres. An exception is observed for the agglomerate of three spheres, where the Haider and Levenspiel model presented the lower RMSE for all turbulence models tested.

Still analyzing Figure 6, lower deviations of the Haider and Levenspiel model for Reynolds numbers between 1 and 100 were observed. The drag coefficient presents higher values for this range, which interferes the most in the RMSE, compared to the drag values for Reynolds above 100. This behavior generates the distortion that leads to statistical inferring that the Haider and Levenspiel model can better represent the drag coefficient in the agglomerate of 3 spheres. Now, considering the range between 1 and 1500, the plot shows that the Tran-Cong model presents the best agreement with simulation data, while the Haider and Levenspiel present good agreement only for lower Reynolds numbers.

Analysis of the turbulence models

To understand the influence of the turbulence models on the drag coefficient prediction, we first observed the behavior of the streamlines of the flow

surrounding the agglomerate to determine which one better represents three relevant regions of the flow: the boundary layer, the flow far from the walls of the particle and the wake region in the rear of the agglomerates. To infer if the simulation results are consistent, we compared with the literature correlations to observe if simulations follow a trend. At last, we compared the results of the turbulence models with the correlation that better represented the trend of the simulations to find which turbulence model presents lower deviations from the predicted by the correlation.

Before analyzing the drag results, it is relevant to observe if the flow profile corresponds to the expectations from the literature. Militzer *et al.* [46] stated that a particle's aspect ratio substantially interferes with where the separation begins, and the size of the recirculation wake. According to them, particles with similar aspect ratios present similar flow profiles. The flow profile past a sphere is well-known, and since the particle agglomerates are composed of spheres, the flow profile is expected to behave similarly [47]. To compare the velocity profiles, we chose the inlet velocity to reach Re = 1000, where the flow is turbulent, and the vortex street in the rear of the agglomerate is considered fully turbulent [19,35,47]. Figures 3 to 5 present the velocity streamlines for agglomerates of three, four, and five particles, respectively, according to the turbulence models. Comparing the models with wall functions, due to its anisotropic treatment, the RSM is more capable of representing the velocity in the rear of the particle agglomerates in the wake region than the RNG k-ε. However, both do not represent the profile as well as the turbulence models without wall functions. Such behavior confirms the expectation since they model the boundary layer zone to represent it instead of solving the transport equations around the particle.

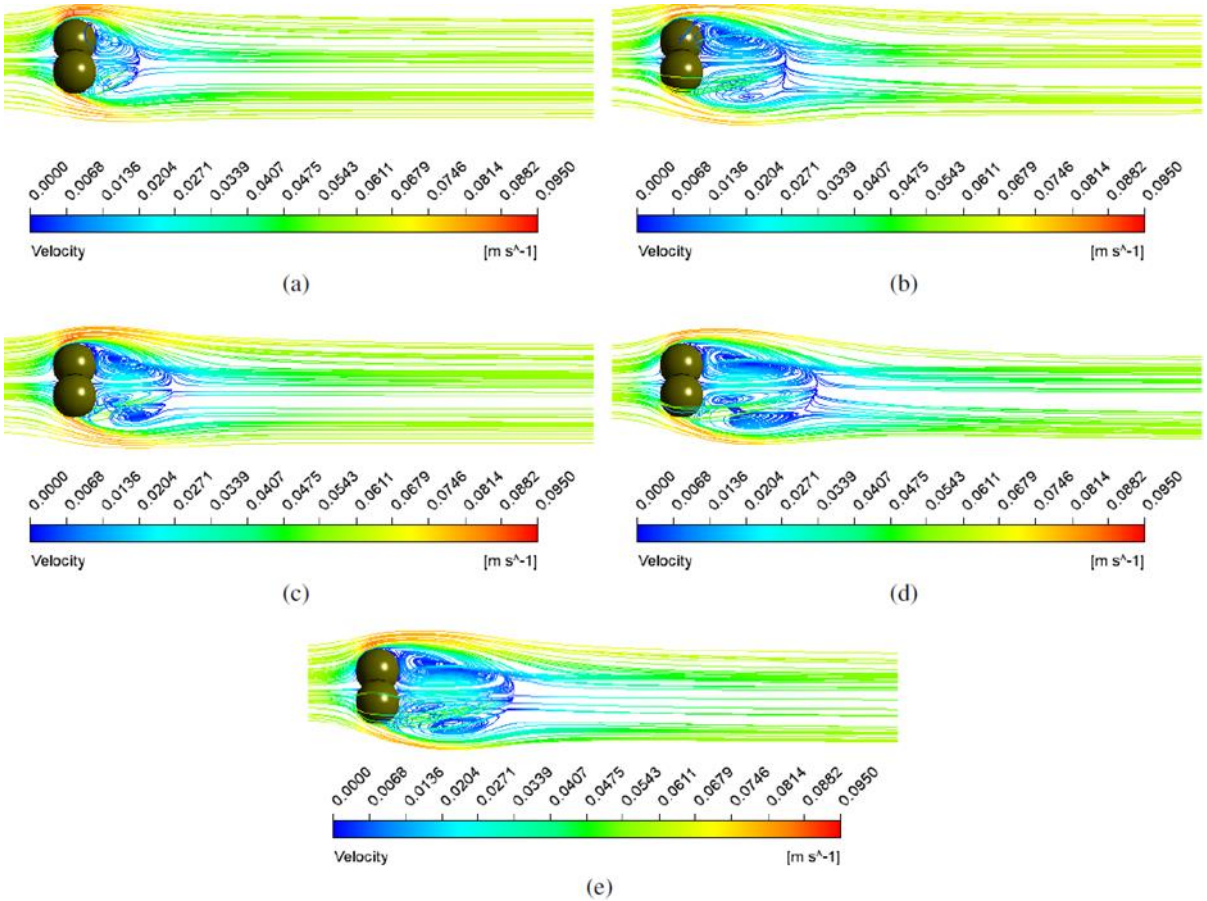

Figure 3. From left to right and top to bottom: velocity streamlines for Re = 1000 in the agglomerate of three particles using the RNG k-ε, RSM, Langtry-Menter, Spalart-Allmaras, and SST k-ω turbulence models.

The velocity streamlines obtained by the SST k-ω model, seen in Figures 3e, 4e, and 5e, better represent the flow profile near the agglomerate walls, i.e., the viscous effects ahead of the particle becoming less important than the inertial effects [19,48]. Such behavior leads to a separation of the flow from the particle at the so-called separation location, and the fluid's inertia is large enough that the fluid cannot follow the path around the rear of the particle. This effect results in a separation bubble after the particle [47] in a region where the boundary layer thickens rapidly in rising pressure, generating a backflow.

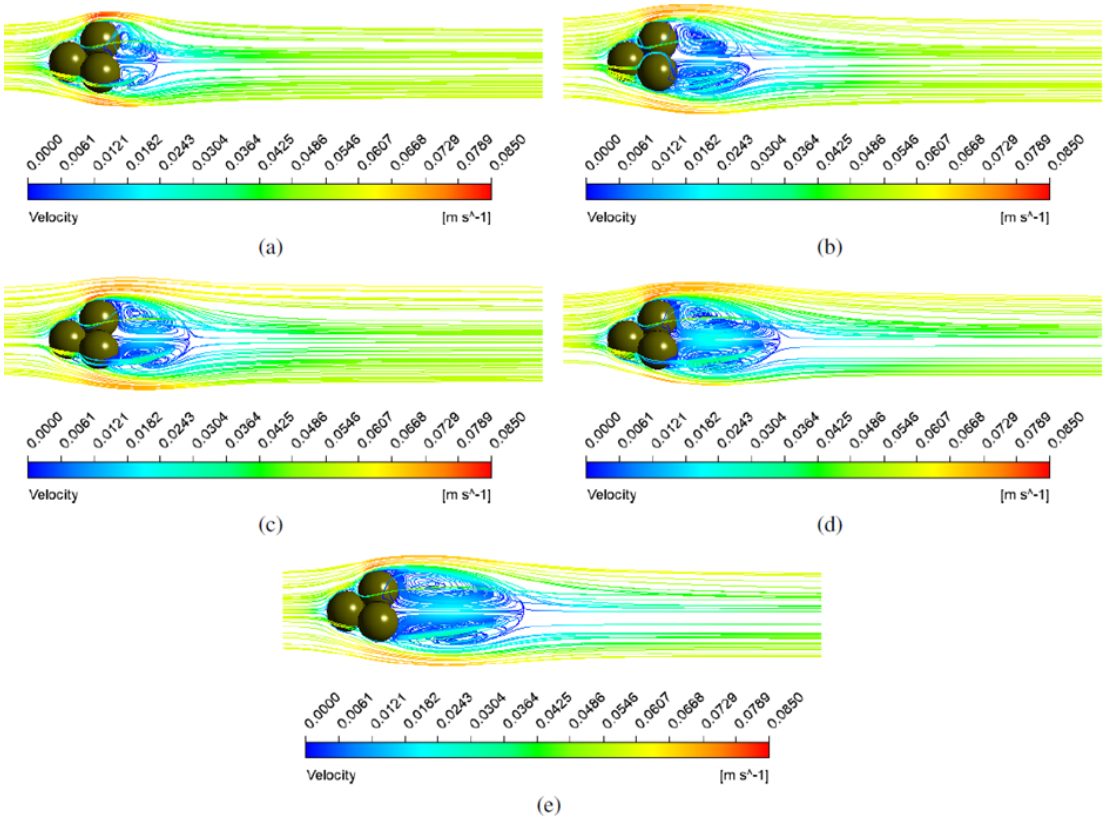

Figure 4. From left to right and top to bottom: velocity streamlines for Re = 1000 in the agglomerate of four particles using the RNG k-ε, RSM, Langtry-Menter, Spalart-Allmaras, and SST k-ω turbulence models..

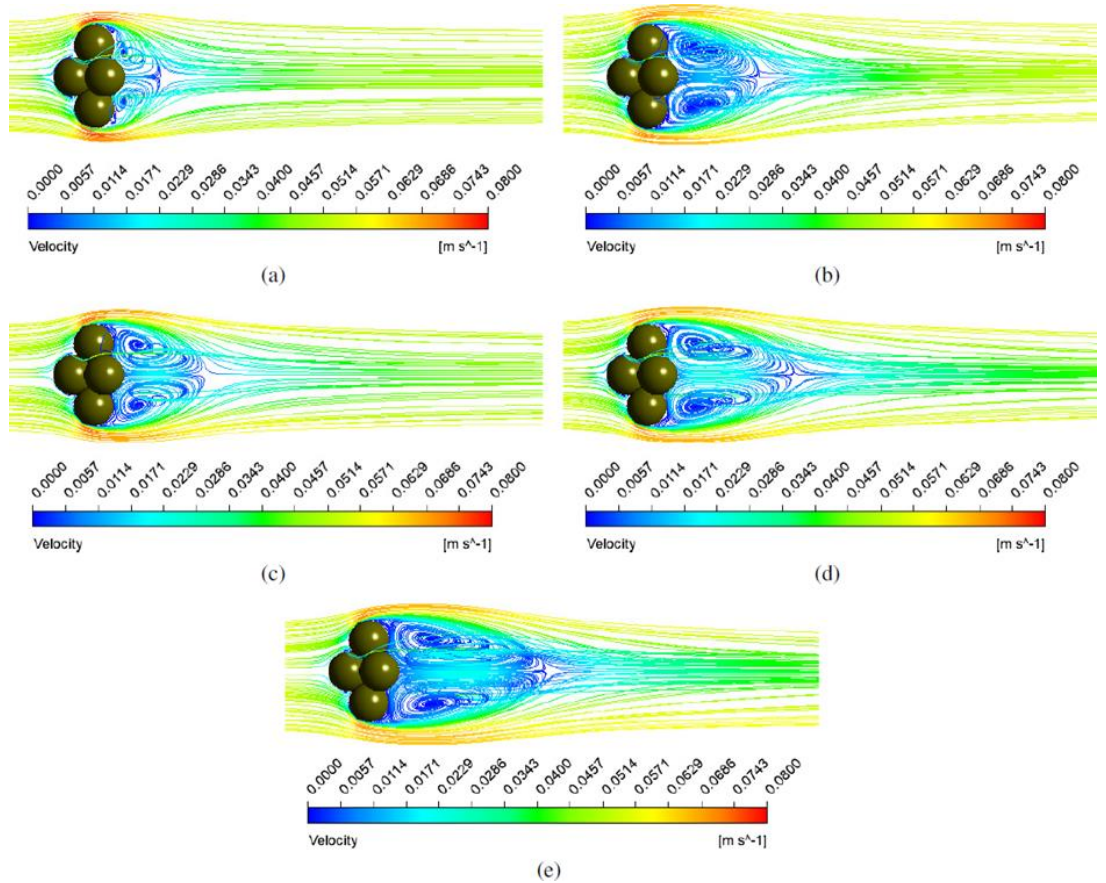

Figure 5. From left to right and top to bottom: velocity streamlines for Re = 1000 in the agglomerate of five particles using the RNG k-ε, RSM, Langtry-Menter, Spalart-Allmaras, and SST k-ω turbulence models.

In the moderate Reynolds number range, e.g., the tested in this study, as the Reynolds number increases, the backflow profile increases in the rear of the particle to regions far from the particle. The SST k-ω model better represented the recirculating profile in the rear of the agglomerates for all the particle agglomerates. However, the separation is unclear for larger Reynolds numbers by order of Re = 105 since it occurs together with the wake region [48]. Consequently, the results of the drag coefficient estimated by simulations using such a model tend to obtain, in general, lower deviations from the empirical model of drag coefficient, as presented in Figure 7.

To find a correlation that better represents the trends of the drag coefficient estimated by simulations, we compared the results of the simulations using the Spalart-Allmaras and the SST k-ω turbulence models with five drag coefficient correlations present in the literature [11,16–19]. The comparisons are presented in Figure 6.

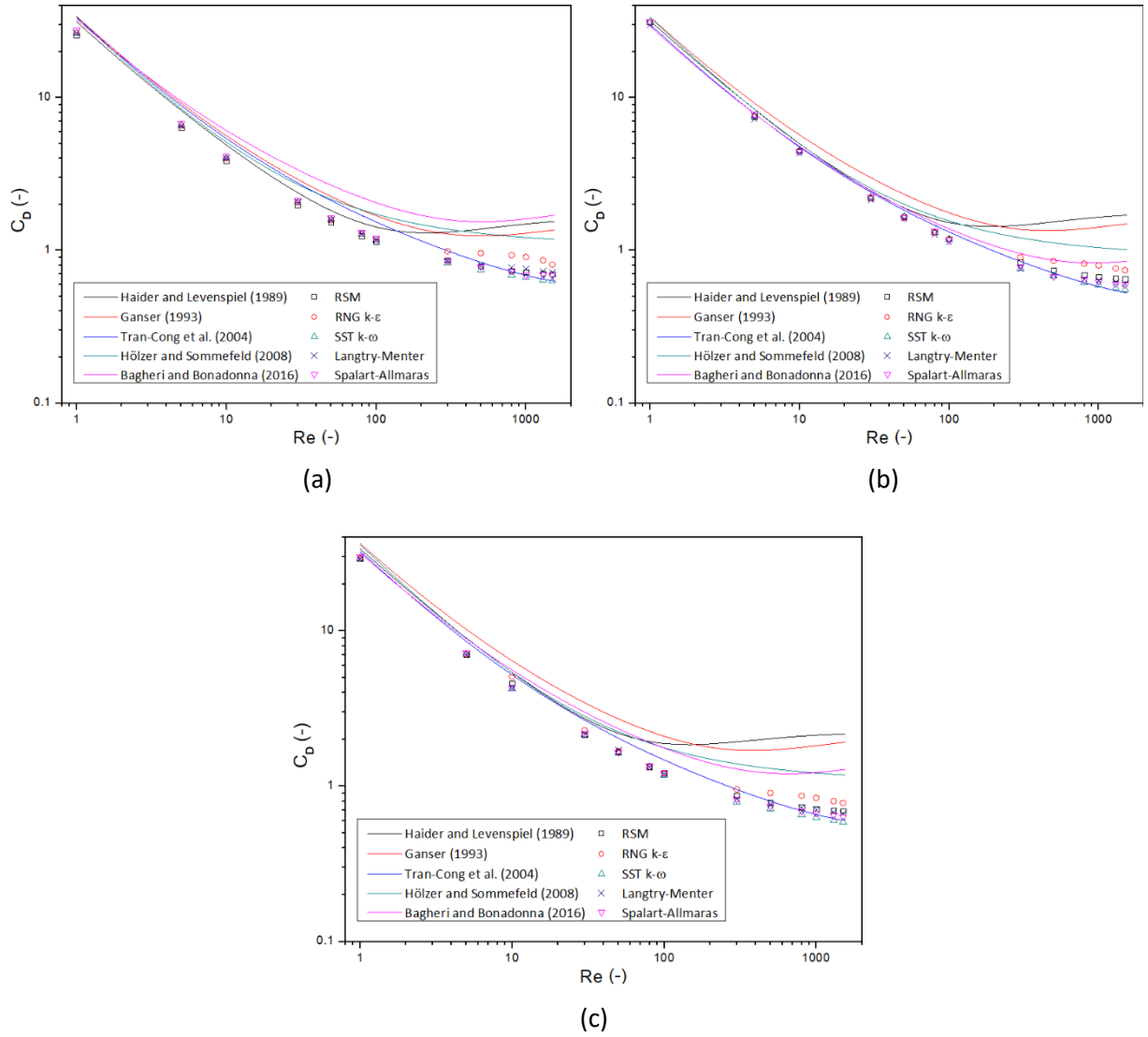

Figure 6. Comparison between predictions of the experimental drag models tested and the simulations data using different turbulence models for agglomerates: a) three particles, b) four particles, and c) five particles.

In a first analysis, one can infer that the simulations correlate better to the Tran-Cong *et al.* [11] model for the three agglomerates along the range of Reynolds numbers tested. An exception occurs in the agglomerate of three particles, as seen in Figure 6a, where the Haider and Levenspiel [16] model has a slightly better representation for Reynolds numbers lower than 10 and a significantly better representation for Reynolds numbers between 10 and 100. Since the range of Reynolds numbers is wide, the logarithm scale

distorts the perception of the deviations.

To reduce the distortion, the relative deviations along the Reynolds number were plotted for the Tran-Cong *et al.* [11] model to analyze if the model represents the simulations and find the turbulence model that presents lower deviations from the correlation. Analyzing the plot of the deviations for the agglomerate of three particles (Figure 7a), the range from 1 to 100 is not so distant from the error of 12% observed in the literature [11]. Also, considering the wide range of Reynolds numbers to which the models are applicable, deviations between ±25% are considered low.

For lower velocities, the flow still follows the curvature of the particle and, consequently, the path around the rear of the particle, for all turbulence models, presented a similar flow profile, leading to similar values for the drag coefficient. As the velocity increases, the edge of the boundary layer gets far from the particle; the boundary layer separation location gets far from the stagnation point, and the turbulence models that use wall functions present difficulties in representing the backflow and wake regions after the particles. Consequently, the RNG k-ε and RSM do not follow the trends observed by the other three turbulence models. The RSM is closer to the trends observed due to its robustness, compared to the RNG k-ε, but in Figures 3 to 5 we observe that the RSM also does not represent so well the velocity profile expected.

Figure 7 shows the deviation of the drag coefficient obtained by simulations compared to the correlation of Tran-Cong *et al.* [11] for the agglomerates in the applicable range of the Reynolds number of the model. The figure shows a trend for all agglomerates, where the deviation slightly and negatively increases as the Reynolds number increases in the range of low Reynolds numbers, from 1 to 100, and for the moderate Reynolds numbers range, from 100 to 1500, the deviation slope is positive and higher.

For Reynolds numbers between 1 and 100, turbulence models presented similar deviations for each of the three agglomerates studied since it corresponds to the laminar regime presenting unseparated flow. The variation between the models results from the different values of the closure constants present in each turbulence model. The deviations begin to diverge for Re ≥ 300, where the flow is transitioning to the turbulence region, and the vortices are becoming present. Figure 7 shows that the values obtained are lower than the predicted by equations, by the magnitude of -25%, -10%, and -18% for the agglomerates of three, four, and five particles, respectively.

As the velocity increases, the gradient of the deviations is positive. However, the slope of the curves for Spalart-Allmaras and SST k-ω models are smoother, and for Reynolds numbers above 1000, the deviations for the SST k-ω present a trend to converge to a value between ± 5%, according to the agglomerate studied. The increase of kinetic turbulence explains so turbulence models that better capture effects in the boundary and outer layers can better estimate the drag force acting in the agglomerate. The streamlines presented in Figures 3 to 5 show that the SST k-ω better represents these effects, followed by the Spalart-Allmaras model, confirming the ability of this model to estimate the drag coefficient in particle agglomerates.

For Reynolds numbers between 10 and 100, the deviations are constant or close to constant – in the case of the agglomerate of four particles. It corresponds to the range where the von Kármán vortex street starts to appear in a laminar flow, depending on the body's shape and the fluid's kinematic viscosity. The deviations varied from -13 to -28% in the agglomerate of three particles, -6 to -14% in the agglomerate of four particles, and -13 to -20% in the agglomerate of five particles. However, simulations with Reynolds numbers below 10 have drag coefficients closer to the estimated correlation.

The symmetry of the agglomerate is an important variable to consider in the analysis. In numerical simulations, symmetric geometries are easier to generate meshes with good refinement quality in the boundary layer separation region. It leads to better results and reduces errors of pressure and velocity fields, mainly near walls, where the drag and lift are computed. The capacity to predict the flow profile and the adverse pressure gradient is correlated with the geometry since the interference of the effect between the spheres of each agglomerate of particles is reduced as the symmetry of the agglomerate increases. Physically, it means that symmetric geometries tend to generate symmetric streamlines, which are easier to be calculated by turbulence models. Such behavior is well presented in Figure 7, where the agglomerate of four particles has lower deviations since its symmetry is closer to a single sphere – the most symmetrical shape for spheric particle agglomerates – followed by the agglomerate of five and three particles.

Still analyzing the geometry of the agglomerates, it is possible to see that they generate curvature in the streamlines as we increase the velocity, which directly affects the turbulence and, consequently, the flow profile. The curvature effect can highly decrease the Reynolds stress normal to the wall as the ratio between the boundary layer thickness and the radius increases. Such a decrease reaches up to 50% for a ratio of 0.03 [49].

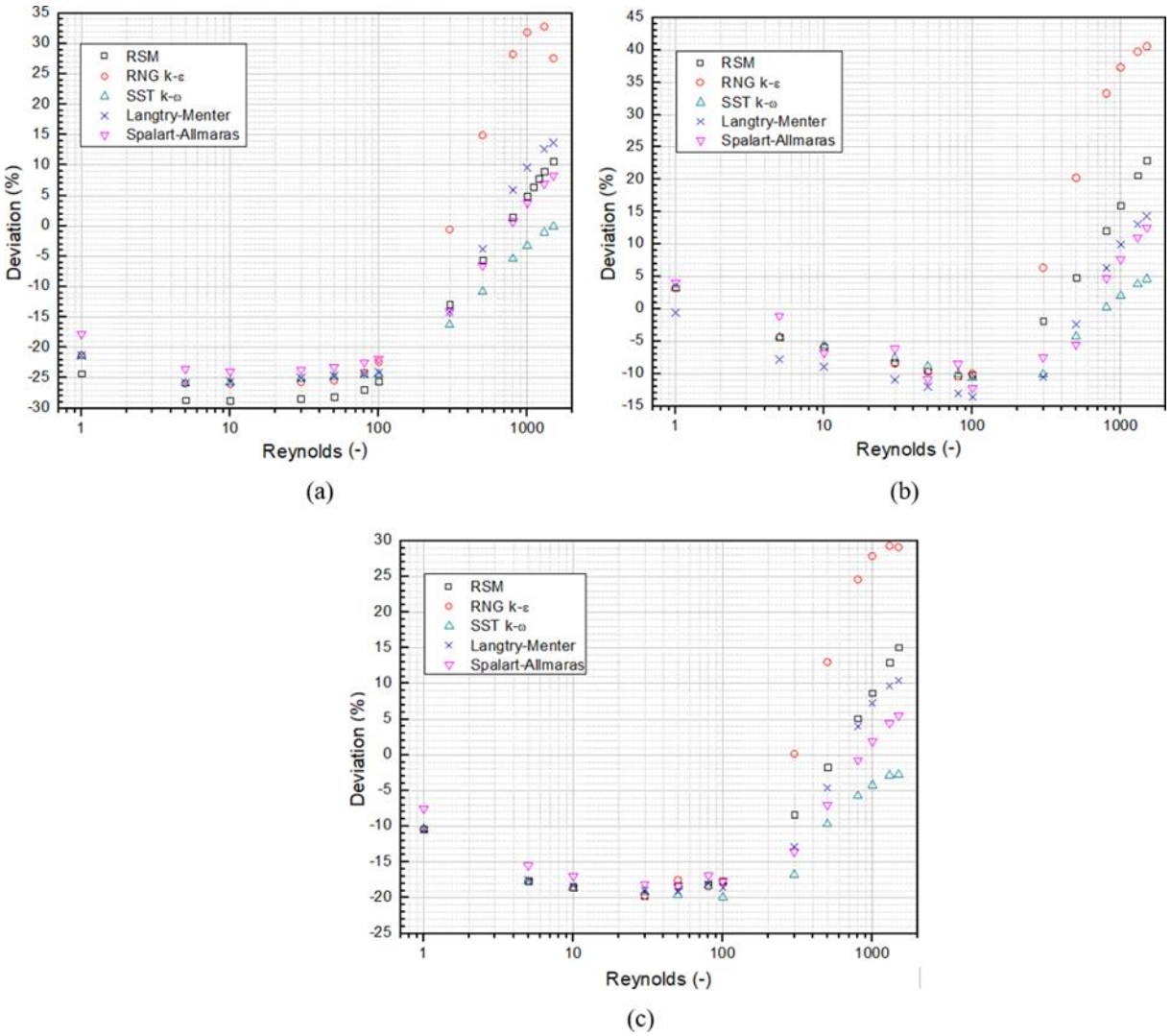

Figure 7. From left to right and top to bottom: deviations of simulated data from the Tran-Cong model for the agglomerate of three, four, and five particles.

The simulations confirmed the expectations of better results when the curvature effects are considered using the Spalart-Allmaras and both SST k-ω-based models [50].

Since the geometry in the agglomerate of four particles is closer to a single sphere, the deviations are lower for the turbulence models that do not use wall functions. Turbulence models such as the RSM and RNG k-ε are accurate in computing the field far from the agglomerate; however, the near-wall regions and boundary layers are not correctly presented, with difficulties in representing the adverse pressure gradient of the agglomerate in a greater area, lacking the quality to compute the drag coefficient, increasing the deviation. It is related to the fact that the wall-functions effects are more influential in the turbulence model than the curvature effects present in a sphere, so the pressure and velocity fields are not well represented near the walls as in the other turbulence models.

The results of this study demonstrate that the utilization of the steady formulation approach yields accurate estimations of the drag coefficient. Furthermore, the turbulence model plays a crucial role in effectively modeling the problem, not only for estimating the drag coefficient but also for accurately predicting the flow profile in regions characterized by separation and recirculating wakes, particularly in flows with higher Reynolds numbers. The implementation of RANS turbulence models that calculate the flow field near the particles instead of relying on wall-function modeling exhibited robustness in representing the presented problem. Moreover, these models agreed more closely with experimental correlations for drag estimation in particle agglomerates.

The simplifications proposed in this study offer a significant advantage, primarily through the reduction of computational time required to obtain results. Consequently, this reduction allows for more simulations to be conducted, facilitating a more detailed

presentation of the drag coefficient curve and enabling the proposal of new correlations. By incorporating these findings into future research, it is possible to advance the understanding of drag coefficient estimation and develop improved correlations for industrial-scale problems.

CONCLUSION

The present study carried out steady simulations of three irregularly-shaped particle agglomerates composed of spherical particles surrounded by water. The drag coefficient at different inlet conditions was obtained for five different turbulence models and compared with five correlations in the literature to predict the drag coefficient in agglomerates to understand which numerical setup better represents the flow. The proposed methodology presented a good agreement with experimental correlations of drag coefficient estimation, which is useful for reducing the time and computational efforts required to numerically obtain the drag acting in particle agglomerates and robustness to estimate the drag coefficient in higher Reynolds numbers. The main observations were:

Steady RANS turbulence models showed good agreement with the literature to estimate the drag coefficient on particle agglomerates, without the drawback of high computational cost seen in unsteady simulations, such as URANS, LES, DNS, or LBM.

The turbulence closure equations present a lower influence in the evaluation of flow fields for $1 \leq Re \leq 100$, so the drag coefficients estimated for each turbulence model are very similar.

The flow profile is better represented using turbulence models with no wall functions. Spalart-Allmaras and SST k-ω models could represent the flow near the particle agglomerates and far from its walls; however, the second one was more robust.

Steady formulation with the SST k-ω turbulence model can represent the flow for a wide range of Reynolds numbers with less computational effort.

Despite presenting the best agreement with Tran-Cong *et al.*[11] model, the numerical results presented relative deviations by a magnitude of -20%, mainly for lower Reynolds numbers, representing a good agreement since the average error of the empirical correlation is 10%.

Reduced computational costs make it possible to obtain more data so that further studies can focus on elaborating new accurate correlations to be scaled up for industry-scale problems.

The proposed numerical methodology was useful for initial tests and experimental validation.

NOMENCLATURE

A, B, C, D	Parameters of the Haider and Levenspiel drag model
A_P	Projected area
C	Circularity
C_D	Drag coefficient
$CDcorr$	Drag coefficient estimated by correlations
$CDsim$	Drag coefficient estimated by simulations
d_A	Surface-equivalent-sphere diameter
d_{eq}	Volume-equivalent-sphere diameter
F_D	Drag force
K	Fluctuation kinetic energy
K	Turbulence kinetic energy
k_N	Newton's parameter
k_S	Stokes' parameter
N	Total data in the sample studied
P_k	Production of turbulent kinetic energy
Re	Reynolds number
$Re\theta t$	Transition momentum thickness Reynolds number
T	Time
u_f	Fluid velocity
u_p	Particle velocity
xi	Value of the i^{th} data estimated by correlations
x_i	Value of the i^{th} data obtained by simulation
γ	Intermittency
δ	Percent deviation
ε	Turbulence dissipation rate
ν	Kinematic viscosity
ν_t	Turbulent kinematic viscosity
$\tilde{\nu}$	Spalart-Allmaras kinematic viscosity
ρ	Density
τ_{ij}	Specific Reynolds stress tensor
ϕ	Sphericity
$\phi_\perp$	Crosswise sphericity
$\phi_\parallel$	Lengthwise sphericity
ω	Specific turbulence dissipation

ACKNOWLEDGMENTS

This study was partly financed by the Coordination for the Improvement of Higher Education Personnel (CAPES) - Finance Code 001. The authors would like to thank also the National Council for Scientific and Technological Development (CNPq, grant number 140412/2020-4) for the financial support of this work.

REFERENCES

[1] J. Wang, W. Ge, J. Li, Chem. Eng. Sci. 63 (2008) 1553–1571. https://doi.org/10.1016/j.ces.2007.11.023.

[2] E.U. Hartge, L. Ratschow, R. Wischnewski, J. Werther, Particuology 7 (2009) 283–296.

https://doi.org/10.1016/j.partic.2009.04.005.

[3] A. Nikolopoulos, D. Papafotiou, N. Nikolopoulos, P. Grammelis, E. Kakaras, Chem. Eng. Sci. 65 (2010) 4080–4088. https://doi.org/10.1016/j.ces.2010.03.054.

[4] L. Wang, C. Wu, W. Ge, Powder Technol. 319 (2017) 221–227. https://doi.org/10.1016/j.powtec.2017.06.046.

[5] D. Gidaspow, in Multiphase Flow and Fluidization: Continuum and Kinetic Theory Descriptions with Applications, Academic Press, Cambridge (1994). ISBN: 978-0-122-82470-8.

[6] R.J. Hill, D.L. Koch, A.J.C. Ladd, J. Fluid Mech. 448 (2001) 213–241. https://doi.org/10.1017/S0022112001005948.

[7] R.J. Hill, D.L. Koch, A.J.C. Ladd, J. Fluid Mech. 448 (2001) 243–278. https://doi.org/10.1017/S0022112001005936.

[8] M.A. van der Hoef, R. Beetstra, J.A.M. Kuipers, J. Fluid Mech. 528 (2005) 233–254. https://doi.org/10.1017/S0022112004003295.

[9] R.C. Senior, C. Brereton, Chem. Eng. Sci. 47 (1992) 281–296. https://doi.org/10.1016/0009-2509(92)80020-D.

[10] K. Kuwagi, K. Takano, M. Horio, Powder Technol. 113 (2000) 287–298. https://doi.org/10.1016/S0032-5910(00)00311-9.

[11] S. Tran-Cong, M. Gay, E.E. Michaelides, Powder Technol. 139 (2004) 21–32. https://doi.org/10.1016/j.powtec.2003.10.002.

[12] D.A. Deglon, C.J. Meyer, Miner. Eng. 19 (2006) 1059–1068. https://doi.org/10.1016/j.mineng.2006.04.001.

[13] G.L. Lane, Chem. Eng. Sci. 169 (2017) 188–211. https://doi.org/10.1016/j.ces.2017.03.061.

[14] R. Clift, J.R. Grace, M.E. Weber, Bubbles, Drops and Particles, Academic Press, Cambridge (1978). ISBN: 978-0-121-76950-5.

[15] D. Leith, Aerosol Sci. Technol. 6 (1987) 153–161. https://doi.org/10.1080/02786828708959128.

[16] A. Haider, O. Levenspiel, Powder Technol. 58 (1989) 63–70. https://doi.org/10.1016/0032-5910(89)80008-7.

[17] G.H. Ganser, Powder Technol. 77 (1993) 143–152. https://doi.org/10.1016/0032-5910(93)80051-B.

[18] A. Hölzer, M. Sommerfeld, Powder Technol. 184 (2008) 361–365. https://doi.org/10.1016/j.powtec.2007.08.021.

[19] G. Bagheri, C. Bonadonna, Powder Technol. 301 (2016) 526–544. https://doi.org/10.1016/j.powtec.2016.06.015.

[20] R. Beetstra, M. van der Hoef, J. Kuipers, Comput. Fluids 35 (2006) 966–970. https://doi.org/10.1016/j.compfluid.2005.03.009.

[21] N.G. Deen, S.H.L. Kriebitzsch, M.A. van der Hoef, J.A.M. Kuipers, Chem. Eng. Sci. 81 (2012) 329–344. https://doi.org/10.1016/j.ces.2012.06.055.

[22] S.B. Pope, Turbulent Flows, Cambridge University Press, Cambridge, (2000). ISBN: 978-0-521-59886-6.

[23] S. Heinz, Prog. Aerosp. Sci. 114 (2020) 100597. https://doi.org/10.1016/j.paerosci.2019.100597.

[24] S.Y. Chen, G.D. Doolen, Annu. Rev. Fluid Mech. 30 (1998) 329–364. https://doi.org/10.1146/annurev.fluid.30.1.329.

[25] M. Dietzel, M. Sommerfeld, Powder Technol. 250 (2013) 122–137. https://doi.org/10.1016/j.powtec.2013.09.023.

[26] M. Mehrabadi, E. Murphy, S. Subramaniam, Chem. Eng. Sci. 152 (2016) 199–212. https://doi.org/10.1016/j.ces.2016.06.006.

[27] S. Chen, P. Chen, J. Fu, Phys. Fluids 34 (2022) 023307. https://doi.org/10.1063/5.0082653.

[28] ANSYS, Inc, ANSYS Fluent 14.5 Theory Guide (2012). http://www.pmt.usp.br/academic/martoran/notasmodelosgrad/ANSYS%20Fluent%20Theory%20Guide%2015.pdf [accessed 15 February 2023].

[29] J. Ferziger, M. Perić, R.L. Street, Computational Methods for Fluid Dynamics, Springer, New York, (2002). ISBN: 978-3-319-99693-6.

[30] P.R. Spalart, S.R. Allmaras, Technical Report AIAA-92-0439 1 (1992) 5–21. https://doi.org/10.2514/6.1992-439.

[31] V. Yakhot, S.A. Orszag, S. Thangam, T.B. Gatski, C.G. Speziale, Phys. Fluids A 7 (1992) 1510–1520. https://doi.org/10.1063/1.858424.

[32] F.R. Menter, AIAA J. 32 (1994) 1598–1605. https://doi.org/10.2514/3.12149.

[33] R.B. Langtry, F.R. Menter, AIAA J. 47 (2009) 2894–2906. https://doi.org/10.2514/1.42362.

[34] B.E. Launder, G.J. Reece, W. Rodi, J. Fluid Mech. 68 (1975) 537–566. https://doi.org/10.1017/S0022112075001814.

[35] W.R.A. Goossens, Powder Technol. 352 (2019) 350–359. https://doi.org/10.1016/j.powtec.2019.04.075.

[36] E. Loth, Powder Technol. 182 (2008) 342–353. https://doi.org/10.1016/j.powtec.2007.06.001.

[37] J.P. van Doormaal, G.D. Raithby, Numer. Heat Transfer 7 (1984) 147–163. https://doi.org/10.1080/01495728408961817.

[38] H.K. Versteeg, W. Malalasekera, An Introduction to Computational Fluid Dynamics: The Finite Volume Method, Pearson Education Limited, Harlow, (2007). ISBN: 978-0-131-27498-3.

[39] Z. Tuković, M. Perić, H. Jasak, Comput. Fluids 166 (2018) 78–85. https://doi.org/10.1016/j.compfluid.2018.01.041.

[40] D.C. Wilcox, Turbulence Modeling for CFD, DCW Industries, La Cañada, (2004). ISBN: 978-1-928729-08-2.

[41] B.E. Launder, B.I. Sharma, Lett. Heat Mass Trans. 1 (1974) 131–138. https://doi.org/10.1016/0094-4548(74)90150-7.

[42] J.L. Isaacs, G. Thodos, Can. J. Chem. Eng. 45 (1967) 150–155. https://doi.org/10.1002/cjce.5450450306.

[43] R. Clift, W.H. Gauvin, Can. J. Chem. Eng. 49 (1971) 439–448. https://doi.org/10.1002/cjce.5450490403.

[44] E.K. Marchildon, W.H. Gauvin, AIChE J. 25 (1979) 938–948. https://doi.org/10.1002/aic.690250604.

[45] R.P. Chhabra, L. Agarwal, N.K. Sinha, Powder Technol. 101 (1999) 288–295. https://doi.org/10.1016/S0032-5910(98)00178-8.

[46] J. Militzer, J. M. Kan, F. Hamdullahpur, P.R. Amyotte, A.M. Al Taweel, Powder Technol. 57 (1989) 193–195. https://doi.org/10.1016/0032-5910(89)80075-0.

[47] R. Ouchene, Phys. Fluids 32 (2020) 073303. https://doi.org/10.1063/5.0011618.

[48] B.R. Munson, D.F. Young, T.H. Okiishi, Fundamentals of Fluid Mechanics, John Wiley & Sons, Hoboken, (2016). ISBN: 978-1-119-54799-0.

[49] B.E. Thompson, J.H. Whitelaw, J. Fluid Mech. 157 (1985) 305–326. https://doi.org/10.1017/S0022112085002397.

[50] L. Davidson, J. Fluids Eng. 117 (1995) 50–57. https://doi.org/10.1115/1.2816818.

RICARDO ARBACH FERNANDES DE OLIVEIRA

JULIO HENRIQUE ZANATA

GABRIELA CANTARELLI LOPES

Department of Chemical Engineering, Federal University of São Carlos, São Carlos - São Paulo - Brazil

NUMERIČKO ISTRAŽIVANJE TURBULENCIJE ODREĐIVANJEM KOEFICIJENTA OTPORA ZA AGLOMERATE ČESTICA

Numeričke simulacije strujanja oko aglomerata čestica su sprovedene korišćenjem računarske dinamike fluida da bi se ocenila sposobnost pet modela turbulencije RANS da procene koeficijent otpora za aglomerate čestica. Simulacije su sprovedene u stacionarnim uslovima za Rejnoldsove brojeve između 1 i 1500. Strujnice su pokazale da simetrični aglomerati imaju profil brzine sličan profilu jedne sfere. Rezultati su pokazali da i Spalart-Allmaras i SST k-ω modeli turbulencije mogu predstaviti profil protoka u regionima blizu i daleko od zidova aglomerata i mrtve zone iza aglomerata. RNG k-ε model loše predviđa profil brzine i koeficijent otpora. Koeficijent otpora se bolje predstavlja modelom Tran-Kong, koji pokazuje da su se odstupanja od predviđanja koeficijenta otpora za aglomeratima česticasmanjivala kako se povećava gustina pakovanja aglomerata. Upotreba stabilnih RANS simulacija je izvodljiva i efikasna metoda predviđanja, uz niske računarske troškove. Za prelazne i turbulentne režime strujanja, rezultati su pokazali dobru saglasnost, sa odstupanjima između -15% i 13%, dok su za niže Rejnoldsove brojeve odstupanja varirala između -25% i 5%.

Ključne reči: čvrste materije, aglomerati čestica, turbulencija, koeficijent otpora, računarska dinamika fluida.

NAUČNI RAD